

The Vera C. Rubin Observatory Data Preview 1

1
2 VERA C. RUBIN OBSERVATORY TEAM,¹ TATIANA ACERO-CUELLAR ² EMILY ACOSTA ¹ CHRISTINA L. ADAIR ³
3 PRAKRUTH ADARI ⁴ JENNIFER K. ADELMAN-McCARTHY ⁵ ANASTASIA ALEXOV ¹ RUSS ALLBERY ¹
4 ROBYN ALLSMAN,¹ YUSRA ALSAYYAD ⁶ JHONATAN AMADO ⁵ NATHAN AMOUROUX ⁷ PIERRE ANTILOGUS ⁸
5 ALEXIS ARACENA ALCAYAGA,⁹ GONZALO ARAVENA-ROJAS ⁹ CLAUDIO H. ARAYA CORTES,⁹ ÉRIC AUBOURG ¹⁰
6 TIM S. AXELROD ¹¹ JOHN BANOVETZ ¹² CARLOS BARRÍA,⁹ AMANDA E. BAUER ¹³ BRIAN J. BAUMAN,¹⁴
7 ELLEN BECHTOL ¹⁵ KEITH BECHTOL ^{1,16} ANDREW C. BECKER ¹⁷ VALERIE R. BECKER ¹⁸
8 MARK G. BECKETT ¹⁹ ERIC C. BELLM ²⁰ PEDRO H. BERNARDINELLI ²¹ FEDERICA BETTINA BIANCO ^{2,22,23}
9 ROBERT D. BLUM ¹⁸ JOANNE BOGART,²⁴ ADAM BOLTON ³ MICHAEL T. BOOTH,¹ JAMES F. BOSCH ⁶
10 ALEXANDRE BOUCAUD ²⁵ DOMINIQUE BOUTIGNY ⁷ ROBERT A. BOVILL,¹ ANDREW BRADSHAW,^{3,24}
11 JOHAN BREGEON ²⁶ MASSIMO BRESCIA ²⁷ BRIAN J. BRONDEL ²⁸ ALEXANDER BROUGHTON ²⁴
12 AUDREY BUDLONG ²⁹ DIMITRI BUFFAT,²⁶ RODOLFO CANESTRARI ³⁰ NEVEN CAPLAR ²⁰ JEFFREY L. CARLIN ¹
13 ROSS CEBALLO ¹⁸ COLIN ORION CHANDLER ^{31,20,32} CHIHWAY CHANG ³³ GLENAVER CHARLES-EMERSON,¹
14 HSN-FANG CHIANG ³ JAMES CHIANG ²⁴ YUMI CHOI ³⁴ ERIC J. CHRISTENSEN ⁹ CHARLES F. CLAVER,¹
15 ANDY W. CLEMENTS,¹ JOSEPH J. COCKRUM,¹ JOHANN COHEN-TANUGI ³⁵ FRANCO COLLEONI,⁹ CÉLINE COMBET ²⁶
16 ANDREW J. CONNOLLY ²¹ JULIO EDUARDO CONSTANZO CORDOVA ⁹ HANS E CONTRERAS,⁹
17 JOHN FRANKLIN CRENSHAW ²¹ SYLVIE DAGORET-CAMPAGNE ³⁶ SCOTT F. DANIEL,²⁰ FELIPE DARUICH,⁹
18 GUILLAUME DAUBARD ⁸ GREG DAUES,³⁷ ERIK DENNIHY ¹ STEPHANIE J. H. DEPPE ¹⁸ SETH W. DIGEL ³
19 PETER E. DOHERTY,³⁸ CYRILLE DOUX ²⁶ ALEX DRLICA-WAGNER ⁵ GREGORY P. DUBOIS-FELSMANN ³⁹
20 FROSSIE ECONOMOU ¹ ORION EIGER ^{3,24} LUKAS EISERT ³ ALAN M. EISNER ⁴⁰ ANTHONY ENGLERT ⁴¹
21 BADEN ERB,⁹ JUAN A. FABREGA,⁹ PARKER FAGRELIUS,¹ KEVIN FANNING ³ ANGELO FAUSTI NETO ¹
22 PETER S. FERGUSON ^{21,16} AGNÈS FERTÉ ³ KRZYSZTOF FINDEISEN ²⁰ MERLIN FISHER-LEVINE ⁴²
23 GLORIA FONSECA ALVAREZ ³⁴ MICHAEL D. FOSS,³ DOMINIQUE FOUCHEZ ⁴³ DAN C. FUCHS ³ SHENMING FU ²⁴
24 EMMANUEL GANGLER ⁴⁴ IGOR GAPONENKO,³ JULEN GARCIA ⁴⁵ JOHN H GATES,³ RANPAL K. GILL ²⁸
25 ENRICO GIRO ⁴⁶ THOMAS GLANZMAN ³ ROBINSON GODOY,⁹ IAIN GOODENOW,¹ MIRANDA R. GORSUCH ¹⁶
26 MICHELLE GOWER ³⁷ MELISSA L. GRAHAM ^{20,21} MIKAEL GRANVIK ^{47,48} SARAH GREENSTREET ³⁴ WEN GUAN ¹²
27 THIBAUT GUILLEMIN ⁷ LEANNE P. GUY ⁹ DIANE HASCALL,³ PATRICK A. HASCALL,³ AREN NATHANIEL HEINZE ²¹
28 FABIO HERNANDEZ ⁴⁹ KENNETH HERNER ⁵ ARDIS HERROLD,¹ CLARE R. HIGGS ¹⁸ JOSHUA HOBLITT ¹
29 ERIN LEIGH HOWARD ²⁰ MINHEE HYUN ⁹ AMANDA IBSEN,²⁸ PATRICK INGRAHAM ¹¹ DAVID H. IRVING ¹⁸
30 ŽELJKO IVEZIĆ ^{1,20} SUZANNE H. JACOBY,¹ BUELL T. JANNUZI ⁵⁰ SREEVANI JARUGULA ⁵ M. JAMES JEE ^{51,52}
31 TIM JENNESS ¹ TOBY C. JENNINGS ³ ANDREA JEREMIE ⁷ GARRETT JERNIGAN,^{53,*} DAVID JIMÉNEZ MEJÍAS,⁹
32 ANTHONY S. JOHNSON ³ R. LYNNE JONES ²⁰ ROGER WILLIAM LEWIS JONES ⁵⁴ CLAIRE JURAMY-GILLES ⁸
33 MARIO JURIĆ ²¹ STEVEN M. KAHN ⁵⁵ J. BRYCE KALMBACH ³ YIJUNG KANG ^{24,9} ARUN KANNAWADI ^{56,6}
34 JEFFREY P. KANTOR,¹ EDWARD KARAVAKIS ¹² KSHITIJ KELKAR ⁹ LEE S. KELVIN ⁶ SCOT J. KLEINMAN,⁵⁷
35 IVAN V. KOTOV,¹² GÁBOR KOVÁCS ²¹ MIKOLAJ KOWALIK ³⁷ VICTOR L. KRABBENDAM,¹ K. SIMON KRUGHOFF ^{1,*}
36 PETR KUBÁNEK ⁹ JACOB A. KURLANDER ²¹ MILE KUSULJA,²⁶ CRAIG S. LAGE ⁵² PAULO J. A. LAGO ²⁸
37 KATHERINE LALLOTIS ⁵⁸ TRAVIS LANGE ³ DIDIER LAPORTE,⁸ RYAN M. LAU ³⁴ JUAN CARLOS LAZARTE,³
38 QUENTIN LE BOULC'H ⁴⁹ PIERRE-FRANÇOIS LÉGET ⁶ LAURENT LE GUILLOU ⁸ BENJAMIN LEVINE ⁴ MING LIANG,¹
39 SHUANG LIANG,³ KIAN-TAT LIM ³ ANJA VON DER LINDEN ⁴ HUAN LIN ⁵ MARGAUX LOPEZ ³
40 JUAN J. LOPEZ TORO,⁹ PETER LOVE,⁵⁴ ROBERT H. LUPTON ⁶ NATE B. LUST ⁶ LAUREN A. MACARTHUR ⁶
41 SEAN PATRICK MACBRIDE ⁵⁹ GREG M. MADEJSKI,²⁴ GABRIELE MAINETTI ⁴⁹ STEVEN J. MARGHEIM ²⁸
42 THOMAS W. MARKIEWICZ ³ PHIL MARSHALL ³ STUART MARSHALL,²⁴ GUIDO MAULEN,⁹ SIDNEY MAU ⁵⁶
43 MORGAN MAY,^{60,12} JEREMY McCORMICK ³ DAVID MCKAY ⁶¹ ROBERT MCKERCHER,¹ GUILLEM MEGIAS HOMAR ⁶²
44 AARON M. MEISNER ³⁴ FELIPE MENANTEAU,³⁷ HEATHER R. MENTZER ⁴⁰ KRISTEN METZGER,¹⁸
45 JOSHUA E. MEYERS ²⁴ MICHELLE MILLER,³⁴ DAVID J. MILLS,¹ JOACHIM MOEYENS ²¹ MARC MONIEZ,³⁶
46 FRED E. MOOLEKAMP ⁶³ C. A. L. MORALES MARÍN ⁹ FRITZ MUELLER ³ JAMES R. MULLANEY ⁶⁴
47 FREDDY MUÑOZ ARANCIBIA,¹ KATE NAPIER ²⁴ HOMER NEAL,³ ERIC H. NEILSEN, JR. ⁵ JEREMY NEVEU ³⁶
48 TIMOTHY NOBLE,⁶⁵ ERFAN NOURBAKHSH ⁶ KNUT OLSEN ³⁴ WILLIAM O'MULLANE ⁹ DMITRY ONOPRIENKO,³
49 MARCO ORIUNNO ³ SHAWN OSIER,³ RUSSELL E. OWEN,²⁰ AASHAY PAI ³³ JOHN K. PAREJKO ²⁰ HYE YUN PARK ⁵⁶

50 JAMES B. PARSONS,^{37,*} MARIA T. PATTERSON^{id,20} MARINA S. PAVLOVIC^{id,9} KARLA PEÑA RAMÍREZ^{id,9}
 51 JOHN R. PETERSON^{id,66} STEPHEN R. PIETROWICZ^{id,37} ANDRÉS A. PLAZAS MALAGÓN^{id,3,24} REBEKAH POLEN,⁵⁶
 52 HANNAH MARY MARGARET POLLEK,³ PAUL A. PRICE^{id,6} BRUNO C. QUINT^{id,1} JOSÉ MIGUEL QUINTERO MARIN,⁹
 53 MARKUS RABUS^{id,67} BENJAMIN RACINE^{id,43} VELJKO RADEKA,¹² MANON RAMEL,²⁶ ARIANNA RANABHAT^{id,68}
 54 ANDREW P. RASMUSSEN^{id,24} DAVID A. RATHFELDER,⁶⁹ MEREDITH L. RAWLS^{id,20,21} SOPHIE L. REED^{id,6}
 55 KEVIN A. REIL^{id,3} DAVID J. REISS,²⁰ MICHAEL A. REUTER^{id,1} TIAGO RIBEIRO^{id,1} MICKAEL RIGAULT^{id,70}
 56 VINCENT J. RIOT^{id,14} STEVEN M. RITZ^{id,40} MARIO F. RIVERA RIVERA,⁹ BRANT E. ROBERTSON^{id,71}
 57 WILLIAM ROBY^{id,39} GABRIELE RODEGHIERO^{id,72} AARON ROODMAN^{id,24} LUCA ROSIGNOLI^{id,73,72} CÉCILE ROUCELLE^{id,25}
 58 MATTHEW R. RUMORE^{id,12} STEFANO RUSSO,⁸ ELI S. RYKOFF^{id,24} ANDREI SALNIKOV^{id,3} BRUNO O. SÁNCHEZ^{id,43}
 59 DAVID SANMARTIM^{id,9} CLARE SAUNDERS^{id,6} RAFE H. SCHINDLER,²⁴ SAMUEL J. SCHMIDT^{id,52} JACQUES SEBAG,⁹
 60 NIMA SEDAGHAT^{id,20} BRIAN SELVY,¹ EDGARD ESTEBAN SEPULVEDA VALENZUELA,⁹ GONZALO SERICHE^{id,9}
 61 JACQUELINE C. SERON-NAVARRETE^{id,9} IGNACIO SEVILLA-NOARBE^{id,74} ALYSHA B. SHUGART^{id,9} JONATHAN SICK^{id,75,1}
 62 CRISTIÁN SILVA^{id,9} MATHEW C. SIMS^{id,76} JALADH SINGHAL^{id,39} KEVIN BENJAMIN SIRUNO,⁹ COLIN T. SLATER^{id,20}
 63 BRIANNA M. SMART^{id,20} ADAM SNYDER^{id,52} CHRISTINE SOLDAHL,³ IOANA SOTUELA ELORRIAGA^{id,9} BRIAN STALDER^{id,1}
 64 HERNAN STOCKEBRAND^{id,9} ALAN L. STRAUSS^{id,18} MICHAEL A. STRAUSS^{id,6} KRZYSZTOF SUBERLAK^{id,20}
 65 IAN S. SULLIVAN^{id,20} JOHN D. SWINBANK^{id,77,6} DIEGO TAPIA^{id,9} ALESSIO TARANTO^{id,72,73} DAN S. TARANU^{id,6}
 66 JOHN GREGG THAYER^{id,3} SANDRINE THOMAS^{id,18} ADAM J. THORNTON^{id,1} ROBERTO TIGHE,⁹
 67 LAURA TORIBIO SAN CIPRIANO,⁷⁴ TE-WEI TSAI^{id,1} DOUGLAS L. TUCKER^{id,5} MAX TURRI,³ J. ANTHONY TYSON^{id,52}
 68 ELANA K. URBACH^{id,78} YOUSUKE UTSUMI^{id,79} BRIAN VAN KLAVEREN,³ WOUTER VAN REEVEN^{id,9}
 69 PETER ANTHONY VAUCHER^{id,3} PAULINA VENEGAS^{id,28} APRAJITA VERMA^{id,80} ANTONIA SIERRA VILLARREAL^{id,3}
 70 STELIOS VOUTSINAS^{id,1} CHRISTOPHER W. WALTER^{id,56} YUANKUN (DAVID) WANG^{id,21} CHRISTOPHER Z. WATERS^{id,6}
 71 CHRISTINA C. WILLIAMS^{id,34} BETH WILLMAN^{id,81} MATTHIAS WITTGEN^{id,3} W. M. WOOD-VASEY^{id,82} WEI YANG^{id,3}
 72 ZHAOYU YANG^{id,12} BRIAN P. YANNY^{id,5} PETER YOACHIM^{id,20} TIANQING ZHANG^{id,82} CONGHAO ZHOU^{id,40} AND
 73 DANICA ŽILKOVÁ^{id,28}

74 ¹Vera C. Rubin Observatory Project Office, 950 N. Cherry Ave., Tucson, AZ 85719, USA

75 ²Department of Physics and Astronomy, University of Delaware, Newark, DE 19716-2570, USA

76 ³SLAC National Accelerator Laboratory, 2575 Sand Hill Rd., Menlo Park, CA 94025, USA

77 ⁴Department of Physics and Astronomy, Stony Brook University, Stony Brook, NY 11794, USA

78 ⁵Fermi National Accelerator Laboratory, P. O. Box 500, Batavia, IL 60510, USA

79 ⁶Department of Astrophysical Sciences, Princeton University, Princeton, NJ 08544, USA

80 ⁷Université Savoie Mont-Blanc, CNRS/IN2P3, LAPP, 9 Chemin de Bellevue, F-74940 Annecy-le-Vieux, France

81 ⁸Sorbonne Université, Université Paris Cité, CNRS/IN2P3, LPNHE, 4 place Jussieu, F-75005 Paris, France

82 ⁹Vera C. Rubin Observatory, Avenida Juan Cisternas #1500, La Serena, Chile

83 ¹⁰Université Paris Cité, CNRS/IN2P3, CEA, APC, 4 rue Elsa Morante, F-75013 Paris, France

84 ¹¹Steward Observatory, The University of Arizona, 933 N. Cherry Ave., Tucson, AZ 85721, USA

85 ¹²Brookhaven National Laboratory, Upton, NY 11973, USA

86 ¹³Yerkes Observatory, 373 W. Geneva St., Williams Bay, WI 53191, USA

87 ¹⁴Lawrence Livermore National Laboratory, 7000 East Avenue, Livermore, CA 94550, USA

88 ¹⁵Wisconsin IceCube Particle Astrophysics Center, University of Wisconsin—Madison, Madison, WI 53706, USA

89 ¹⁶Department of Physics, University of Wisconsin-Madison, Madison, WI 53706, USA

90 ¹⁷Amazon Web Services, Seattle, WA 98121, USA

91 ¹⁸Vera C. Rubin Observatory/NSF NOIRLab, 950 N. Cherry Ave., Tucson, AZ 85719, USA

92 ¹⁹Institute for Astronomy, University of Edinburgh, Royal Observatory, Blackford Hill, Edinburgh EH9 3HJ, UK

93 ²⁰University of Washington, Dept. of Astronomy, Box 351580, Seattle, WA 98195, USA

94 ²¹Institute for Data-intensive Research in Astrophysics and Cosmology, University of Washington, 3910 15th Avenue NE, Seattle, WA
 95 98195, USA

96 ²²Data Science Institute, University of Delaware, Newark, DE 19717 USA

97 ²³Joseph R. Biden, Jr., School of Public Policy and Administration, University of Delaware, Newark, DE 19717 USA

98 ²⁴Kavli Institute for Particle Astrophysics and Cosmology, SLAC National Accelerator Laboratory, 2575 Sand Hill Rd., Menlo Park, CA
 99 94025, USA

100 ²⁵Université Paris Cité, CNRS/IN2P3, APC, 4 rue Elsa Morante, F-75013 Paris, France

101 ²⁶Université Grenoble Alpes, CNRS/IN2P3, LPSC, 53 avenue des Martyrs, F-38026 Grenoble, France

102 ²⁷Department of Physics "E. Pancini", University Federico II of Napoli, Via Cintia, 80126 Napoli, Italy

103 ²⁸Vera C. Rubin Observatory/NSF NOIRLab, Avenida Juan Cisternas #1500, La Serena, Chile

104 ²⁹University of Washington, Dept. of Physics, Box 351580, Seattle, WA 98195, USA

105 ³⁰INAF Istituto di Astrofisica Spaziale e Fisica Cosmica di Palermo, Via Ugo la Malfa 153, 90146, Palermo, Italy

- 106 ³¹LSST Interdisciplinary Network for Collaboration and Computing, Tucson, USA
- 107 ³²Department of Astronomy and Planetary Science, Northern Arizona University, P.O. Box 6010, Flagstaff, AZ 86011, USA
- 108 ³³Department of Astronomy and Astrophysics, University of Chicago, 5640 South Ellis Avenue, Chicago, IL 60637, USA
- 109 ³⁴NSF NOIRLab, 950 N. Cherry Ave., Tucson, AZ 85719, USA
- 110 ³⁵LPCA, Université Clermont-Auvergne, CNRS/IN2P3, Clermont-Ferrand, France
- 111 ³⁶Université Paris-Saclay, CNRS/IN2P3, IJCLab, 15 Rue Georges Clemenceau, F-91405 Orsay, France
- 112 ³⁷NCSA, University of Illinois at Urbana-Champaign, 1205 W. Clark St., Urbana, IL 61801, USA
- 113 ³⁸Smithsonian Astrophysical Observatory, 60 Garden St., Cambridge MA 02138, USA
- 114 ³⁹Caltech/IPAC, California Institute of Technology, MS 100-22, Pasadena, CA 91125-2200, USA
- 115 ⁴⁰Santa Cruz Institute for Particle Physics and Physics Department, University of California–Santa Cruz, 1156 High St., Santa Cruz,
116 CA 95064, USA
- 117 ⁴¹Department of Physics, Brown University, 182 Hope Street, Providence, RI 02912, USA
- 118 ⁴²D4D CONSULTING LTD., Suite 1 Second Floor, Everdene House, Deansleigh Road, Bournemouth, UK BH7 7DU
- 119 ⁴³Aix Marseille Université, CNRS/IN2P3, CPPM, 163 avenue de Luminy, F-13288 Marseille, France
- 120 ⁴⁴Université Clermont Auvergne, CNRS/IN2P3, LPCA, 4 Avenue Blaise Pascal, F-63000 Clermont-Ferrand, France
- 121 ⁴⁵C. Iñaki Goenaga, 5, 20600, Guipúzcoa, Spain
- 122 ⁴⁶INAF Osservatorio Astronomico di Trieste, Via Giovan Battista Tiepolo 11, 34143, Trieste, Italy
- 123 ⁴⁷Department of Physics, P.O. Box 64, 00014 University of Helsinki, Finland
- 124 ⁴⁸Asteroid Engineering Laboratory, Luleå University of Technology, Box 848, SE-981 28 Kiruna, Sweden
- 125 ⁴⁹CNRS/IN2P3, CC-IN2P3, 21 avenue Pierre de Coubertin, F-69627 Villeurbanne, France
- 126 ⁵⁰University of Arizona, Department of Astronomy and Steward Observatory, 933 N. Cherry Ave, Tucson, AZ 85721, USA
- 127 ⁵¹Department of Astronomy, Yonsei University, 50 Yonsei-ro, Seoul 03722, Republic of Korea
- 128 ⁵²Physics Department, University of California, One Shields Avenue, Davis, CA 95616, USA
- 129 ⁵³Space Sciences Lab, University of California, 7 Gauss Way, Berkeley, CA 94720-7450, USA
- 130 ⁵⁴Lancaster University, Lancaster, UK
- 131 ⁵⁵Physics Department, University of California, 366 Physics North, MC 7300 Berkeley, CA 94720, USA
- 132 ⁵⁶Department of Physics, Duke University, Durham, NC 27708, USA
- 133 ⁵⁷Astromanager LLC, 63 Halai St, Hilo, 96720 Hawaii, USA
- 134 ⁵⁸Center for Cosmology and Astro-Particle Physics, The Ohio State University, Columbus, OH 43210, USA
- 135 ⁵⁹Physik-Institut, University of Zurich, Winterthurerstrasse 190, 8057 Zurich, Switzerland
- 136 ⁶⁰Department of Physics Columbia University, New York, NY 10027, USA
- 137 ⁶¹EPCC, University of Edinburgh, 47 Potterrow, Edinburgh, EH8 9BT, UK
- 138 ⁶²Division of Physics, Mathematics and Astronomy, California Institute of Technology, Pasadena, CA 91125, USA
- 139 ⁶³soZen Inc., 105 Clearview Dr, Penfield, NY 14526
- 140 ⁶⁴Astrophysics Research Cluster, School of Mathematical and Physical Sciences, University of Sheffield, Sheffield, S3 7RH, United
141 Kingdom
- 142 ⁶⁵Science and Technology Facilities Council, Rutherford Appleton Laboratory, Harwell, UK
- 143 ⁶⁶Department of Physics and Astronomy, Purdue University, 525 Northwestern Ave., West Lafayette, IN 47907, USA
- 144 ⁶⁷Departamento de Matemática y Física Aplicadas, Facultad de Ingeniería, Universidad Católica de la Santísima Concepción, Alonso de
145 Rivera 2850, Concepción, Chile
- 146 ⁶⁸Australian Astronomical Optics, Macquarie University, North Ryde, NSW, Australia
- 147 ⁶⁹AURA, 950 N. Cherry Ave., Tucson, AZ 85719, USA
- 148 ⁷⁰Université Claude Bernard Lyon 1, CNRS/IN2P3, IP2I, 4 Rue Enrico Fermi, F-69622 Villeurbanne, France
- 149 ⁷¹Department of Astronomy and Astrophysics, University of California–Santa Cruz, 1156 High St., Santa Cruz, CA 95064, USA
- 150 ⁷²INAF Osservatorio di Astrofisica e Scienza dello Spazio Bologna, Via P. Gobetti 93/3, 40129, Bologna, Italy
- 151 ⁷³Department of Physics and Astronomy (DIFA), University of Bologna, Via P. Gobetti 93/2, 40129, Bologna, Italy
- 152 ⁷⁴Centro de Investigaciones Energéticas, Medioambientales y Tecnológicas, Av. Complutense 40, 28040 Madrid, Spain
- 153 ⁷⁵J.Sick Codes Inc., Penetanguishene, Ontario, Canada
- 154 ⁷⁶Science and Technology Facilities Council, UK Research and Innovation, Polaris House, North Star Avenue, Swindon, SN2 1SZ, UK
- 155 ⁷⁷ASTRON, Oude Hoogeveensedijk 4, 7991 PD, Dwingeloo, The Netherlands
- 156 ⁷⁸Department of Physics, Harvard University, 17 Oxford St., Cambridge MA 02138, USA
- 157 ⁷⁹National Astronomical Observatory of Japan, Chile Observatory, Los Abedules 3085, Vitacura, Santiago, Chile
- 158 ⁸⁰Department of Physics, University of Oxford, Denys Wilkinson Building, Keble Road, Oxford, OX1 3RH, UK
- 159 ⁸¹LSST Discovery Alliance, 933 N. Cherry Ave., Tucson, AZ 85719, USA
- 160 ⁸²Department of Physics and Astronomy, University of Pittsburgh, 3941 O’Hara Street, Pittsburgh, PA 15260, USA

(Dated: March 24, 2026)

ABSTRACT

We present Rubin Data Preview 1 (DP1), the first data from the NSF-DOE Vera C. Rubin Observatory, comprising raw and calibrated single-epoch images, coadds, difference images, detection catalogs, and ancillary data products. DP1 is based on 1792 optical/near-infrared exposures acquired over 48 distinct nights by the Rubin Commissioning Camera, LSSTComCam, on the Simonyi Survey Telescope at the Summit Facility on Cerro Pachón, Chile in late 2024. DP1 covers $\sim 15 \text{ deg}^2$ distributed across seven roughly equal-sized non-contiguous fields, each independently observed in six broad photometric bands, *ugrizy*. The median FWHM of the point-spread function across all bands is approximately $1''.14$, with the sharpest images reaching about $0''.58$. The 5σ point source depths for coadded images in the deepest field, the Extended Chandra Deep Field South, are: $u = 24.55, g = 26.18, r = 25.96, i = 25.71, z = 25.07, y = 23.1$. Other fields are no more than 2.2 magnitudes shallower in any band, where they have nonzero coverage. DP1 contains approximately 2.3 million distinct astrophysical objects, of which 1.6 million are extended in at least one band in coadds, and 431 solar system objects, of which 93 are new discoveries. DP1 is approximately 3.5 TB in size and is available to Rubin data rights holders via the Rubin Science Platform, a cloud-based environment for the analysis of petascale astronomical data. While small compared to future LSST releases, its high quality and diversity of data support a broad range of early science investigations ahead of full operations in 2026.

Keywords: Rubin Observatory – LSST

1. INTRODUCTION

The National Science Foundation (NSF)–Department of Energy (DOE) Vera C. Rubin Observatory is a ground-based, wide-field optical/near-infrared facility located on Cerro Pachón in northern Chile. Named in honor of Vera C. Rubin, a pioneering astronomer whose groundbreaking work in the 20th century provided the first convincing evidence for the existence of dark matter (V. C. Rubin & W. K. Ford 1970; V. C. Rubin et al. 1980), the observatory’s prime mission is to carry out the Legacy Survey of Space and Time (LSST) (Ž. Ivezić et al. 2019a). This 10-year survey is designed to obtain rapid-cadence, multi-band imaging of the entire visible southern sky approximately every 3–4 nights. Over its main $18,000 \text{ deg}^2$ footprint, the LSST is expected to reach a depth of ~ 27 magnitude in the r-band, with ~ 800 visits per pointing in all filters (F. B. Bianco et al. 2022).

The Rubin Observatory system consists of four main components: the Simonyi Survey Telescope, featuring an 8.4 m diameter (6.5 m effective aperture) primary mirror that delivers a wide field of view; the 3.2-gigapixel LSST Science Camera (LSSTCam), capable of imaging 9.6 square degrees per exposure⁸³ with seeing-limited

quality in six broadband filters, *ugrizy* (320–1050 nm); an automated Data Management System that processes and archives tens of terabytes of data per night, generating science-ready data products within minutes for a global community of scientists; and an Education and Public Outreach (EPO) program that provides real-time data access, interactive tools, and educational content to engage the public. The integrated system’s étendue⁸⁴ of $319 \text{ m}^2 \text{ deg}^2$, is over an order of magnitude larger than that of any previous optical observatory, enabling a fast, large-scale survey with exceptional depth in a fraction of the time compared to other observatories.

The observatory’s design is driven by four key science themes: probing dark energy and dark matter; taking an inventory of the solar system; exploring the transient and variable optical sky; and mapping the Milky Way (Ž. Ivezić et al. 2019a). These themes inform the optimization of a range of system parameters, including image quality; photometric and astrometric accuracy; single-visit depth; coadded survey depth; the filter complement; the total number of visits per pointing and their distribution on the sky; and total sky coverage. Additionally, they inform the design of the data processing and access systems. By optimizing the system parameters to support a wide range of scientific goals, we maximize the observatory’s scientific output across

* Author is deceased

⁸³ We define an “exposure” as the process of exposing all detectors in the focal plane. It is synonymous with the term “visit” in DP1. By contrast, an “image” is the output of a single detector following an exposure.

⁸⁴ The product of the primary mirror area and the angular area of its field of view for a given set of observing conditions.

all areas, making Rubin a powerful discovery machine capable of addressing a broad range of astrophysical questions.

Throughout the duration of the LSST, Rubin Observatory will issue a series of Data Releases, each representing a complete reprocessing of all LSST data collected up to that point. Prior to the start of the LSST survey, commissioning activities generated a significant volume of science-grade data. To make this early data available to the community, the Rubin Early Science Program (L. P. Guy et al. 2026) was established. One key component of this program is a series of Data Previews; early versions of the LSST Data Releases. These previews include preliminary data products derived from both simulated and commissioning data, which, together with early versions of the data access services, are intended to support high-impact early science, facilitate community readiness, and inform the development of Rubin’s operational capabilities ahead of the start of full survey operations. All data and services provided through the Rubin Early Science Program are offered on a shared-risk basis⁸⁵.

This paper describes Rubin’s second of three planned Data Previews: Data Preview 1 (DP1) (NSF-DOE Vera C. Rubin Observatory 2025a). The first, Data Preview 0 (DP0), contained data products produced from the processing of simulated LSST-like data sets. These were released together with a very early version of the Rubin Science Platform (RSP) (M. Jurić et al. 2019), which provided the data access services. DP0 was released in multiple phases; DP0.1, DP0.2, and DP0.3, each building upon the previous and incorporating new data and functionalities. DP0.1 and DP0.2 uses data from the cosmoDC2 simulations (LSST Dark Energy Science Collaboration (LSST DESC) et al. 2021) prepared by the Dark Energy Science Collaboration (DESC), whereas DP0.3 is based on simulated datasets from the Solar System Science Collaboration (SSSC). Online documentation for DP0 is available at <https://dp0.lsst.io>.

DP1 contains data products derived from the reprocessing of science-grade exposures acquired by the Rubin Commissioning Camera (LSSTComCam) in late 2024. The third and final Data Preview, Data Preview 2 (DP2), is planned to be based on a reprocessing of all science-grade data taken with Rubin’s LSSTCam during commissioning.

All Rubin Data Releases and Previews are subject to a two-year proprietary period, with immediate access granted exclusively to LSST data rights holders⁸⁶ (R. Blum & the Rubin Operations Team 2020). After the two-year proprietary period, DP1 will be made public. However, even once the data become public, access for individuals without data rights will not be provided through Rubin Data Access Centers in the US and Chile (R. Blum & the Rubin Operations Team 2020). Alternative access mechanisms are still under discussion and have not yet been finalized.

In this paper, we describe the contents and validation of Rubin DP1, the first Data Preview to deliver data derived from observations conducted by the Vera C. Rubin Observatory, as well as the data-access mechanisms and community-support services that accompany it. DP1 is based on the reprocessing of 1792 science-grade exposures acquired during the first on-sky commissioning campaign, conducted over 48 nights between 2024-10-24 and 2024-12-11. It covers a total area of approximately ~ 15 deg² distributed across seven distinct non-contiguous fields. The data products include raw and calibrated single-epoch images, coadded images, difference images, detection catalogs, and other derived data products. DP1 is about 3.5 TB in size and contains around 2.3 million distinct astronomical objects, detected in 2644 coadded images. Full DP1 release documentation is available at <https://dp1.lsst.io>. Despite Rubin Observatory still being in commissioning and not yet complete at the time the observations were acquired, Rubin DP1 provides an important first look at the data, showcasing its characteristics and capabilities.

The structure of this paper is as follows. In section 2 we describe the observatory system and overall construction and commissioning status at the time of data acquisition, the seven fields included in DP1, and the observing strategy used. Section 3 summarizes the contents of DP1 and the data products contained in the release. The data processing pipelines are described in section 4, followed by a description of the data validation and performance assessment in section 5. Section 6 describes the RSP, a cloud-based data science infrastructure that provides tools and services to Rubin data rights holders to access, visualize and analyze peta-scale data generated by the LSST. Section 7 presents Rubin Observatory’s model for community support, which emphasizes self-help via documentation and tutorials, and employs an open platform for issue reporting that en-

⁸⁵ Shared risk means early access with caveats: the community benefits from getting a head start on science, preparing analyses, and providing feedback, while also accepting that the system may not work as well as it will during full operations.

⁸⁶ Individuals or institutions with formal authorization to access proprietary data collected by the Vera C. Rubin Observatory. See <https://www.lsst.org/scientists/international-drh-list>

ables crowd-sourced solutions. Finally, a summary of the DP1 release and information on expected future releases of data is given in section 8. The appendix contains a useful glossary of terms used throughout this paper.

All magnitudes quoted are in the AB system (J. B. Oke & J. E. Gunn 1983), unless otherwise specified.

2. ON-SKY COMMISSIONING CAMPAIGN

The primary objective of the first Rubin on-sky commissioning campaign was to optically align the Simonyi Survey Telescope and verify its ability to deliver acceptable image quality using the Commissioning Camera, LSSTComCam. Additionally, the campaign provided valuable operational experience to support commissioning the LSST Science Camera, LSSTCam (T. Lange et al. 2024; A. Roodman et al. 2024). We note that commissioning LSSTComCam was not an objective of the campaign; rather LSSTComCam was used as a tool to support broader observatory commissioning, including early testing of the Active Optics System (AOS) (§2.1) and the LSST Science Pipelines (§2.4). As a result, many artifacts present in the data are specific to LSSTComCam and will be addressed only if they persist with LSSTCam. Accordingly, the image quality achieved during this campaign, and in the DP1 data, may not reflect the performance ultimately expected from LSSTCam.

Approximately 16,000 exposures⁸⁷ were collected during this campaign, the majority in support of AOS commissioning, system-level verification, and end-to-end testing of the telescope’s hardware and software. This included over 10000 exposures for AOS commissioning, more than 2000 bias and dark calibration frames, and over 2000 exposures dedicated to commissioning the LSST Science Pipelines. For DP1, we have selected a subset of 1792 science-grade exposures from this campaign that are most useful for the community to begin preparing for early science.

At the time of the campaign, the observatory was still under construction, with several key components, such as dome thermal control, full mirror control, and the final AOS configuration either incomplete or still undergoing commissioning. As a result, image quality varied widely throughout the campaign and exhibited a broader distribution than is expected with LSSTCam. Despite these limitations, the campaign success-

fully demonstrated system integration and established a functional observatory.

2.1. Simonyi Survey Telescope

The Simonyi Survey Telescope (B. Stalder et al. 2024) features a unique three-mirror design, including an 8.4-meter Primary Mirror Tertiary Mirror (M1M3) fabricated from a single substrate and a 3.5-meter Secondary Mirror (M2). This compact configuration supports a wide 3.5-degree field of view while enabling exceptional stability, allowing the telescope to slew and settle in under five seconds. To achieve the scientific goals of the 10-year LSST, the Observatory must maintain high image quality across its wide field of view (Ž. Ivezić et al. 2019b). This is accomplished through the AOS (B. Xin et al. 2015; G. Megias Homar et al. 2024), which corrects, between successive exposures, wavefront distortions caused by optical misalignments and mirror surface deformations, primarily due to the effect of gravitational and thermal loads.

The AOS, which comprises an open-loop component and a closed-loop component, optimizes image quality by aligning the camera and M2 relative to M1M3, as well as adjusting the shapes of all three mirrors to nanometer precision. The AOS open-loop component corrects for predictable distortions and misalignments, while the closed-loop component addresses unpredictable or slowly varying aberrations using feedback from the corner wavefront sensors. The closed-loop wavefront sensing technique is curvature wavefront sensing, which infers wavefront errors in the optical system by analyzing extra- and intra-focal star images (S. Thomas et al. 2023). Since LSSTComCam lacks dedicated wavefront sensors, wavefront errors were instead estimated by defocusing the telescope ± 1.5 mm on either side of focus and applying the curvature wavefront sensing pipeline to the resulting images. Each night began with an initial alignment correction using a laser tracker to position the system within the capture range of the closed-loop algorithm (G. Megias Homar et al. 2024). Once this coarse alignment was complete, the AOS refined the optical alignment and applied mirror surfaces corrections to optimize the image quality across the LSSTComCam field of view.

During LSST Science Pipelines commissioning (§2.4), observations were conducted using the AOS in open-loop mode only, without closed-loop corrections between exposures. Closed-loop operation, which requires additional intra- and extra-focal images with LSSTComCam, was not compatible with the continuous data acquisition needed by the pipelines. The image quality for these data was monitored by measuring the Point

⁸⁷ We define an exposure as the process of exposing all LSSTComCam detectors. It is synonymous with visit in DP1. By contrast, an image is the output of a single LSSTComCam detector following an exposure.

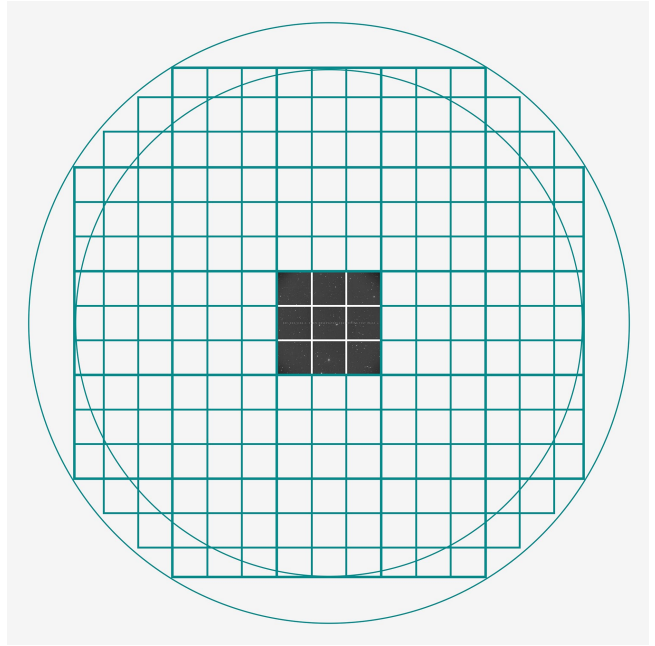
421 Spread Function (PSF) at Full Width at Half-Maximum
 422 (FWHM), and closed-loop sequences were periodically
 423 run when image quality degradation was observed.

424 2.2. The LSST Commissioning Camera

425 LSSTComCam (B. Stalder et al. 2022, 2020; J.
 426 Howard et al. 2018; SLAC National Accelerator Labora-
 427 tory & NSF-DOE Vera C. Rubin Observatory 2024) is
 428 a 144-megapixel version of the 3.2-gigapixel LSSTCam.
 429 It covers approximately 5% of the LSSTCam focal plane
 430 area, with a field of view of $\sim 0.5 \text{ deg}^2$ ($40' \times 40'$), com-
 431 pared to LSSTCam’s 9.6 deg^2 . It was developed to val-
 432 idate camera interfaces with other observatory compo-
 433 nents and evaluate overall system performance prior to
 434 the start of LSSTCam commissioning. Although LSST-
 435 ComCam has a smaller imaging area, it shares the same
 436 plate scale of $0''.2$ per pixel and is housed in a support
 437 structure that replicates the mass, center of gravity, and
 438 physical dimensions of LSSTCam. All mechanical and
 439 utility interfaces to the telescope are implemented iden-
 440 tically, enabling full end-to-end testing of observatory
 441 systems, including readout electronics, image acquisi-
 442 tion, and data pipelines. Although the LSSTComCam
 443 cryostat employs a different cooling system (Cryotels) to
 444 that of LSSTCam, it included a refrigeration pathfinder
 445 to validate the cryogenic system intended for LSSTCam.

446 The LSSTCam focal plane comprises 25 modular rafts
 447 arranged in a 5×5 grid, of which 21 are science rafts de-
 448 dicated to imaging and 4 are corner rafts used for guid-
 449 ing and wavefront sensing. LSSTCam employs CCD
 450 sensors from two vendors: Imaging Technology Labora-
 451 tory, University of Arizona (UA) (ITL) and Teledyne
 452 (E2V). In contrast, LSSTComCam contains only a single
 453 science raft equipped exclusively with ITL sensors.
 454 Figure 1 presents a schematic of the LSSTCam focal
 455 plane, with the LSSTComCam raft positioned at the
 456 center, corresponding to the LSSTCam central science
 457 raft location. The perspective is from above, looking
 458 down through the LSSTComCam lenses onto the focal
 459 plane.

460 Each science raft is a self-contained unit compris-
 461 ing nine $4\text{K} \times 4\text{K}$ Charge-Coupled Device (CCD) (G. E.
 462 Smith 2010) sensors arranged in a 3×3 mosaic, complete
 463 with integrated readout electronics and cooling systems.
 464 Each sensor is subdivided into 16 segments arranged in
 465 a 2×8 layout, with each segment consisting of 512×2048
 466 pixels and read out in parallel using individual ampli-
 467 fiers. This design is identical across all science rafts.
 468 To maintain uniform performance and calibration, each
 469 raft is populated exclusively with sensors from a single
 470 vendor.
 471



472 **Figure 1.** LSSTComCam focal plane layout illustrating the
 473 placement of its nine sensors, shown in gray, which form a
 474 raft. The view is looking down from above the focal plane
 475 through the LSSTComCam lenses. LSSTComCam is Raft
 476 R22 (R22). We also indicate the location of the LSSTCam
 477 sensors (open squares) to highlight the field-of-view of LSST-
 478 ComCam in relation to that of LSSTCam.

479 LSSTComCam consists of a single science raft, design-
 480 ated Raft 22 (R22), equipped solely with ITL sensors.
 481 These sensors were selected from the best-performing re-
 482 maining ITL devices after the LSSTCam rafts were fully
 483 populated. Some exhibit known issues such as high read-
 484 out noise (e.g., Detector 8) and elevated Charge Transfer
 485 Inefficiency (CTI) (e.g., Detector 5). Consequently, cer-
 486 tain image artifacts present in the DP1 dataset may be
 specific to LSSTComCam. Figure 2 shows the LSST-
 ComCam R22 focal plane layout and the placement and
 numbering scheme of sensors (S) and amplifiers (C).
 This configuration is identical across all science rafts
 in LSSTCam. The LSSTCam and LSSTComCam focal
 planes are described in detail in A. A. Plazas Malagón
 et al. (2026).

488 2.2.1. Filter Complement

489 LSSTComCam supports imaging with six broadband
 490 filters *ugrizy* spanning 320–1050 nm, identical in de-
 491 sign to LSSTCam. However, its filter exchanger can
 492 hold only three filters at a time, compared to five with
 493 LSSTCam. The full-system throughput of the six LSST-
 494 ComCam filters, which encompasses contributions from
 495 a standard atmosphere at airmass 1.2, telescope opt-
 496 ics, camera surfaces, and the mean ITL detector quan-

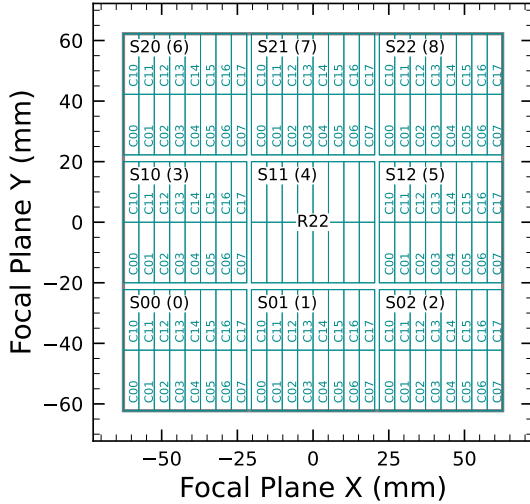


Figure 2. LSSTComCam focal plane layout, showing Raft 22 (R22) and the placement and numbering scheme of sensors (S) and amplifiers (C). The view is from above, looking through the LSSTComCam lenses onto the focal plane. Each sensor contains 16 amplifiers, and the raft is composed of a 3×3 array of sensors. The detector number for each sensor is indicated in parentheses.

497 tum efficiency is shown in Figure 3. The corresponding
 498 transmission curves are provided as a DP1 data product
 499 (§3.6.1).

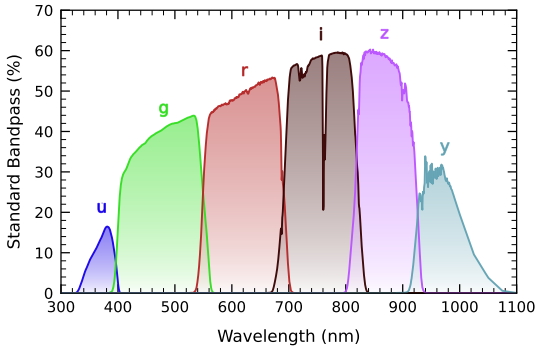


Figure 3. LSSTComCam standard bandpasses, illustrating full system throughput. The bandpasses include a standard atmosphere at airmass 1.2, telescope optics, camera surfaces, and mean ITL detector quantum efficiency. The corresponding transmission curves are provided as a DP1 data product.

2.2.2. Timing Calibration

503 The absolute time accuracy of data taken with LSST-
 504 ComCam relies on the Network Time Protocol (NTP)
 505 for clock synchronization, which should be accurate
 506 to approximately 1 millisecond. In order to evaluate
 507 the absolute timing accuracy of the entire system we
 508 observed the geosynchronous satellite EUTELSAT 117

509 West B with a set of 10 usable 10-second exposures over
 510 two nights. EUTELSAT 117 West B is part the Global
 511 Positioning System (GPS) system and serves as one of
 512 the Wide Area Augmentation System (WAAS) satellites
 513 operated for the U.S. Federal Aviation Administration
 514 (FAA) and used to broadcast GPS corrections to air
 515 traffic.

516 As these satellites are part of the GPS system, their
 517 positions are tracked very precisely and the record of
 518 their locations is published after the fact and can be
 519 downloaded. Following the technique previously em-
 520 ployed by other surveys, (J. L. Tonry et al. 2018), we
 521 observed the satellite while tracking the sky and then
 522 downloaded the data-files with its precise locations from
 523 the National Satellite Test Bed web site⁸⁸. By compar-
 524 ing the measured and predicted locations of the start
 525 of the satellite track on the sky, we determined that
 526 (relative to the start of integration-time recorded in the
 527 Flexible Image Transport System (FITS) headers) our
 528 time was accurate to 53.6 ± 11.0 milliseconds.

529 This work continues to be an area of ongoing study,
 530 with the exact timing of when the shutter open com-
 531 mand is issued, and the complete profile of the shutter
 532 movement not yet determined. However the open com-
 533 mand is on average near 29 milliseconds later. Incorpor-
 534 ating the delays into the fit reduces the offset to 24.8
 535 ± 11.0 milliseconds.

536 The full shutter takes approximately 396 milliseconds
 537 to completely open. As the LSSTComCam sensors are
 538 centered in the aperture, the center of the focal plane
 539 should be exposed about half-way through the shutter
 540 open procedure, 198 milliseconds after the open com-
 541 mand. There are uncertainties on the full motion pro-
 542 file, and the blade direction motions are currently not
 543 known, but the fraction of the shutter aperture sub-
 544 tended by the focal plane is 52%. This implies that that
 545 the shutter will pass any pixel between 198 ± 103 mil-
 546 liseconds. Subtracting this from the fitted delay of 24.8
 547 milliseconds and adding the fitted error of 11.0 millic-
 548 onds in quadrature, results in a current conservative esti-
 549 mate of the delay of -173.2 ± 104.1 milliseconds, consis-
 550 tent with and smaller than the constraints on the tim-
 551 ing offset determined using astrometric residuals from
 552 known asteroid associations presented in §5.9.2.

2.3. Flat Field System

554 During the on-sky campaign, key components of the
 555 Rubin calibration system (P. Ingraham et al. 2022),
 556 including the flat field screen, had not yet been in-
 557 stalled. As a result, flat fielding for DP1 relied en-

⁸⁸ <https://www.nstb.tc.faa.gov/nstbarchive.html>

558 tirely on twilight flats. While twilight flats pose chal-
 559 lenges such as non-uniform illumination and star print-
 560 through, they were the only available option during
 561 LSSTComCam commissioning and for DP1 processing.
 562 To mitigate these limitations, dithered, tracked expo-
 563 sures were taken over a broad range of azimuth and rota-
 564 tor angles to construct combined flat calibration frames.
 565 Exposure times were dynamically adjusted to reach tar-
 566 get signal levels of between 10,000 and 20,000 electrons.
 567 Future campaigns with LSSTCam will benefit from more
 568 stable and uniform flat fielding using the Rubin flat field
 569 system, described in P. Fagrelus & E. S. Rykoff (2025).

2.4. LSST Science Pipelines Commissioning

571 Commissioning of the LSST Science Pipelines, (Rubin
 572 Observatory Science Pipelines Developers 2025), began
 573 once the telescope was able to routinely deliver sub-
 574 arcsecond image quality. The goals included testing the
 575 internal astrometric and photometric calibration across
 576 a range of observing conditions, validating the difference
 577 image analysis and prompt processing (K.-T. Lim 2023)
 578 framework, and accumulating over 200 visits per band
 579 to evaluate deep coadded images with integrated expo-
 580 sure times roughly equivalent to those of the planned
 581 LSST Wide-Fast-Deep (WFD) 10-year depth. To sup-
 582 port these goals, seven target fields were selected that
 583 span a range of stellar densities, overlap with external
 584 reference datasets, and collectively span the full breadth
 585 of the four primary LSST science themes. These seven
 586 fields form the basis of the DP1 dataset. Figure 4 shows
 587 the locations of these seven fields on the sky, overlaid on
 588 the LSST baseline survey footprint (R. L. Jones et al.
 589 2021; P. Yoachim 2022; Rubin’s Survey Cadence Opti-
 590 mization Committee et al. 2022, 2023, 2025), along with
 591 the sky coverage of both the LSSTCam and LSSTCom-
 592 Cam focal planes. Each of the seven target fields was
 593 observed repeatedly in multiple bands over many nights.
 594 A typical observing epoch on a given target field con-
 595 sisted of 5-20 visits in each of the three loaded filters.
 596 Only images taken as 1x30 second exposures have been
 597 included in DP1. All images were acquired using the
 598 Rubin Feature-Based Scheduler (FBS), version 3.0 (E.
 599 Naghib et al. 2019; P. Yoachim et al. 2024). Table 1 lists
 600 the seven DP1 fields and their pointing centers, and pro-
 601 vides a summary of the band coverage in each.

603 Figure 5 shows the temporal sampling of observations
 604 by filter and by night. The figure indicates the dates
 605 on which each field was observed in a given band but
 606 does not convey the total number of observations ob-
 607 tained per filter on any individual night. Gaps in cov-
 608 erage across some bands arise from the fact that LSST-
 609 ComCam can only accommodate three filters at a time

611 (see §2.2). As the campaign progressed, the temporal
 612 sampling became denser across all fields, reflecting im-
 613 proved efficiency and increased time allocated for sci-
 614 ence observations. The Extended Chandra Deep Field-
 615 South Survey (ECDFS) field received the most consis-
 616 tent and densest temporal sampling. It is important to
 617 note that the time sampling in the DP1 dataset differs
 618 significantly from what will be seen in the final LSST
 619 data. All fields except for the low ecliptic latitude field,
 620 Rubin_SV_38_7, used a small random dithering pat-
 621 tern. The random translational dithers of the telescope
 622 boresight were applied for each visit, with offsets of up to
 623 0.2 degrees around the pointing center. The rotational
 624 dithers of the camera rotator were typically approxi-
 625 mately 1 degree per visit, with larger random offsets
 626 at each filter change, which worked to keep operational
 627 efficiency high. The Rubin_SV_38_7 field used a dif-
 628 ferent dither pattern to optimize coverage of Solar Sys-
 629 tem Objects and test Solar System Object linking across
 630 multiple nights. These observations used a 2x2 grid of
 631 LSSTComCam pointings to cover an area of about 1.3
 632 degreex1.3 degrees. The visits cycled between the grid’s
 633 four pointing centers, each separated by 0.65 degrees,
 634 and used small random translational dithers to fill chip
 635 gaps with the goal of acquiring 3-4 visits per pointing
 636 center per band in each observing epoch. The RA and
 637 Dec values provided in Table 1 for this field represent
 638 approximately the center of the four fields.

639 Figure 6 shows sky coverage maps showing the distri-
 640 bution of visits in each of the seven DP1 fields, color
 641 coded by band. The images clearly show the focal plane
 642 chip gaps and dithering pattern. Only the detectors for
 643 which single frame processing succeeded are included
 644 in the plots, which explains why the central region of
 645 47_Tuc looks thinner than the other fields (see §5.10).
 646 Table 2 reports the 5 σ point source depths for coad-
 647 ded images per field and per band, where coverage in
 648 a band is non-zero, together with the expected 10-year
 649 LSST depths derived from the baseline simulated survey
 650 (F. B. Bianco et al. 2022).

2.5. Delivered Image Quality

653 The delivered image quality is influenced by contribu-
 654 tions from both the observing system (i.e., dome, tele-
 655 scope and camera) and the atmosphere. During the
 656 campaign, the Rubin Differential Image Motion Monitor
 657 (DIMM) was not operational, so atmospheric seeing was
 658 estimated using live data from the Southern Astrophys-
 659 ical Research Telescope (SOAR) Ring-Image Next Gen-
 660 eration Scintillation Sensor (RINGSS) seeing monitor,
 661 also located on Cerro Pachón. Although accelerometers
 662 mounted on the mirror cell and top-end assembly were

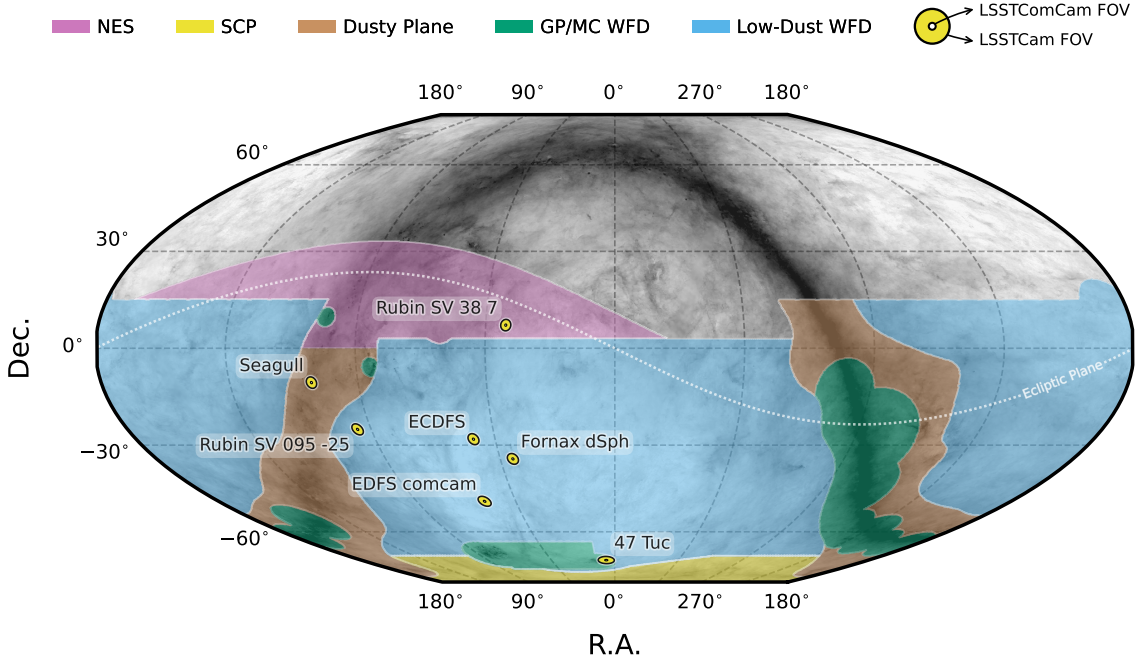


Figure 4. Locations of the seven DP1 fields overlaid on the LSST baseline survey footprint. NES: North Ecliptic Spur; SCP: South Celestial Pole; Low-Dust WFD: regions away from the Galactic Plane (GP) observed with a WFD cadence; GP/MC WFD: Galactic Plane and Magellanic Clouds regions observed with a WFD cadence. The fields of view of the LSSTCam and LSSTComCam focal planes are shown as concentric yellow circles about the pointing center of each field. The background Milky Way dust map is based on the FDS model (D. P. Finkbeiner et al. 1999).

Table 1. DP1 fields and pointing centers with the number of exposures in each band per field. ICRS coordinates are in units of decimal degrees, and are specified as J2000.

Field Code	Field Name	RA deg	Dec deg	Band					Total	
				<i>u</i>	<i>g</i>	<i>r</i>	<i>i</i>	<i>z</i>		<i>y</i>
47_Tuc	47 Tucanae Globular Cluster	6.128	-72.090	6	10	32	19	0	5	72
ECDFS	Extended Chandra Deep Field South	53.160	-28.100	43	230	237	162	153	30	855
EDFS_comcam	Rubin SV Euclid Deep Field South	59.150	-48.730	20	61	87	42	42	20	272
Fornax_dSph	Fornax Dwarf Spheroidal Galaxy	40.080	-34.450	0	5	25	12	0	0	42
Rubin_SV_095_-25	Rubin SV Low Galactic Latitude Field	95.040	-25.000	33	82	84	23	60	10	292
Rubin_SV_38_7	Rubin SV Low Ecliptic Latitude Field	37.980	7.015	0	44	40	55	20	0	159
Seagull	Seagull Nebula	106.300	-10.510	10	37	43	0	10	0	100
Total				112	469	548	313	285	65	1792

663 available to track dynamic optics effects, such as mir-
 664 ror oscillations that can degrade optical alignment, this
 665 data was not used during the campaign. Mount encoder
 666 data were used to measure the mount jitter in every im-
 667 age, with a measured median contribution of 0.004 arc-
 668 seconds to image degradation. As the pointing model
 669 was not fine tuned, tracking errors could range from 0.2
 670 to 0.4 arcseconds per image, depending on RA and Dec.

671 Dome and mirror-induced seeing were not measured dur-
 672 ing the campaign.

673 The DP1 median delivered image quality, quantified
 674 as the PSF at FWHM across all filters and target fields,
 675 is $1''.14$. The best images achieve a PSF FWHM of ap-
 676 proximately $0''.58$. Both the per-sensor PSF FWHM and
 677 the overall median vary depending on the filter and the
 678 specific target field. The median delivered image quality
 679 per band and target field is provided in Table 3. Fig-

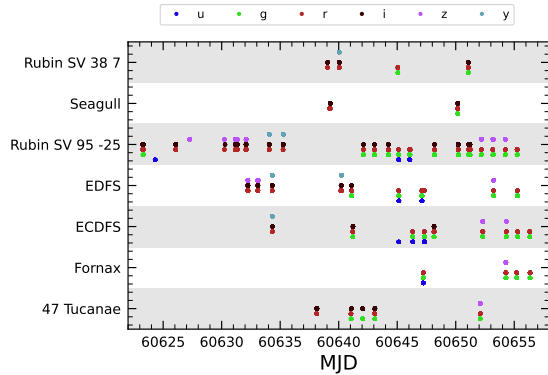


Figure 5. Temporal distribution of DP1 observations, grouped by field as a function of Modified Julian Date (MJD) and color-coded by filter. Each point indicates that a given field was observed at least once in the corresponding filter on that date.

Table 2. DP1 median 5σ coadded point-source detection limits per field and band, expressed in magnitudes, compared with the expected 10-year LSST values derived from the baseline simulated survey (F. B. Bianco et al. 2022).

Field Code	Band					
	<i>u</i>	<i>g</i>	<i>r</i>	<i>i</i>	<i>z</i>	<i>y</i>
47_Tuc	-	24.03	24.24	23.90	-	21.79
ECDFS	24.55	26.18	25.96	25.71	25.07	23.10
EDFS_comcam	23.42	25.77	25.72	25.17	24.47	23.14
Fornax_dSph	-	24.53	25.07	24.64	-	-
Rubin_SV_095_-25	24.29	25.46	24.95	24.86	24.32	22.68
Rubin_SV_38_7	-	25.46	25.15	24.86	23.52	-
Seagull	23.51	24.72	24.19	-	23.30	-
LSST 10-year	25.73	26.86	26.88	26.34	25.63	24.87

Table 3. DP1 Median image quality per field and per band quantified as the PSF at FWHM in arcseconds.

Field Code	Band						All
	<i>u</i>	<i>g</i>	<i>r</i>	<i>i</i>	<i>z</i>	<i>y</i>	
47_Tuc	-	1.27	1.25	1.11	-	1.33	1.22
ECDFS	1.40	1.14	1.08	1.00	1.00	1.07	1.08
EDFS_comcam	1.88	1.25	1.20	1.10	1.18	0.99	1.19
Fornax_dSph	-	1.16	0.82	0.93	-	-	0.85
Rubin_SV_095_-25	1.40	1.25	1.14	0.97	1.17	0.82	1.19
Rubin_SV_38_7	-	1.13	1.13	1.10	1.22	-	1.13
Seagull	1.50	1.34	1.19	-	1.19	-	1.25
All	1.48	1.17	1.12	1.03	1.11	1.01	1.13

3. OVERVIEW OF THE CONTENTS OF RUBIN DP1

In this section we describe the Rubin DP1 data products and provide summary statistics for each. For more detailed information, we refer the reader to the DOI-registered DP1 release documentation available at <https://dp1.lsst.io> and the catalog schemas available at <https://sdm-schemas.lsst.io>.⁸⁹

The DP1 science data products are derived from the 15972 individual CCD images taken across 1792 exposures in the seven LSSTComCam commissioning fields (§2.4). To aid legibility, we have separated the descriptions of the data products from the description of the data release processing pipeline (§4). Similarly, as the DP1 data products can be accessed via one or both of International Virtual Observatory Alliance (IVOA) Services (§6.2.1) or the Data Butler (§6.2.2), we describe them here in a manner that is agnostic to the means of access.

The data products that comprise DP1 provide an early preview of future LSST data releases and are strongly dependent on the type and quality of the data that was collected during the LSSTComCam on-sky campaign (§2.4). Consequently not all anticipated LSST data products, as described in the Data Product Definition Document (DPDD) (M. Jurić et al. 2023), were produced for the DP1 dataset.

Rubin Observatory has adopted the convention by which single-epoch detections are referred to as “Sources”, and the astrophysical object associated with

⁸⁹ Searchable catalog schemas are also available to Data Rights Holders via the Rubin Science Platform at <https://data.lsst.cloud>.

ure 7 shows the distribution of PSF FWHM (in arcsec) over all 16071 individual sensors images. Ongoing efforts aim to quantify all sources of image degradation, including contributions from the camera system; static and dynamic optical components; telescope mount motion; observatory-induced seeing from the dome and primary mirror; and atmospheric conditions. For the LSST, the design specification for the median delivered image quality, referenced to the zenith and 550 nm, is $0''.7$. This value corresponds to the measured median atmospheric seeing at the Cerro Pachón site and a system contribution to delivered image quality of $0''.35$ added in quadrature.

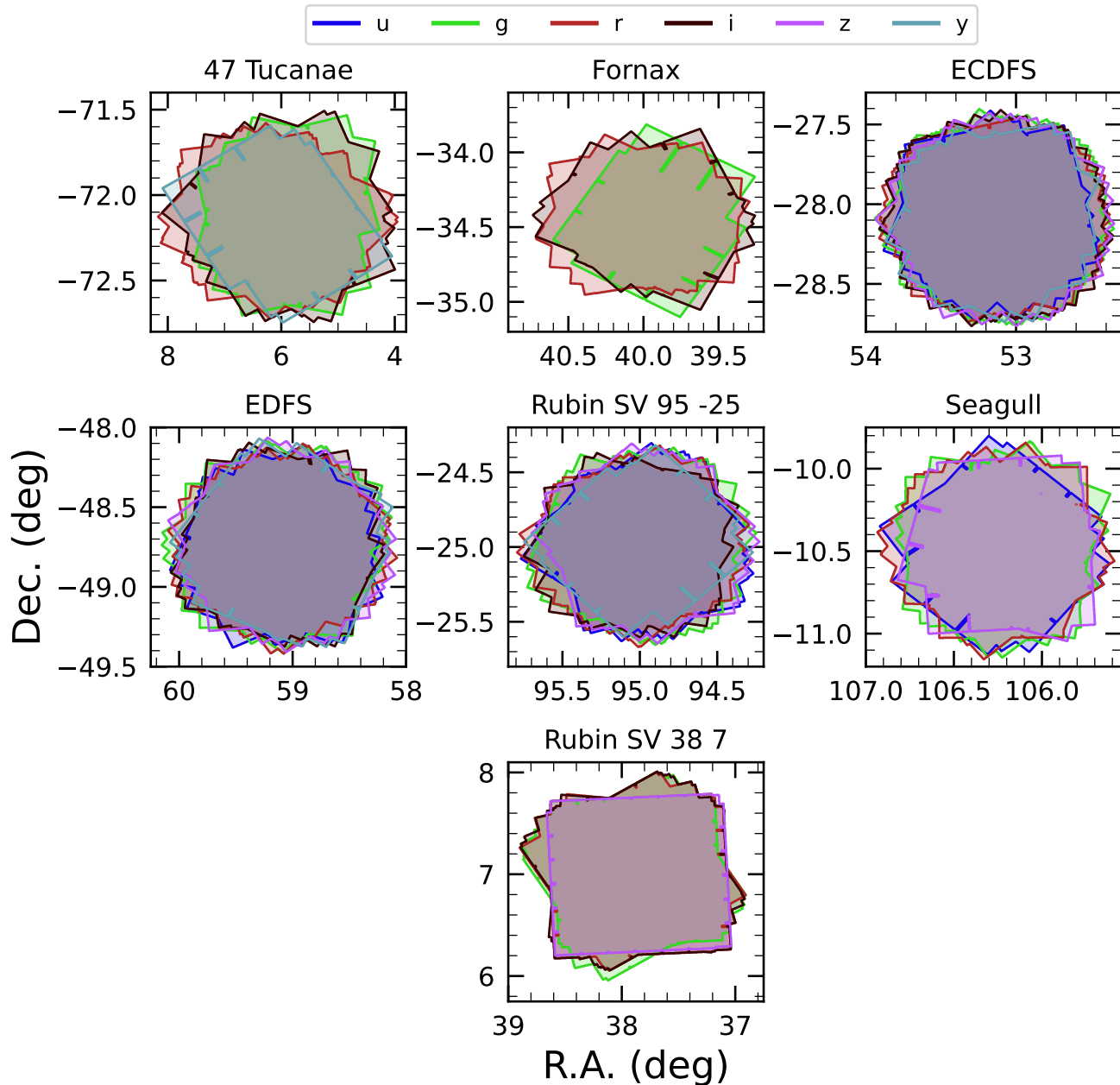


Figure 6. Sky coverage maps showing the distribution of visits in each field, color coded by band. The images clearly show the focal plane chip gaps and dithering pattern. Only the detectors for which single frame processing succeeded are included in the plots, which explains why the central region of 47_Tuc looks thinner than the other fields.

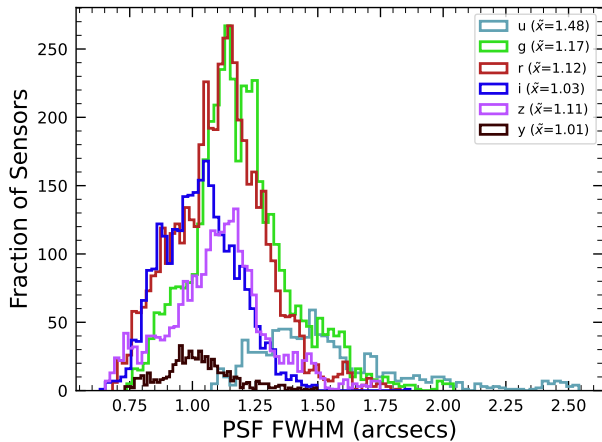
724 a given detection is referred to as an “Object”⁹⁰. As 729
 725 such, a given Object will likely have multiple associated 730
 726 Sources, since it will be observed in multiple epochs. 731

727 At the highest level, the DP1 data products fall into
 728 one of five types:

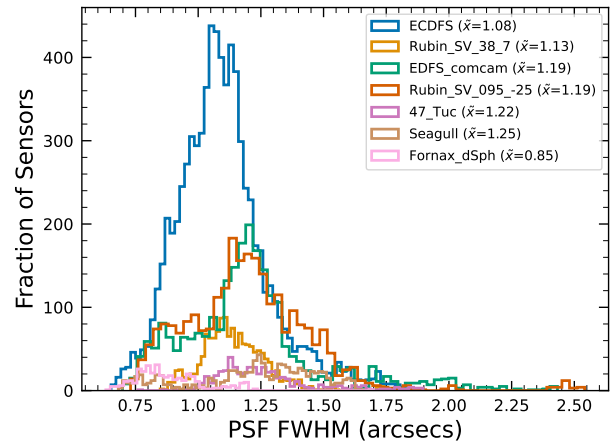
- **Science Images**, including single-epoch images, deep and template coadded images, and difference images (§3.1);

- **Catalogs** of astrophysical Sources and Objects detected and measured in the aforementioned images. We also provide the astrometric and photometric reference catalog generated from external

⁹⁰ We caution that this nomenclature is not universal; for example, some surveys use “detections” for what we call “sources”, and “sources” for what we call “objects”.



(a) PSF FWHM (arcsecs) per passband across all DP1 target fields.



(b) PSF FWHM (arcsecs) per DP1 target field across all passbands

Figure 7. Histograms showing the distribution of delivered image quality for all 16071 single-epoch individual sensors in the DP1 dataset per passband (a) and per field (b). The median values are given in the legend.

736 sources that was used during processing to gener-
737 ate the DP1 data products (§3.2);

- 738 • **Maps**, which provide non-science-level visualiza-
739 tions of the data within the release. They include,
740 for example, zoomable multi-band images and cover-
741 age maps (§3.4.1);
- 742 • **Ancillary data products**, including, for exam-
743 ple, the parameters used to configure the data pro-
744 cessing pipelines, log and processing performance
745 files, and **calibration** data products (§3.6);
- 746 • **Metadata** in the form of tables containing infor-
747 mation about each visit and processed image, such
748 as pointing, exposure time, and a range of image
749 quality summary statistics (§3.5).

750 While images and catalogs are expected to be the pri-
751 mary data products for scientific research, we also rec-
752 ognize the value of providing access to other data types
753 to support investigations and ensure transparency.

754 To facilitate processing, Rubin DP1 uses a single
755 skymap⁹¹ that covers the entire sky area encompass-
756 ing the seven DP1 fields. The DP1 skymap divides the
757 entire celestial sphere into 18938 **tracts**, each covering
758 approximately 2.8 deg^2 . The **tracts** are arranged in rings
759 of declination, ordered from south to north, then with
760 increasing right ascension within a ring. Each **tract** is
761 further subdivided into 10×10 equally-sized patches.

⁹¹ A skymap is a tiling of the celestial sphere, organizing large-
scale sky coverage into manageable sections for processing and
analysis. While the skymap described here is specific to DP1,
we do not anticipate major changes to the skymap in future
data releases.

762 Both **tracts** and patches overlap with their neighboring
763 regions. The amount of overlap between **tracts** changes
764 with declination, with **tracts** nearest the poles having
765 the greatest degree of overlap; the minimum overlap be-
766 tween **tracts** is $1'0$. By contrast, the amount of overlap
767 between patches is constant, with each **patch** overlap-
768 ping each of its neighbouring patches by $80'0$. Each
769 patch covers 0.036 deg^2 which, due to the patch over-
770 lap, is slightly larger than the tract area divided by the
771 number of patches in a tract. The aerial coverage of
772 a patch is comparable to, but somewhat smaller than,
773 the 0.058 deg^2 field-of-view of a single LSSTComCam or
774 LSSTComCam detector, meaning each detector image spans
775 multiple patches. The size of a tract is larger than the
776 LSSTComCam field of view. However, since each ob-
777 served field extends across more than one tract, each
778 field covers multiple tracts.

779 The skymap is integral to the production of co-added
780 images. To create a coadded image, the processing
781 pipeline selects all calibrated science images in a given
782 field that meet specific quality thresholds (§3.1 and
783 §4.5.1) for a given **patch**, warps them onto a single
784 consistent pixel grid for that **patch**, as defined by the
785 skymap, then coadds them. Each individual coadd im-
786 age therefore covers a single **patch**.

787 Throughout this section, the data product names are
788 indicated using monospace font. Data products are ac-
789 cessed via either the IVOA Services (§6.2.1) or the Data
790 Butler (§6.2.2).

3.1. Science Images

792 Science images are exposures of the night sky, as dis-
793 tinct from **calibration** images (§3.6.3). Although the re-
794 lease includes **calibration** images, thereby allowing users

Table 4. Number of **raw** images per field and band. Each raw image corresponds to a single 30-second LSSTComCam exposure on one CCD. Most exposures produce nine raw images, one per sensor in the focal plane, however some yield fewer due to occasional hardware or readout issues.

Field Code	Band						Total
	<i>u</i>	<i>g</i>	<i>r</i>	<i>i</i>	<i>z</i>	<i>y</i>	
47_Tuc	54	90	288	171	0	45	648
ECDFS	387	2070	2133	1455	1377	270	7692
EDFS_comcam	180	549	783	378	378	180	2448
Fornax_dSph	0	45	225	108	0	0	378
Rubin_SV_095_-25	297	738	756	207	540	90	2628
Rubin_SV_38_7	0	396	360	495	180	0	1431
Seagull	90	333	387	0	90	0	900
Total	1008	4221	4932	2814	2565	585	16125

to reprocess the raw images if needed, this is expected to be necessary only in rare cases. Users are strongly encouraged to start from the `visit_image` provided. The data product names shown here are those used by the Data Butler, but the names used in the IVOA Services differ only slightly in that they are prepended by “`lsst.`”.

3.1.1. Raw Image

raw images (NSF-DOE Vera C. Rubin Observatory 2025b) are unprocessed data received directly from the camera. Each **raw** corresponds to a single CCD from a single LSSTComCam exposure of 30 s duration. Each LSSTComCam exposure typically produces up to nine **raws**, one per sensor in the focal plane. However, a small number of exposures resulted in fewer than nine **raw** images due to temporary hardware issues or readout faults.

In total, DP1 includes 16125 raw images. Table 4 provides a summary by target and band. A **raw** contains 4608×4096 pixels, including prescan and overscan, and occupies around 18 MB of disk space.⁹² The field of view of a single **raw**, excluding prescan and overscan regions, is roughly $0^\circ 23' \times 0^\circ 22' \approx 0.051 \text{ deg}^2$, corresponding to a plate scale of $0''.2$ per pixel.

⁹² Each amplifier image contains 3 and 64 columns of serial prescan and overscan pixels, respectively, and 48 rows of parallel overscan pixels, meaning a **raw** contains 4072×4000 exposed pixels.

3.1.2. Visit Image

`visit_images` (NSF-DOE Vera C. Rubin Observatory 2025c) are fully-calibrated processed images. They have undergone instrument signature removal (§4.2.1) and all the single frame processing steps described in §4.2 which are, in summary: PSF modeling, background subtraction, and astrometric and photometric calibration. As with **raws**, a `visit_image` contains processed data from a single CCD resulting from a single 30 s LSSTComCam exposure. As a consequence, a single LSSTComCam exposure typically results in nine `visit_images`. The handful of exposures with fewer than nine **raw** images also have fewer than nine `visit_images`, but there are an additional 153 **raw** images that failed processing and for which there is thus no corresponding `visit_image`. The majority of failures – 131 in total – were due to challenges with astrometric fits or PSF models in the 47_Tuc crowded field. The other failures were in the Rubin_SV_095_-25 (9 failures), ECDFS (8), Fornax_dSph (3), and EDFs_comcam (2) fields.

In total, there are 15972 `visit_images` in DP1. Each `visit_image` comprises three images: a calibrated science image, a variance image, and a pixel-level bit-mask that flags issues such as saturation, cosmic rays, or other artifacts. Each `visit_image` also contains a position-dependent PSF model, World Coordinate System (WCS) information, and various metadata providing information about the observation and processing. The science and variance images and the pixel mask each contain 4072×4000 pixels. In total, a single `visit_image`, including all extensions and metadata, occupies around 110 MB of disk space. A plot showing the normalized cumulative histogram of the 5σ depths of all the `visit_images` in DP1 is shown in Figure 8.

3.1.3. Deep Coadd

`deep_coadds` are created on a per-band basis, meaning only data from exposures taken with a common filter are coadded. As such, there are up to six `deep_coadds` covering each `patch` – one for each of the six LSSTComCam bands. The process of producing `deep_coadds` is described in §4.5 but, to summarize, it involves the selection of suitable `visit_images` (both in terms of `patch` coverage, band, and image quality), the warping of those `visit_images` onto a common pixel grid, and the co-adding of the warped `visit_images`. To be included in a DP1 `deep_coadd`, a `visit_image` needed to have a PSF FWHM smaller than $1''.7$. Of the 15972 `visit_images`, 15375 satisfied this criterion and were therefore used to create `deep_coadds`.

There are a total of 2644 `deep_coadds` in DP1. As mentioned above, a single `deep_coadd` covers one `patch`,

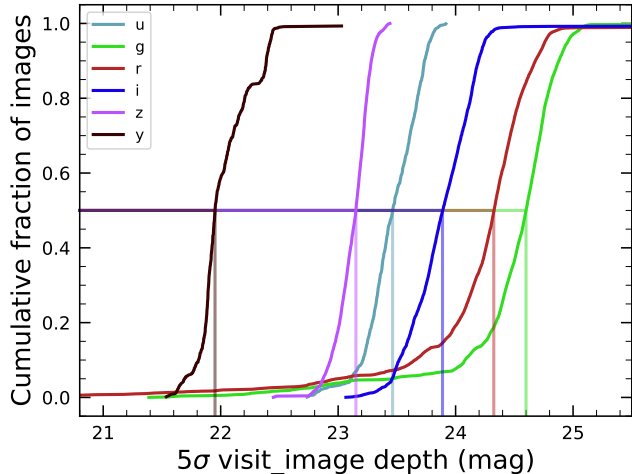


Figure 8. Normalized cumulative histograms of the 5σ depths of all `visit_images` in each band. The vertical lines indicate the 50th percentiles for each band (see legend).

and includes a small amount of overlap with its neighboring `patch`. The skymap used for DP1 defines a `patch` as having an on-sky area of 0.028 deg^2 excluding overlap, and 0.036 deg^2 including overlap. A single `deep_coadd` – including overlap – contains 3400×3400 equal-sized pixels, corresponding to a platescale of $0''.2$ per pixel. Each `deep_coadd` contains the science image (i.e., the coadd), a variance image, and a pixel mask; all three contain the same number of pixels. Each `deep_coadd` also contains a position-dependent PSF model (which is the weighted sum of the PSF models of the input `visit_images`), WCS information, plus various `meta-data`.

The number of `visit_images` that contributed to a given `deep_coadd` varies across the patch; the Survey Property Maps can be consulted to gain insights into the total exposure time at all locations covered by the survey. Similarly, since coadds always cover an entire `patch`, it is common for a `deep_coadd` to contain regions that were not covered by any of the selected `visit_images`, particularly if the `patch` is on the outskirts of a field and was thus not fully observed. By the nature of how coadds are produced, such regions may contain seemingly valid `flux` values (i.e., not necessarily zeros or NaNs), but will instead be flagged with the `NO_DATA` flag in the pixel mask. It is therefore crucial that the pixel mask be referred to when analyzing `deep_coadds`.

3.1.4. Template Coadd

`template_coadds` (NSF-DOE Vera C. Rubin Observatory 2025d) are those created to use as templates for difference imaging, i.e., the process of subtracting a template image from a `visit_image` to identify either vari-

able or `transient` objects. It should be noted, however, that `template_coadds` are not themselves subtracted from `visit_images` but are, instead, warped to match the WCS of a `visit_image`. It is this warped template that is subtracted from the `visit_image` to create a difference image.⁹³ As with `deep_coadds`, `template_coadds` are produced by warping and co-adding multiple `visit_images` covering a given skymap-defined `patch`. The process of building `template_coadds` is the same as that for `deep_coadds`, but the selection criteria differ between the two types of coadd. In the case of `template_coadds`, one third of `visit_images` covering the `patch` in question with the narrowest PSF FWHM are selected. If one third corresponds to fewer than twelve `visit_images` (i.e., there are fewer than 36 `visit_images` covering the `patch`), then the twelve `visit_images` with the narrowest PSF FWHM are selected. Finally, if there are fewer than twelve `visit_images` covering the `patch`, then all `visit_images` are selected. Of the 15972 `visit_images`, 13113 were used to create `template_coadds`. This selection strategy is designed to optimize for seeing when a `patch` is well-covered by `visit_images`, yet still enable the production of `template_coadds` for poorly-covered patches. As with `deep_coadds`, the number of `visit_images` that contributed to a `template_coadd` varies across the patch.

DP1 contains a total of 2730 `template_coadds`.⁹⁴ As with `deep_coadds`, a single `template_coadd` covers a single `patch`. Since the same skymap is used when creating both `deep_coadd` and `template_coadds`, the on-sky area and pixel count of `template_coadds` are the same as that of a `deep_coadd` (see above). Similarly, `template_coadds` contain the science image (i.e., the coadd), a variance image, and a pixel mask; all three contain the same number of pixels. Also included are the PSF model, WCS information, and `metadata`. As is the case for `deep_coadds`, those pixels within `template_coadds` that are not covered by any of the selected `visit_images` may still have seemingly valid values, but are indicated with the `NO_DATA` flag within the pixel mask.

3.1.5. Difference Image

`difference_images` (NSF-DOE Vera C. Rubin Observatory 2025e) are generated by the subtraction of the warped, scaled, and PSF-matched `template_coadd`

⁹³ For storage space reasons, warped templates are not retained for DP1, as they can be readily and reliably recreated from the `template_coadds`.

⁹⁴ The difference in the number of `deep_coadds` and `template_coadds` is due to the difference in the `visit_image` selection criteria for each coadd.

from the `visit_image` (see §4.6.1). In principle, only those sources whose `flux` has changed relative to the `template_coadd` should be apparent (at a significant level) within a `difference_image`. In practice, however, there are numerous spurious sources present in `difference_images` due to unavoidably imperfect template matching.

In total, there are 15972 `difference_images` in DP1, one for each `visit_image`.

Like `visit_images`, `difference_images` contain the science (i.e., difference) image, a variance image, and a pixel mask; all three contain the same number of pixels, which is the same as that of the input `visit_image`. Also included is the PSF model, WCS information, and `metadata`.

3.1.6. Background Images

Background images contain the model `background` that has been generated and removed from a science image. `visit_images`, `deep_coadds` and `template_coadds` all have associated `background` images.⁹⁵ Background images contain the same number of pixels as their respective science image, and there is one `background` image for each `visit_image`, `deep_coadd`, and `template_coadd`. Difference imaging analysis also measures and subtracts a `background` model, but the `difference_background` data product is not written out by default and is not part of DP1.

Background images are not available via the IVOA Service; they can only be accessed via the Butler Data Service.

3.2. Catalogs

In this section we describe science-ready tables produced by the science pipelines. All catalogs contain data for detections in the images described in §3.1, except the `Calibration` catalog, which contains reference data obtained from previous surveys. Observatory-produced `metadata` tables are described in §3.5.

The catalogs contains measurements for either Sources detected in `visit_images` and `difference_images`, or Objects detected in `deep_coadds`. All catalogs store fluxes rather than magnitudes, with fluxes measured in nanojansky ($1 \text{ nJy} = 10^{-35} \text{ Wm}^{-2}\text{Hz}^{-1}$). Fluxes are preferred for multi-epoch observations, as they can be averaged across epochs, unlike magnitudes. Additionally, flux measurements on difference images (§3.1) are computed against a template, representing a flux difference. As a result, flux measurements on difference

images can be negative, particularly for faint sources in the presence of noise.

The `Source`, `Object`, `ForcedSource`, `DiaSource`, `DiaObject`, and `ForcedSourceOnDiaObject` catalogs described below each vary in terms of their specific columns but generally contain: one or more unique identification numbers, positional information, multiple types of `flux` measurements (e.g., aperture fluxes, PSF fluxes, Gaussian fluxes, etc.), and a series of boolean flags indicating characteristics such as saturation or cosmic ray contamination for each source/object. The Solar System catalogs `SSObject` and `SSSource` deviate from this general structure in that they instead contain orbital parameters for all known asteroids.

Where applicable, quantities are prefixed with the band in which they were measured, and all measured properties are reported with their associated 1σ uncertainties. For example, `g_ra` and `g_raErr` refer to right ascension and its uncertainty, measured in the g-band.

Fluxes for various apertures are provided together with an uncertainty and a flag, and named in the format `[band]_ap[size]Flux`, where `[size]` is the aperture diameter in pixels. For example, `g_ap03Flux`, `g_ap03FluxErr`, `g_ap03Flux_flag` provide the flux, uncertainty and flag measured within a 3.0-pixel aperture in the g-band. Similarly for flux measurements using difference algorithms, e.g. `g_psfFlux` provides the flux derived using the PSF model as a weight function, forced on g-band.

A complete list of columns with description and units for all tables in DP1 is available at <https://sdm-schemas.lsst.io/dp1.html> Since DP1 is a preview release, it does not include all the catalogs expected in a full LSST Data Release. Additionally, some catalogs may be missing columns, as not all quantities have been computed yet. These quantities will be included in future releases, and, where it is known to be the case, missing data are noted in the catalog descriptions that follow.

Catalog data are stored in the Qserv database (§6.5.1) and are accessible via Table Access Protocol (IVOA standard) (IVOA), and an online DP1 catalog schema is available at <https://sdm-schemas.lsst.io/dp1.html>. Catalog data are also accessible via the Data Butler (see §6.2.2).

3.2.1. Source Catalog

The `Source` catalog (NSF-DOE Vera C. Rubin Observatory 2025f) contains data on all sources which are, prior to deblending (§4.5.2), detected with a greater than 5σ significance in each individual visit. The detections reported in the `Source` catalog have undergone deblending; in the case of blended detections, only the

⁹⁵ In future data releases, `background` images may be included as part of their respective science image data product.

deblended sources are included in the `Source` catalog. It is important to note that while the criterion for inclusion in a `Source` catalog is a $> 5\sigma$ detection in a `visit_image` prior to deblending, the positions and fluxes are reported post-deblending. Hence, it is possible for the `Source` catalog to contain sources whose flux-to-error ratios – potentially of all types (i.e., aperture flux, PSF flux, etc.) – are less than 5.

In addition to the general information mentioned above (i.e., IDs, positions, fluxes, flags), the `Source` catalog also includes basic `shape` and extendedness information.

The `Source` catalog contains data for 46 million sources in DP1.

A cumulative histogram showing the PSF magnitudes of all sources contained within the `Source` catalogue is presented in the top panel of Figure 9

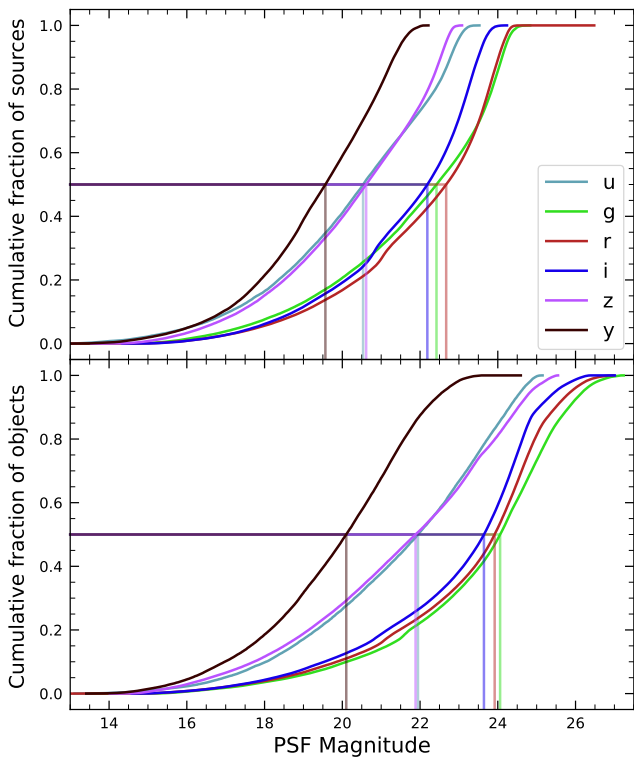


Figure 9. Normalized cumulative histograms of the PSF magnitudes of all $> 5\sigma$ -detected sources (top panel) and objects (bottom panel) contained in the `Source` and `Object` catalogs, respectively, separated according to band (see legend). The vertical lines indicate the 50th percentile for each band.

3.2.2. Object Catalog

The `Object` catalog (NSF-DOE Vera C. Rubin Observatory 2025g) contains data on all objects detected with a greater than 5σ significance in the `deep_coadds`.

With coadd images produced on a per-band basis, a $> 5\sigma$ detection in one or more of the bands will result in an object being included in the `Object` catalog. For cases where an object is detected at $> 5\sigma$ in more than one band, a cross-matching has been performed between bands to associate an object in one band with its counterpart(s) in the other bands. As such, the `Object` catalog contains data from multiple bands. The objects reported in the `Object` catalog have also undergone deblending; in the case of blended detections, only the deblended child objects are included in the catalog. As with the `Source` catalog, the criterion for inclusion in the `Object` catalog is a $> 5\sigma$ detection in one of the `deep_coadds` prior to deblending, yet the positions and fluxes of objects are reported post-deblending. Hence, it is possible for `Object` catalog to contain objects whose flux-to-error ratios — potentially of all types and in all bands — are less than 5.

In addition to the general information mentioned above (i.e., IDs, positions, fluxes, flags), the `Object` catalog also includes basic `shape` and extendedness information. While they may be included in future data releases, no photometric redshifts, Petrosian magnitudes (V. Petrosian 1976), proper motions or periodicity information are included in the DP1 object catalogs.

The `Object` catalog contains data for 2.3 million objects in DP1.

3.2.3. ForcedSource Catalog

The `ForcedSource` catalog (NSF-DOE Vera C. Rubin Observatory 2025h) contains forced PSF photometry measurements performed on both `difference_images` (i.e., the `psfDiffFlux` column) and `visit_images` (i.e., the `psfFlux` column) at the positions of all the objects in the `Object` catalog, to allow assessment of the time variability of the fluxes. We recommend using the `psfDiffFlux` column when generating light curves because this quantity is less sensitive to flux from neighboring sources than `psfFlux`. In addition to forced photometry PSF fluxes, a number of boolean flags are also included in the `ForcedSource` catalog.

The `ForcedSource` catalog contains a total of 269 million entries across 2.3 million unique objects.

3.2.4. DiaSource Catalog

The `DiaSource` catalogs (NSF-DOE Vera C. Rubin Observatory 2025i) contains data on all the sources detected at $> 5\sigma$ significance — including those associated with known Solar System objects — in the `difference_images`. Unlike sources detected in `visit_images`, sources detected in difference images (hereafter, “DiaSource”) have gone through an association step in which an attempt has been made to associate them into

underlying objects called “DiaObject”. The `DiaSource` catalog consolidates all this information across multiple visits and bands. The detections reported in the `DiaSource` catalog have not undergone deblending.

The `DiaSource` catalog contains data for 3.1 million `DiaSources` in [DP1](#).

3.2.5. *DiaObject Catalog*

The `DiaObject` catalog ([NSF-DOE Vera C. Rubin Observatory 2025j](#)) contains the astrophysical objects that `DiaSources` are associated with (i.e., the `DiaObjects`). The `DiaObject` catalog contains only non-Solar System Objects; Solar System Objects are, instead, recorded in the `SSObject` catalog. When a `DiaSource` is identified, the `DiaObject` and `SSObject` catalogs are searched for objects to associate it with. If no association is found, a new `DiaObject` is created and the `DiaSource` is associated to it. Along similar lines, an attempt has been made to associate `DiaObjects` across multiple bands, meaning the `DiaObject` catalog, like the `Object` catalog, contains data from multiple bands. Since `DiaObjects` are typically [transient](#) or variable (by the nature of their means of detection), the `DiaObject` catalog contains summary statistics of their fluxes, such as the mean and standard deviation over multiple epochs; users must refer to the `ForcedSourceOnDiaObject` catalog (see below) or the `DiaSource` catalog for single [epoch flux](#) measurements of `DiaObjects`.

The `DIAObject` catalog contains data for 1.1 million `DiaObjects` in [DP1](#).

3.2.6. *ForcedSourceOnDiaObject Catalog*

The `ForcedSourceOnDiaObject` catalog ([NSF-DOE Vera C. Rubin Observatory 2025k](#)) is equivalent to the `ForcedSource` catalog, but contains [forced photometry](#) measurements obtained at the positions of all the `DiaObjects` in the `DiaObject` catalog.

The `ForcedSourceOnDiaObject` catalog contains a total of 197 million entries across 1.1 million unique `DiaObjects`.

3.3. *SSObject Catalog*

The `SSObject` catalog ([NSF-DOE Vera C. Rubin Observatory 2025l](#)) and the [Minor Planet Center Orbit database \(MPCORB\)](#) carry information about solar system objects. The `MPCORB` table provides the [Minor Planet Center](#)-computed orbital elements for all known asteroids, including those that Rubin discovered. For [DP1](#), the `SSObject` catalog serves primarily to provide the mapping between the [International Astronomical Union \(IAU\)](#) designation of an object (listed in `MPCORB`), and the internal `ssObjectId` identifier,

which is used as a key to find solar system object observations in the `DiaSource` and `SSSource` tables. The `SSObject` catalog contains data for 431 `SSObjects` in [DP1](#).

3.3.1. *SSSource Catalog*

The `SSSource` catalog ([NSF-DOE Vera C. Rubin Observatory 2025m](#)) contains data on all `DiaSources` that are either associated with previously-known Solar System Objects, or have been confirmed as newly-discovered Solar System Objects by confirmation of their orbital properties. As entries in the `SSSource` catalog stem from the `DiaSource` catalog, they have all been detected at $> 5\sigma$ significance in at least one band. The `SSSource` catalog contains data for 5988 Solar System Sources.

3.3.2. *CcdVisit Catalog*

The `CcdVisit` catalog ([NSF-DOE Vera C. Rubin Observatory 2025n](#)) contains data for all `CCD` images from a single visit. In principle, this means nine entries per visit, however due to a variety of technical reasons, not all `CCDs` have data for each visit, and so the catalog may contain fewer than nine entries per visit. In addition to technical information, such as the on-sky coordinates of the central pixel and measured pixel scale, the `CcdVisit` catalog contains a range of data quality measurements, such as whole-image summary statistics for the `PSF` size, zeropoint, sky [background](#), sky noise, and quality of astrometric solution. It provides an efficient method to access `visit_image` properties without needing to access the image data. When combined with the data contained in the `Visit` table described in [§3.5](#), it provides a full picture of the telescope pointing and sky conditions at the time of observation.

The `CcdVisit` catalog contains 16071 entries (nine entries for each of the 1786 visits, minus three entries for one incomplete visit). This differs from the number of `visit_images` due to the more stringent requirements imposed to generate a science-ready image.

3.3.3. *Calibration Catalog*

The `Calibration` catalog is the reference catalog that was used to perform astrometric and photometric [calibration](#). It is a whole-sky catalog built specifically for [LSST](#), as no single prior reference catalog had both the depth and coverage needed to calibrate [LSST](#) data. It combines data from multiple previous reference catalogs and contains only stellar sources. Full details on how the `Calibration` catalog was built are provided in [P. S.](#)

1214 Ferguson et al. (2025)⁹⁶. We provide a brief summary
1215 here.

1216 For the *grizy* bands, the input catalogs were (in order
1217 of decreasing priority): Dark Energy Survey (DES)
1218 Y6 Calibration Stars (E. S. Rykoff et al. 2023); Gaia-
1219 B or R Photometry (Gaia) (XP) Synthetic Magnitudes
1220 (Gaia Collaboration et al. 2023a); the Panoramic Survey
1221 Telescope and Rapid Response System (Pan-STARRS)1
1222 3PI Survey (K. C. Chambers et al. 2016); Data Release
1223 2 of the SkyMapper survey (C. A. Onken et al. 2019);
1224 and Data Release 4 of the VLT Survey Telescope (VST)
1225 Asteroid Terrestrial-impact Last Alert System (ATLAS)
1226 survey (T. Shanks et al. 2015). For the *u*-band, the input
1227 catalogs were (in order of decreasing priority): Standard
1228 Stars from Sloan Digital Sky Survey (SDSS) Data Re-
1229 lease 16 (R. Ahumada et al. 2020); Gaia-XP Synthetic
1230 Magnitudes (Gaia Collaboration et al. 2023a); and syn-
1231 thetic magnitudes generated using Single Lens Reflex
1232 (SLR), which estimates the *u*-band flux from the *g*-band
1233 flux and *g-r* colors. This SLR estimates were used to
1234 boost the number of *u*-band reference sources, as other-
1235 wise the source density from the *u*-band input catalogs
1236 is too low to be useful for the LSST.

1237 Only stellar sources were selected from each input cat-
1238 alog. Throughout, the Calibration catalog uses the
1239 DES bandpasses for the *grizy* bands and the SDSS band-
1240 pass for the *u*-band; color transformations derived from
1241 high quality sources were used to convert fluxes from the
1242 various input catalogs (some of which did not use the
1243 DES/SDSS bandpasses) to the respective bandpasses.
1244 All sources from the input catalogs are matched to Gaia-
1245 Data Release 3 (DR3) sources for robust astrometric in-
1246 formation, selecting only isolated sources (i.e., no neigh-
1247 bors within 1").

1248 After collating the input catalogs and transforming
1249 the fluxes to the standard DES/SDSS bandpasses, the
1250 catalog was used to identify sources within a specific
1251 region of the sky. This process generated a set of stan-
1252 dard columns containing positional and flux informa-
1253 tion, along with their associated uncertainties.

1254 3.3.4. Source and Object Designations

1255 To refer to individual sources or objects from the DP1
1256 catalogs, one should follow the LSST DP1 naming con-
1257 vention that has been registered with the International
1258 Astronomical Union. Because the Source, Object, Di-
1259 aSource, DiaObject, and SSObject tables each have
1260 their own unique IDs, their designations should differ.

⁹⁶ In P. S. Ferguson et al. (2025), the calibration reference catalog is referred to as “The Monster”. This terminology is also carried over to the DP1 Butler.

1261 In general, source and object designations should be-
1262 gin with the string “LSST-DP1” (denoting the Legacy
1263 Survey of Space and Time, Data Preview 1), followed
1264 by a string specifying the table from which the source
1265 was obtained. These strings should be “O” (for the Ob-
1266 ject table), “S” (Source), “DO” (DiaObject), “DS”
1267 (DiaSource), or “SSO” (SSObject). Following the table
1268 identifier, the designation should contain the full unique
1269 numeric identifier from the specified table (i.e., the ob-
1270 jectId, sourceId, diaObjectId, diaSourceId, or ssObject-
1271 Id). Each component of the identifier should be sep-
1272 arated by dashes, resulting in a designation such as
1273 “LSST-DP1-TAB-123456789012345678”. In summary,
1274 source designations should adhere to the formats listed
1275 below:

- 1276 • Object: LSST-DP1-O-609788942606161356 (for
1277 objectId 609788942606161356)
- 1278 • Source: LSST-DP1-S-600408134082103129 (for
1279 sourceId 600408134082103129)
- 1280 • DiaObject: LSST-DP1-DO-609788942606140532
1281 (for diaObjectId 609788942606140532)
- 1282 • DiaSource: LSST-DP1-DS-600359758253260853
1283 (for diaSourceId 600359758253260853)
- 1284 • SSObject: LSST-DP1-SSO-21163611375481943
1285 (for ssObjectId 21163611375481943)

1286 Tables that were not explicitly mentioned in the de-
1287 scription above do not have their own unique IDs, but
1288 are instead linked to one of the five tables listed above
1289 via a unique ID. For example, the ForcedSource table
1290 uses objectId, ForcedSourceOnDiaObject uses diaOb-
1291 jectId, SSSource uses diaSourceId and ssObjectId, and
1292 MPCORB uses ssObjectId.

1293 3.4. Maps

1294 Maps are two-dimensional visualizations of survey
1295 data. In DP1, these fall into two categories: Sur-
1296 vey Property Maps and Hierarchical Progressive Survey
1297 (HiPS) Maps (P. Fernique et al. 2015).

1298 3.4.1. Survey Property Maps

1299 Survey Property Maps (NSF-DOE Vera C. Rubin Ob-
1300 servatory 2025o) summarize how properties such as ob-
1301 serving conditions or exposure time vary across the ob-
1302 served sky. Each map provides the spatial distribution
1303 of a specific quantity at a defined sky position for each
1304 band by aggregating information from the images used
1305 to make the deep_coadd. Maps are initially created per-
1306 tract and then combined to produce a final consolidated

map. At each sky location, represented by a spatial pixel in the Hierarchical Equal-Area iso-Latitude Pixelisation (HEALPix)(K. M. Górski et al. 2005) grid, values are derived using statistical operations, such as minimum, maximum, mean, weighted mean, or sum, depending on the property.

DP1 contains 14 survey property maps. The available maps describe total exposure times, observation epochs (one each for the earliest, mean, and latest observation epoch), PSF size and shape (one for each of the e^1 and e^2 shape parameters; see §5.2), PSF magnitude limits, sky background and noise levels, as well as astrometric shifts (one each for right ascension and declination) and PSF distortions (one for each of the e^1 and e^2 shape parameters) due to wavelength-dependent atmospheric Differential Chromatic Refraction (DCR) effects. They all use the dataset type format `deep_coadd_<PROPERTY>_consolidated_map_<STATISTIC>`. For example, `deep_coadd_exposure_time_consolidated_map_sum` provides a spatial map of the total exposure time accumulated per sky position in units of seconds. All maps are stored in HealSparse⁹⁷ format. Survey property maps are only available via the Data Butler (§6.2.2).

Figure 10 presents three survey property maps for exposure time, PSF magnitude limit, and sky noise, computed for representative tracts and bands. Because full consolidated maps cover widely separated tracts, we use clipped per-tract views here to make the spatial patterns more discernible.

3.4.2. HiPS Maps

HiPS Maps (P. Fernique et al. 2015), offer an interactive way to explore seamless, multi-band tiles of the sky regions covered by DP1, allowing for smooth panning and zooming. DP1 provides multi-band HiPS images created by combining data from individual bands of `deep_coadd` and `template_coadd` images, using an improved version (Lust et al. in prep) of the algorithm presented in R. Lupton et al. (2004). These images are false-color representations generated using various filter combinations for the red, green, and blue channels.

The available filter combinations include `gri`, `izy`, `riz`, and `ugr` for both `deep_coadd` and `template_coadd`. Additionally, for `deep_coadd` only, we provide color blends such as `uug` and `grz`. Post-DP1, we plan to also provide single-band HiPS images for all `ugrizy` bands in both Portable Network Graphics (PNG) and FITS formats.

HiPS maps are only accessible through the HiPS viewer in the RSP Portal (§6.3) and cannot be accessed via the Data Butler (§6.2.2). All multi-band HiPS images are provided in PNG format.

3.5. Metadata

DP1 also includes metadata about the observations, which are stored in the `Visit` table. We distinguish it from a catalog as the data it contains was produced by the observatory directly, rather than the science pipelines. The `Visit` table contains technical data for each visit, such as telescope pointing, camera rotation, airmass, exposure start and end time, and total exposure time. Some of the information contained within the `Visit` table is also contained in the `CCDVisit` catalogue described in §3.2 (e.g., exposure time), although the latter also includes information produced by the processing pipelines at a per-detector level, such as the PSF size and limiting magnitudes of a given `visit_image`.

3.6. Ancillary Data Products

DP1 also includes several ancillary data products. While we do not expect most users to need these, we describe them here for completeness. All the Data Products described in this section can only be accessed via the Data Butler (§6.2.2).

3.6.1. Standard Bandpasses

Figure 3 shows the full-system throughput of the six LSSTComCam filters. The corresponding transmission curves are provided as a DP1 data product. These datasets tabulate the full-system transmission of the six LSSTComCam filters as a function of wavelength and were used as a reference for the LSSTComCam DP1 photometry. The `standard_passband` dataset is keyed by band and is stored in Astropy Table format.

3.6.2. Task configuration, log, and metadata

DP1 includes provenance-related data products such as task logs, configuration files, and task metadata. Configuration files record the parameters used in each processing task, while logs and metadata contain information output during processing. These products help users understand the processing setup and investigate potential processing failures.

3.6.3. Calibration Data Products

Calibration data products include a variety of images and models that are used to characterize and correct the performance of the camera and other system components. These include bias, dark, and flat-field images,

⁹⁷ A sparse HEALPix representation that efficiently encodes data values on the celestial sphere. <https://healsparse.readthedocs.io>

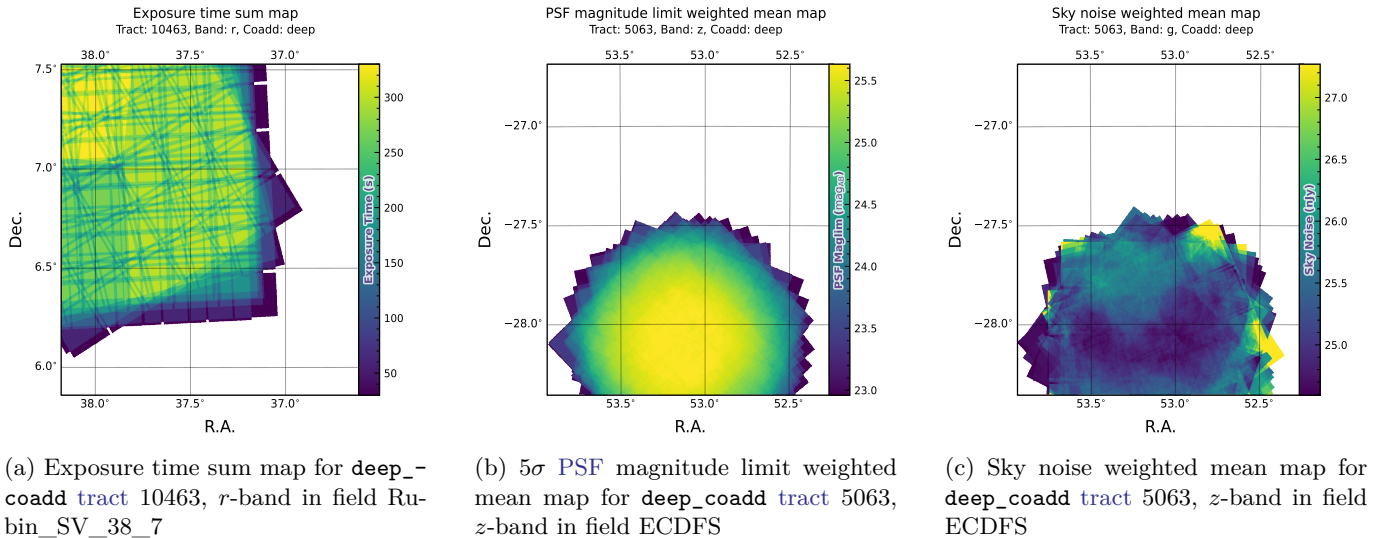


Figure 10. Examples of survey property maps from Rubin DP1 across different bands, clipped to the boundary of a single tract for visual clarity.

1401 Photon Transfer Curve (PTC) gains, brighter-fatter kernels
 1402 (P. Antilogus et al. 2014), charge transfer inefficiency
 1403 (CTI) models, linearizers, and illumination corrections.
 1404 For flat-field corrections, DP1 processing used
 1405 combined flats, which are averaged from multiple indi-
 1406 vidual flat-field exposures to provide a stable calibra-
 1407 tion. These calibration products are essential inputs
 1408 to Instrument Signal Removal (ISR) (§4.2.1). While
 1409 these products are included in DP1 for transparency and
 1410 completeness, users should not need to rerun ISR for
 1411 their science and are advised to start with the processed
 1412 visit_image.

1413 4. DATA RELEASE PROCESSING

1414 Data Release Processing (DRP) is the systematic pro-
 1415 cessing of all Rubin Observatory data collected up to
 1416 a certain date to produce the calibrated images, cata-
 1417 logs of detections, and derived data products described
 1418 in Section 3. DP1 was processed entirely at the United
 1419 States Data Facility (USDF) at SLAC using 17,024 CPU
 1420 hours.⁹⁸

1421 This section describes the pipeline algorithms used to
 1422 produce DP1 and how they differ from those planned for
 1423 full-scale LSST data releases. Data Release Production
 1424 consists of four major stages: (1) single-frame process-
 1425 ing, (2) calibration, (3) coaddition, and (4) difference
 1426 image analysis (DIA).

⁹⁸ For future Data Releases, data processing will be distributed across the USDF, the French (FrDF) and UK (UKDF) data facilities.

1427 4.1. LSST Science Pipelines Software

1428 The LSST Science Pipelines software (Rubin Observa-
 1429 tory Science Pipelines Developers 2025; J. D. Swinbank
 1430 et al. 2020) will be used to generate all Rubin Obser-
 1431 vatory and LSST data products. They provide both
 1432 the algorithm and middleware frameworks necessary to
 1433 process raw data into science-ready data products, en-
 1434 abling analysis by the Rubin scientific community. Ver-
 1435 sion v29.1 of the pipelines was used to produce DP1⁹⁹.

1436 4.2. Single Frame Processing

1437 4.2.1. Instrument Signature Removal

1438 The first step in processing LSSTComCam images is
 1439 to correct for the effects introduced by the telescope and
 1440 detector. Each sensor and its readout amplifiers can
 1441 vary slightly in performance, causing images of even a
 1442 uniformly illuminated focal plane to exhibit discontinu-
 1443 ities and shifts due to detector effects. The ISR pipe-
 1444 line aims to recover the original astrophysical signal as
 1445 best as possible and produce science-ready single-epoch
 1446 images for source detection and measurement. A detailed
 1447 description of the ISR procedures can be found in P. Fa-
 1448 greglius & E. S. Rykoff (2025) and A. A. Plazas Malagón
 1449 et al. (2025). Figure 11 illustrates the model of detector
 1450 components and readout electronics and their impact
 1451 on the signal, tracing the process from photons incident
 1452 on the detector surface to the final quantized values¹⁰⁰
 1453 recorded in the image files. The ISR pipeline essen-

⁹⁹ Documentation for this version is available at https://pipelines.lsst.io/v/v29_1_1

¹⁰⁰ The images written to disk by the camera have values that are integers that come from the ADC converting an analog voltage.

1454 tially “works backward” through the signal chain, cor-
 1455 recting the integer analog-to-digital units (ADU) raw
 1456 camera output back to a floating-point number of pho-
 1457 toelectrons created in the silicon. The physical detec-
 1458 tor, represented on the left in Figure 11, is the source
 1459 of effects that arise from the silicon itself, such as the
 1460 dark current and the brighter-fatter effect (A. A. Plazas
 1461 et al. 2018; A. Broughton et al. 2024). After the inte-
 1462 gration time has elapsed, the charge is shifted to the
 1463 serial register and read out, which can introduce charge
 1464 transfer inefficiencies and a clock-injected offset level.
 1465 The signals for all amplifiers are transferred via cables
 1466 to the Readout Electronics Board (REB), during which
 1467 crosstalk between the amplifiers may occur. The Ana-
 1468 log Signal Processing Integrated Circuit (ASPIC) on the
 1469 REB converts the analog signal from the detector into a
 1470 digital signal, adding both quantization and a bias level
 1471 to the image. Although the signal chain is designed to
 1472 be stable and linear, the presence of numerous sources
 1473 of non-linearity indicates otherwise.

1474 The ISR processing pipeline for DP1 performs, in
 1475 the following order: Analogue-to-Digital Unit (ADU)
 1476 dithering to reduce quantization effects, serial over-
 1477 scan subtraction, saturation masking, gain normaliza-
 1478 tion, crosstalk correction, parallel overscan subtraction,
 1479 linearity correction, serial CTI correction, image assem-
 1480 bly, bias subtraction, dark subtraction, brighter-fatter
 1481 correction, defect masking and interpolation, variance
 1482 plane construction, flat fielding, and amplifier offset
 1483 (amp-offset) correction¹⁰¹. Flat fielding for DP1 was
 1484 performed using combined flats produced from twilight
 1485 flats acquired with sufficient rotational dithering to mit-
 1486 igate artifacts from print-through stars, as described in
 1487 §2.3.

¹⁰¹ Amp-offset corrections are designed to address systematic dis-
 continuities in background sky levels across amplifier bound-
 aries. The implementation in the LSST Science Pipelines is
 based on the Pan-STARRS Pattern Continuity algorithm (C. Z.
 Waters et al. 2020).

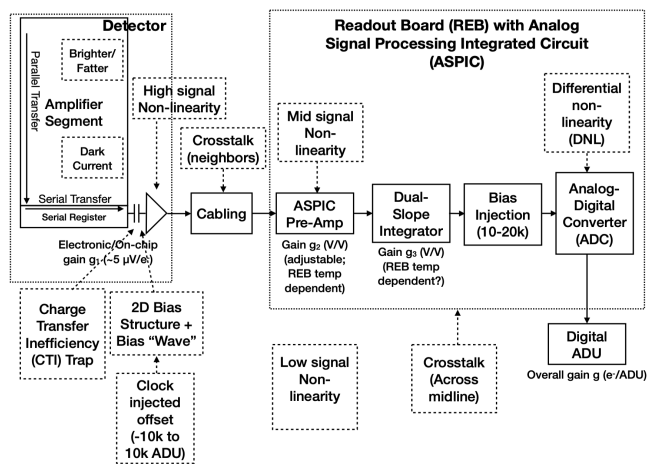


Figure 11. The model of the detector and REB components, labeled with the effects that they impart on signal.

4.2.2. Background Subtraction

The background subtraction algorithms in the LSST Science Pipelines estimate and remove large-scale background signals from science imaging. Such signals may include sky brightness from airglow, moonlight, scattered light instrumental effects, zodiacal light, and diffuse astrophysical emission. In so doing, true astrophysical sources are isolated to allow for accurate detection and measurement.

To generate a background model, each post-ISR image is divided into superpixels of 128×128 pixels. Pixels with a mask flag set that indicates that they contain no useful science data or that they contain flux from a preliminary source detection are masked. The iterative 3σ clipped mean of the remaining pixels is calculated for each superpixel, constructing a background statistics image. A sixth-order Chebyshev polynomial is fit to these values on the scale of a single detector to allow for an extrapolation back to the native pixel resolution of the post-ISR image.

4.3. Calibration

Stars are detected in each post-ISR image using a 5σ threshold. Detections of the same star across multiple images are then associated to identify a consistent set of isolated stars with repeated observations suitable for use in PSF modeling, photometric calibration, and astrometric calibration.

Initial astrometric and photometric solutions are derived using only the calibration reference catalogs (see §3.2), and an initial PSF model is fit using PSFEx (E. Bertin 2011). These preliminary solutions provide approximate source positions, fluxes, and PSF shapes that serve as essential inputs to the calibration process, en-

1521 abling reliable source matching, selection of high-quality
 1522 stars, and iterative refinement of the final astrometric,
 1523 photometric, and PSF models. These preliminary solu-
 1524 tions are subsequently replaced by more accurate fits, as
 1525 described in the following sections.

1526 4.3.1. PSF Modeling

1527 PSF modeling in DP1 uses the Piff (M. Jarvis et al.
 1528 2021) package. Our configuration of Piff utilizes its `Pix-`
 1529 `elGrid` model with a fourth-order polynomial interpola-
 1530 tion per CCD, except in the u -band, where star counts
 1531 are insufficient to support a fourth-order fit. In this
 1532 case, a second-order polynomial is used instead. Details
 1533 on the choice of polynomial order, overall PSF modeling
 1534 performance, and known issues are discussed in §5.2.

1535 4.3.2. Astrometric Calibration

1536 Starting from the astrometric solution calculated in
 1537 single frame processing (§4.2), the final astrometric so-
 1538 lution is computed using the ensemble of visits in a given
 1539 band that overlap a given tract. This allows the astro-
 1540 metric solution to be further refined by using all of the
 1541 isolated point sources of sufficient signal-to-noise ratio
 1542 in an image, rather than only those that appear in the
 1543 reference catalog, as is done in single frame processing.
 1544 Using multiple whole visits rather than a single detector
 1545 also allows us to account for effects that impact the full
 1546 focal plane, and for the proper motion and parallax of
 1547 the sources.

1548 In order to perform the fit of the astrometric solu-
 1549 tion, isolated point sources are associated between over-
 1550 lapping visits and with the Gaia DR3 (Gaia Collabora-
 1551 tion et al. 2023b) reference catalog where possible. The
 1552 model used for DP1 consists of a static map from pixel
 1553 space to an intermediate frame (the per-detector model),
 1554 followed by a per-visit map from the intermediate frame
 1555 to the plane tangent to the telescope boresight (the per-
 1556 visit model), then finally a deterministic mapping from
 1557 the tangent plane to the sky. The fit is done using the
 1558 `gbdes` package (G. M. Bernstein et al. 2017), and a full
 1559 description is given in C. Saunders (2024).

1560 The per-detector model is intended to capture quasi-
 1561 static characteristics of the telescope and camera. Dur-
 1562 ing Rubin Operations, the astrometric solution will al-
 1563 low for separate epochs with different per-detector mod-
 1564 els, to account for changes in the camera due to warm-
 1565 ing and cooling and other discrete events. However, for
 1566 DP1, LSSTComCam was assumed to be stable enough
 1567 that all visits use the same per-detector model. The
 1568 model itself is a separate two-dimensional polynomial for
 1569 each detector. For DP1, a degree 4 polynomial was used;
 1570 the degree of the polynomial mapping is tuned for each

1571 instrument and may be different for LSSTCam. Fur-
 1572 ther improvements may be made by including a pixel-
 1573 based astrometric offset mapping, which would be fit
 1574 from the ensemble of astrometric residuals, but this is
 1575 not included in the DP1 processing.

1576 The per-visit model attempts to account for the path
 1577 of a photon from both atmospheric sources and those
 1578 dependent on the telescope orientation. This model is
 1579 also a polynomial mapping, in this case a degree 6 two-
 1580 dimensional polynomial. Correction for DCR (§5.4) was
 1581 not done for DP1, but will be included in LSSTCam
 1582 processing during Rubin Operations. Future processing will
 1583 also likely include a Gaussian Process fit to better ac-
 1584 count for atmospheric turbulence, as was demonstrated
 1585 by W. F. Fortino et al. (2021) and P. F. Léget et al.
 1586 (2021).

1587 The final component of the astrometric calibration
 1588 involves the positions of the isolated point sources in-
 1589 cluded in the fit, which are described by five parameters:
 1590 sky coordinates, proper motion, and parallax. While
 1591 proper motions and parallaxes are not released for DP1,
 1592 they are fitted for these sources in the astrometric solu-
 1593 tion to improve the astrometric calibration.

1594 4.3.3. Photometric Calibration

1595 Photometric calibration of the DP1 dataset is based
 1596 on the Forward Global Calibration Method (FGCM)
 1597 (D. L. Burke et al. 2018), adapted for the LSST Sci-
 1598 ence Pipelines (H. Aihara et al. 2022; P. Fagelius &
 1599 E. S. Rykoff 2025). We used the FGCM to calibrate
 1600 the full DP1 dataset with a forward model that uses a
 1601 parameterized model of the atmosphere as a function of
 1602 airmass along with a model of the instrument through-
 1603 put as a function of wavelength. The FGCM process
 1604 typically begins with measurements of the instrumental
 1605 throughput, including the mirrors, filters, and detectors.
 1606 However, because full scans of the LSSTComCam as-
 1607 built filters and individual detectors were not available,
 1608 we instead used the nominal reference throughputs for
 1609 the Simonyi Survey Telescope and LSSTCam.¹⁰² These
 1610 nominal throughputs were sufficient for the DP1 cali-
 1611 bration, given the small and homogeneous focal plane
 1612 consisting of only nine ITL detectors. The FGCM atmo-
 1613 sphere model, provided by MODTRAN (A. Berk et al.
 1614 1999), was used to generate a look-up table for atmo-
 1615 spheric throughput as a function of zenith distance at
 1616 Cerro Pachón. This model accounts for absorption and
 1617 scattering by molecular constituents of the atmosphere,
 1618 including O_2 and O_3 ; absorption by water vapor; and
 1619 Mie scattering by airborne aerosol particulates. Nightly

¹⁰² Available at: <https://github.com/lstt/throughputs/tree/1.9>

variations in the atmosphere are modeled by minimizing the variance in repeated observations of stars with a Signal to Noise Ratio (SNR) greater than 10, measured using “compensated aperture fluxes”. These fluxes include a local background subtraction (see §4.2.2) to mitigate the impact of background offsets. The model fitting process incorporates all six bands (*ugrizy*) but does not include any gray (achromatic) terms, except for a linear assumption of mirror reflectance degradation, which is minimal over the short duration of the DP1 observation campaign. As an additional constraint on the fit, we use a subset of stars from the reference catalog (P. S. Ferguson et al. 2025), primarily to constrain the system’s overall throughput and establish the “absolute” calibration.

Photometric transformation relations between LSST-Cam and LSSTComCam systems and other photometric systems are under development and are provided in (M. N. Porter et al. 2026)

4.4. Visit Images and Source Catalogs

With the final PSF models, WCS solutions, and photometric calibrations in place, we reprocess each single-epoch image to produce a final set of calibrated visit images and source catalogs. Source detection is performed down to a 5σ threshold using the updated PSF models, followed by measurement of PSF and aperture fluxes. These catalogs represent the best single-epoch source characterization, but they are not intended for constructing light curves. For time-domain analysis, we recommend using the forced photometry tables described in §4.6.2.

4.5. Coaddition Processing

4.5.1. Coaddition

Only exposures with a seeing better than 1.7 arcseconds FWHM are included in the deep coadded images. For the template coadds, typically only the top third of visits with the best seeing are used (although see §3.1 for more details), resulting in an even tighter image quality cutoff for the template coadds. Exposures with poor PSF model quality, identified using internal diagnostics, are excluded to prevent contamination of the coadds with unreliable PSF estimates. The remaining exposures are combined using an inverse-variance weighted mean stacking algorithm.

To mitigate transient artifacts before coaddition, we apply the artifact rejection procedure described in Y. Al-Sayyad (2018) that identifies and masks features such as satellite trails, optical ghosts, and cosmic rays. It operates on a time series of PSF-matched images resampled onto a common pixel grid (“warps”) and leverages their

temporal behavior to distinguish persistent astrophysical sources from transient artifacts.

Artifact rejection uses both direct (where no PSF-matching is performed) and PSF-matched warps, homogenized to a standard PSF of 1.8 arcseconds FWHM, broadly consistent with the 1.7 arcsecond FWHM seeing threshold used in data screening. A sigma-clipped mean of the PSF-matched warps serves as a static sky model, against which individual warps are differenced to identify significant positive and negative residuals. Candidate artifact regions are classified as transient if they appear in less than a small percentage of the total number of exposures, with the threshold based on the number of visits, N , as follows:

- $N = 1$ or 2 : threshold = 0 (no clipping).
- $N = 3$ or 4 : threshold = 1.
- $N = 5$: threshold = 2.
- $N > 5$: threshold = $2 + 0.03N$.

Identified transient regions are masked before coaddition, improving image quality and reducing contamination in derived catalogs.

4.5.2. Detection, Deblending and Measurement

After constructing coadded images, sources are detected in each band, merged across bands, deblended, and measured to generate the final object catalogs (§3.2). For each coadd in all six bands, we perform source detection at a 5σ detection threshold and then adjust the background with a per-patch constant (coadds are built from background-subtracted images, but the deeper detection on coadds redefines what is considered source versus background). Detections across bands are merged in a fixed priority order, *irzygu*, to form a union detection catalog, which serves as input to deblending.

Deblending is performed using the Scarlet Lite algorithm, which implements the same model as Scarlet (P. Melchior et al. 2018), but operates on a single pixel grid. This allows the use of analytic gradients, resulting in greater computational speed and memory efficiency.

Object measurement is then performed on the deblended detection footprints in each band. Measurements are conducted in three modes: independent per-band measurements, forced measurements in each band, and multiband measurements.

Most measurement algorithms operate through a single-band plugin system, largely as originally described in J. Bosch et al. (2018). The same plugins are run separately for each object on a deblended image,

1718 which uses the Scarlet model as a template to re-weight
 1719 the original noisy coadded pixel values. This effectively
 1720 preserves the original image in regions where objects are
 1721 not blended, while dampening the noise elsewhere.

1722 A reference band is chosen for each object based on de-
 1723 tection significance and measurement quality using the
 1724 same priority order as detection merging (*irzygu*) and
 1725 a second round of measurements is performed in forced
 1726 mode using the shape and position from the reference
 1727 band to ensure consistent colors (J. Bosch et al. 2018).

1728 Measurement algorithm outputs include object fluxes,
 1729 centroids, and higher-order moments thereof like sizes
 1730 and shapes. A variety of flux measurements are pro-
 1731 vided, from aperture fluxes and forward modeling algo-
 1732 rithms.

1733 Composite model (CModel) magnitudes (K. Abaza-
 1734 jian et al. 2004; J. Bosch et al. 2018) are used to cal-
 1735 culate the extendedness parameter, which functions as
 1736 a star-galaxy classifier. Extendedness is a binary clas-
 1737 sifier that is set to 1 if the PSF model flux is less than
 1738 98.5% of the (free, not forced) CModel flux in a given
 1739 band. Additionally, the extendedness in the reference
 1740 band is provided as a separate column for convenience
 1741 as a multiband star-galaxy classification, and is recom-
 1742 mended generally but also specifically for objects with
 1743 low signal-to-noise ratio in some bands.

1744 Gaussian-Aperture-and-PSF (Gaussian Aperture and
 1745 PSF (GAaP) K. Kuijken 2008; A. Kannawadi 2025)
 1746 fluxes are provided to ensure consistent galaxy colors
 1747 across bands. Sérsic model (J. L. Sérsic 1963; J. L. Sérsic
 1748 1968) fits are run on all available bands simultaneously
 1749 (MultiProFit, D. S. Taranu 2025). The resulting Sérsic
 1750 model fluxes are provided as an alternative to CModel
 1751 and are intended to represent total galaxy fluxes. Like
 1752 CModel, the Sérsic model is a Gaussian mixture approx-
 1753 imation to a true Sérsic profile, convolved with a Gaus-
 1754 sian mixture approximation to the PSF. Sérsic model
 1755 fits also include a free centroid, with all other structural
 1756 parameters shared across all bands. That is, the in-
 1757 trinsic model has no color gradients, but the convolved
 1758 model may have color gradients if the PSF parameters
 1759 vary significantly between bands.

1760 CModel measurements use a double “shapelet” (A.
 1761 Refregier 2003) PSF model with a single shared shape.
 1762 The Sérsic fits are intended to use a double Gaussian
 1763 with independent shape parameters for each component.
 1764 Due to a pipeline misconfiguration, the Sérsic fits actu-
 1765 ally used the shapelet PSF parameters, with the higher-
 1766 order terms ignored (since MultiProFit does not sup-
 1767 port shapelet PSFs). This bug is not expected to im-
 1768 pact the galaxy fluxes significantly, since the higher-
 1769 order shapelet PSF parameters tend to be small, and

1770 the fix will be applied in future campaigns. Either way,
 1771 the double Gaussian PSF parameters are included for
 1772 each object.

1773 Further details on the performance of these algorithms
 1774 are found in §5.7.

1775 4.6. Variability Measurement

1776 4.6.1. Difference Imaging Analysis

1777 Difference Image Analysis (DIA) uses the decorrelated
 1778 Alard & Lupton image differencing algorithm (D. J.
 1779 Reiss & R. H. Lupton 2016). We detected both posi-
 1780 tive and negative DIASources at 5σ in the difference
 1781 image. Sources with footprints containing both posi-
 1782 tive and negative peaks due to offsets from the tem-
 1783 plate position or blending were fit with a dipole centroid
 1784 code, which simultaneously fits offset positive and neg-
 1785 ative PSFs. We filter the resulting DIASource catalog
 1786 to remove detections with pixel flags indicative of ar-
 1787 tifacts, non-astrophysical trail lengths, or unphysically
 1788 negative direct fluxes. Finally, we perform a simple spa-
 1789 tial association of DIASources into DIAObjects using a
 1790 one-arcsecond matching radius.

1791 The Machine Learning reliability model applied to
 1792 DP1 was developed with the aim to meet the latency
 1793 requirements for Rubin Alert Production when executed
 1794 on CPUs. Accordingly we developed a relatively simple
 1795 model: a Convolutional Neural Network with three con-
 1796 volutional layers, and two fully connected layers. The
 1797 convolutional layers have a 5×5 kernel size, with 16, 32,
 1798 and 64 filters, respectively. A max-pooling layer of size 2
 1799 is applied at the end of each convolutional layer, followed
 1800 by a dropout layer of 0.4 to reduce overfitting. The last
 1801 fully connected layers have sizes of 32 and 1. The ReLU
 1802 activation function is used for the convolutional layers
 1803 and the first fully connected layer, while a sigmoid func-
 1804 tion is used for the output layer to provide a probabilistic
 1805 interpretation. The cutouts are generated by extracting
 1806 postage stamps of 51×51 pixels centered on the detected
 1807 sources. The input data of the model consist of the tem-
 1808 plate, science, and difference image stacked to have an
 1809 array of shape (3, 51, 51). The model is implemented
 1810 using PyTorch (J. Ansel et al. 2024). The Binary Cross
 1811 Entropy loss function was used, along with the Adap-
 1812 tive Moment Estimation (Adam) optimizer with a fixed
 1813 learning rate of 1×10^{-4} , weight decay of 3.6×10^{-2} , and
 1814 a batch size of 128. The final model uses the weights
 1815 that achieved the best precision/purity for the test set.
 1816 Training was done on the SLAC Shared Scientific Data
 1817 Facility (S3DF) with an NVIDIA model L40S GPU.

1818 The model was initially trained using simulated data
 1819 from the second DESC Data Challenge (DC2; (LSST
 1820 Dark Energy Science Collaboration (LSST DESC) et al.

2021)) plus randomly located injections of PSFs to increase the number of real sources, for a total of 89,066 real sources. The same number of bogus sources were selected at random from non-injected DIASources. Once the LSSTComCam data were available, the model was fine-tuned on a subset of the data containing 183,046 sources with PSF injections. On the LSSTComCam test set, the model achieved an accuracy of 98.06%, purity of 97.87%, and completeness of 98.27%. As discussed in §5.8, the injections used to train this model version do not capture all types of astrophysical variability, so performance on the test set will not be representative for variable stars, comets, and other types of variable objects. The machine-learning reliability score, reported in the `reliability` column of the `DIASource` catalog, is a scalar value between 0 and 1 that quantifies the model’s confidence that a given detection is astrophysical.

4.6.2. Light Curves

To produce light curves, we perform multi-epoch forced photometry on both the direct visit images and the difference images. For light curves we recommend the forced photometry on the difference images (`psfDiffFlux` on the `ForcedSource` Table), as it isolates the variable component of the flux and avoids contamination from static sources. In contrast, forced photometry on direct images includes flux from nearby or blended static objects, and this contamination can vary with seeing. Centroids used in the multi-epoch forced photometry stage are taken either from object positions measured on the coadds or from the `DIAObjects` (the associated `DIASources` detected on difference images).

4.6.3. Solar System Processing

Solar system processing in DP1 consists of two key components: the association of observations (sources) with known solar system objects, and the discovery of previously unknown objects by linking sets of tracklets¹⁰³.

The association component begins by generating expected positions for all objects in the Minor Planet Center orbit catalog, using ephemerides computed with the `Sorcha` survey simulation toolkit (Merritt et al., in press)¹⁰⁴. To enable fast lookup of objects potentially present in an observed visit, we use the `mpsky` package (M. Juric 2025). In each image, the closest `DIASource` within 1 arcsecond of a known solar system object’s predicted position is associated to that object.

In DP1 we used a simple positional association to tag `DiaSources` that are likely observations of known asteroids. The 1 arcsecond radius is intentionally generous; we did not see evidence of mismatches at DP1 depth and volume. This radius will be tuned for future processing campaigns.

The discovery component of Solar System processing uses the `heliolinx` package¹⁰⁵, which provides tools for asteroid identification and linking (A. Heinze et al. 2023). The repository contains code for the following tasks:

- Tracklet creation with `make_tracklets`
- Multi-night tracklet linking with an algorithm
- Linkage post processing (orbit fitting, outlier rejection, and de-duplication) with `link_purify`

The inputs to the discovery processing comprised all sources detected in difference images, regardless of whether they were tagged in the association step. These inputs were produced by an early processing of LSST-ComCam commissioning data, some of which were later rejected during DP1 processing and therefore do not appear in the final DP1 data products.

About 10% of all commissioning visits targeted the near-ecliptic field `Rubin_SV_38_7`, chosen to facilitate asteroid discovery. `Rubin_SV_38_7` produced the vast majority of asteroid discoveries in DP1, as expected, but a few were found in off-ecliptic fields as well.

Tracklet creation with `make_tracklets` used an upper limit angular velocity of 1.5 deg/day, faster than any main belt asteroid and in the range of many Near-Earth Object (NEO) discoveries. While no formal minimum angular velocity was imposed, in practice it would be unlikely to detect objects moving slower than about 0.01 deg day⁻¹. To minimize false tracklets from fields observed multiple times per night, the minimum tracklet length was set to three detections, and a minimum on-sky motion of five arcseconds was required for a valid tracklet. To claim a discovery candidate, we required tracklets to be linked across at least three nights.

Multi-night tracklet linking is the heart of Solar system discovery, which connects (“links”) tracklets belonging to the same object over a series of nights. It employs the `HelioLinC3D` algorithm (S. Eggl et al. 2020; A. Heinze et al. 2022), a refinement of the original `HelioLinC` algorithm of M. J. Holman et al. (2018). Each processing run tested each tracklet with 324 different hypotheses spanning heliocentric distances from 1.5 to

¹⁰³ A tracklet is defined as two or more detections of a moving object candidate taken in close succession in a single night.

¹⁰⁴ Available at <https://github.com/dirac-institute/sorcha>

¹⁰⁵ <https://github.com/heliolinx/heliolinx>

1914 9.8 astronomical unit (au) and radial velocities span-
 1915 ning the full range of possible bound orbits (eccentricity
 1916 0.0 to nearly 1.0). The upper limit of 10 au was cho-
 1917 sen because searches targeting more distant populations
 1918 require different parameter choices. This range of dis-
 1919 tance encompasses all main belt asteroids and Jupiter
 1920 Trojans, as well as many comets and Mars-crossers and
 1921 some NEOs. A dedicated search for objects at heliocen-
 1922 tric distances out to 50 au was also conducted; no distant
 1923 objects were detected, consistent with expectations for
 1924 the size of the DP1 data set. Smaller heliocentric dis-
 1925 tances were not attempted here because nearby objects
 1926 move rapidly across the sky and hence were not likely
 1927 to remain long enough in an LSSTComCam field to be
 1928 discovered.

1929 Candidate linkages, defined as groups of tracklets
 1930 whose propagated orbits cluster within a radius of 1.33
 1931 $\times 10^3$ au at 1 au, are identified, then post-processed via
 1932 `link_purify` to yield a final, non-overlapping set of
 1933 high-confidence asteroid candidates, ranked by orbit-
 1934 fit residuals and related metrics. While `heliolinx` can
 1935 produce false-positive or redundant raw linkages by de-
 1936 sign, these are filtered during post-processing by `link_`
 1937 `purify`, which applies a Rubin-specific, more stringent
 1938 version of the MPC validation rules¹⁰⁶. This step both
 1939 rejects spurious linkages and deduplicates multiple hy-
 1940 potheses for the same object, ensuring that only the
 1941 highest-quality, non-redundant linkages are carried for-
 1942 ward for orbit determination and for distinguishing new
 1943 discoveries from rediscoveries of known objects.

1944 5. PERFORMANCE CHARACTERIZATION AND 1945 KNOWN ISSUES

1946 In this section, we provide an assessment of the DP1
 1947 data quality and describe known issues.

1948 5.1. Sensor Anomalies and ISR

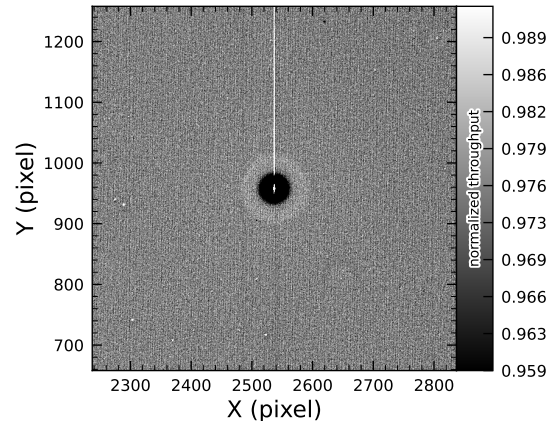
1949 In addition to the known detector features identified
 1950 before LSSTComCam commissioning, most of which are
 1951 handled by the ISR processing (see §4.2.1), we discov-
 1952 ered a number of new types of anomalies in the DP1
 1953 data. Since no corrections are currently available for
 1954 these anomalies, they are masked and excluded from
 1955 downstream data products.

1956 5.1.1. Vampire Pixels

1957 “Vampire” pixels are visible on the images as a bright
 1958 defect surrounded by a region of depressed flux, as
 1959 though the defect is stealing charge from its neighboring

1960 pixels. Figure 12 shows an example of a vampire pixel
 1961 near the center of R22_S11 on an *r*-band flat.

1962 From studies on evenly illuminated images, vampires
 1963 appear to conserve charge. Unfortunately, no unique
 1964 optimum way exists to redistribute this stolen flux so,
 1965 following visual inspection, a defect mask was created
 1966 to exclude them from processing. We have found some
 1967 similar features on the ITL detectors on LSSTCam, and
 1968 will use the same approach to exclude them.



1969 **Figure 12.** A large vampire pixel near the center of R22_-
 1970 S11, as seen on the *r*-band flat. This clearly shows the central hot “vampire” pixels, surrounded by a region of depressed signal, with a brighter ring surrounding that caused by the local electric field effects. The charge contained in the central pixels is incompletely shifted as the image is read, and that charge leaks out into subsequent rows as they are shifted through the remnant charge. The columns that contain the hot pixels are masked as defects in all processing, as this feature cannot be otherwise corrected.

1971 5.1.2. Phosphorescence

1972 Some regions of the LSSTComCam CCD raft were
 1973 seen to contain large numbers of bright defects. An ex-
 1974 ample is shown in Figure 13 in a *g*-band flat. On further
 1975 investigation, it appears that on some detectors a layer
 1976 of photoresist wax was incompletely removed from the
 1977 detector surface during production. As this wax is now
 1978 trapped below the surface coatings, there is no way to
 1979 physically clean these surfaces. If this wax responded
 1980 to all wavelengths equally, then it would likely result in
 1981 quantum efficiency dips, which might be removable dur-
 1982 ing flat correction. However, it appears that this wax is
 1983 slightly phosphorescent, with a decay time on the order
 1984 of minutes, resulting in the brightness of these defects
 1985 being dependent on the illumination of prior exposures.
 1986 The worst of these regions were excluded with manual
 1988 masks.

¹⁰⁶ <https://minorplanetcenter.net/mpcops/documentation/identifications/additional/>

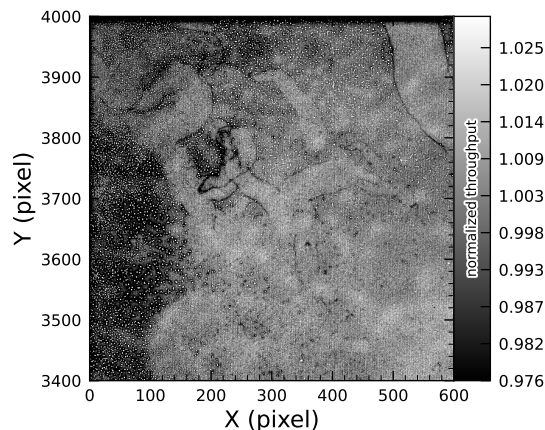


Figure 13. The top left corner of R22_S01 in the g-band flat, showing the many small defect features that are caused by the remnant photoresist wax. A single large defect box masks this region from further analysis to prevent these features from contaminating measurements.

5.1.3. Crosstalk

Crosstalk refers to unwanted signal interference between adjacent pixels or amplifiers. We use an average inter-amp crosstalk correction based on laboratory measurements with LSSTCam. These average corrections proved satisfactory, and so have been used as-is for DP1 processing. There are, however, some residual crosstalk features present post-correction, with a tendency towards over-subtraction. Figure 14 shows an example of a bright star with over-subtracted crosstalk residuals visible on neighboring amplifiers to both sides on exposure 2024120600239, detector R22_S02.

5.1.4. Bleed Trails

Bleed trails are produced when charge from saturated pixels spills into adjacent pixels. Bleed trails were anticipated on LSSTComCam sensors, but they appear in more dramatic forms than had been expected. As a bleed trail nears the serial register, it fans out into a “trumpet” shaped feature. Although bright, these features do not have consistently saturated pixels. In DP1 these “edge bleeds” were identified and masked.

Saturated sources can create a second type of bleed, where the central bleed drops below the background level. The depressed columns along these trails extend across the entire readout column of the detector, crossing the detector mid-line. We developed a model for these to identify which sources are sufficiently saturated to result in such a trail, which is then masked. As this kind of trail appears only on the ITL detectors, we’ve named these features “ITL dips”. Figure 15 shows an example of a bright star exhibiting the “ITL dip” phe-

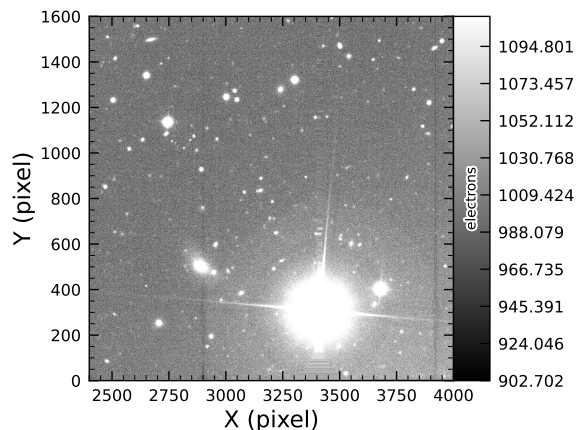


Figure 14. An example of a bright star with over-subtracted crosstalk residuals visible on neighboring amplifiers to both sides (exposure 2024120600239, detector R22_S02). The horizontal banding stretching from the center of the star shows the interpolation pattern covering the saturated core and the ITL edge bleed near the serial register.

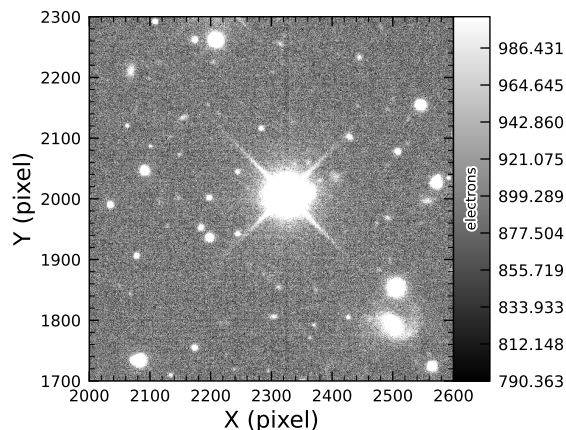


Figure 15. A bright star showing the “ITL dip” phenomenon, in which a dark trail extends out from the star to the top and bottom edges of the detector (exposure: 2024121000503, detector: R22_S21).

5.2. PSF Models

To characterize PSF performance, we use adaptive second moments (G. M. Bernstein & M. Jarvis 2002) measured on PSF stars and on the PSF model using the HSM implementation (C. Hirata & U. Seljak 2003; R. Mandelbaum et al. 2005). All measurements are expressed in the pixel coordinate frame of each detector. We characterize the performance of the PSF using the

classical trace of the second moment matrix T , along with the ellipticity parameters e^1 and e^2 . Measurements on the observed PSF stars are denoted as T_{PSF} , e_{PSF}^1 , e_{PSF}^2 , while those from PSF models are denoted as T_{model} , e_{model}^1 , e_{model}^2 . We compare two PSF modeling approaches:

- Piff with second-order polynomial interpolation (Piff O2), the pipeline’s default, and
- Piff with fourth-order polynomial interpolation (Piff O4), which serves as the final DP1 PSF model.

Table 5 summarizes each model’s ability to reconstruct the mean T , e^1 , and e^2 on LSSTComCam. Both models exhibit a negative residual bias in the reconstructed PSF size, with Piff O4 providing improved performance over Piff O2.

An alternative approach to evaluating the performance of the PSF model is to examine the average $\delta T/T$, where δT is $T_{\text{PSF}} - T_{\text{model}}$, across visits, projected onto focal-plane coordinates, as shown in Figure 16. Piff reveals strong spatial correlations in the residuals, including a systematic offset consistent with the results presented in Table 5. The presence of these spatial structures motivated the adoption of fourth-order polynomial interpolation in all bands except u -band. Although not shown in Figure 16, residual patterns persist even with third-order interpolation, indicating that it is insufficient to capture the complexity of the PSF variation. Increasing the interpolation order to five would nominally reduce the residuals further, but the limited number of stars available on some CCDs would not provide adequate constraints for such a model, while the resulting improvement would likely be minimal. Preliminary analysis of LSSTCam data in the laboratory at SLAC National Accelerator Laboratory (SLAC) shows that the ITL sensors exhibit the same pattern as ITL sensors on LSSTComCam.

Another way to look at the PSF modeling quality is via whisker plots of the PSF second and fourth moments and their modeling residuals projected on a part of the sky. In addition to the second moment, the spin-2 fourth moments, $e^{(4)}$, are defined as:

$$e_1^{(4)} = M_{40} - M_{04}$$

$$e_2^{(4)} = 2(M_{31} - M_{13}),$$

where M_{pq} are the standardized higher moments as defined in T. Zhang et al. (2023) measured on stars and PSF models. Figure 17 shows the whisker plots of e , $e^{(4)}$ (top rows), and δe , $\delta e^{(4)}$ in the ECDFS field. The direction of a whisker represents the orientation of the

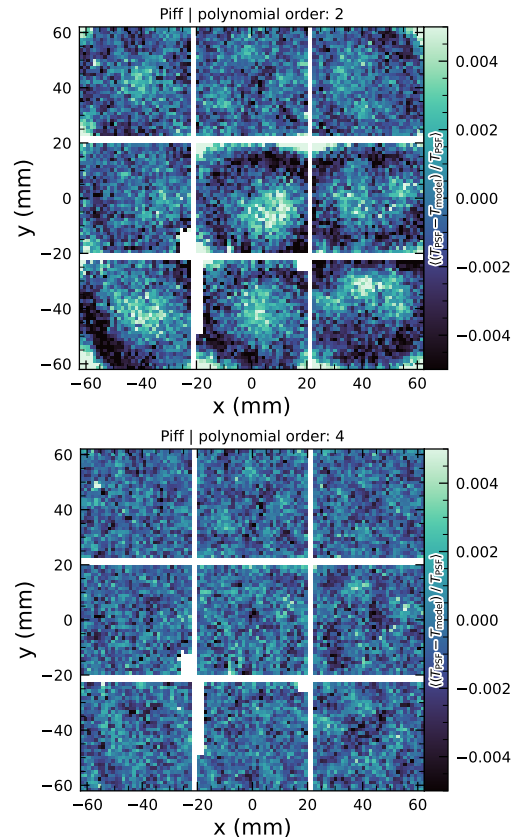


Figure 16. Average across all visits of $\delta T/T$ for Piff O2 and Piff O4 modeling on LSSTComCam. Averages are computed using a 120×120 binning.

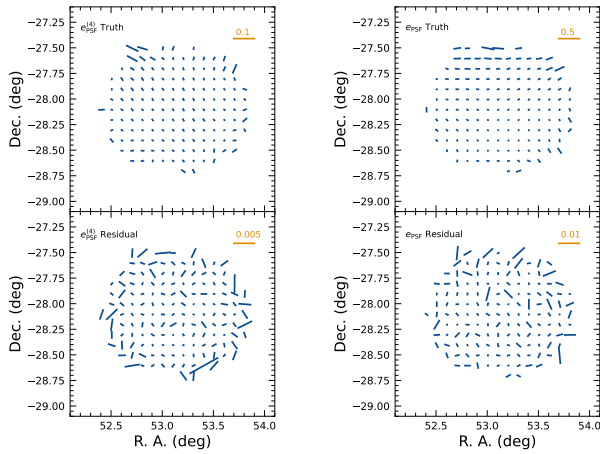
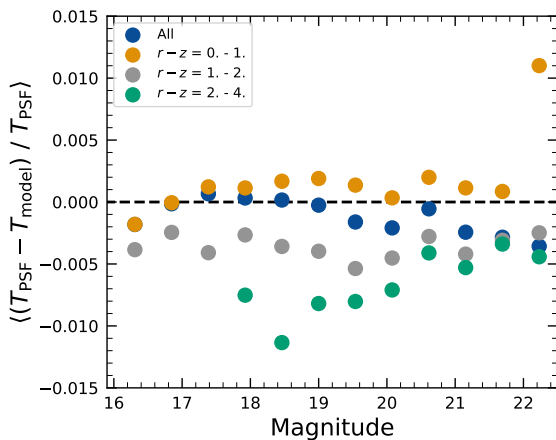
shape, while the length represents the amplitude $|e|$ or $|e^{(4)}|$. We observe coherent patterns in both the PSF moments and the residuals, the latter of which warrants further investigation if it persists in future data releases.

Figure 18 shows a plot of $\delta T/T$ versus stellar magnitude, which can reveal any dependencies between PSF size and flux. We also repeat this analysis in color bins to probe chromatic effects. Binning by color uncovers a clear color dependence, as was also seen in DES (M. Jarvis et al. 2021). The residual is consistent with Table 5 and its cause is unknown. DP1 does not include the color correction implemented in the DES Year 6 analysis, T. Schutt et al. (2025). This will be included in processing of future data releases.

As noted in Rubin Observatory Science Pipelines Developers (2025), two key Piff features were not used in the DP1 processing. PSF color dependence was not implemented, and, while Rubin software allows Piff to work with sky coordinates (including WCS transformations), it does not yet correct for sensor-induced astrometric

Table 5. Observed mean values and comparison of model residuals, across all visits and filters

Quantity	Observed	Piff O2	Piff O4
		$\times 10^{-4}$	$\times 10^{-4}$
$\langle T \rangle$ (pixel ²)	11.366 ± 0.003		
$\langle e^1 \rangle$	$(-6.07 \pm 0.05) \times 10^{-3}$		
$\langle e^2 \rangle$	$(-4.57 \pm 0.05) \times 10^{-3}$		
$\langle e \rangle$	$(8.794 \pm 0.004) \times 10^{-2}$		
$\langle \delta T/T \rangle$		-4.0 ± 0.2	-5.0 ± 0.2
$\langle \delta e^1 \rangle$		0.6 ± 0.1	0.5 ± 0.1
$\langle \delta e^2 \rangle$		0.0 ± 0.1	0.0 ± 0.1

**Figure 17.** Whisker plots for the ECDFS field for e , $e^{(4)}$ and δe , $\delta e^{(4)}$.**Figure 18.** Binned $\delta T/T$ as a function of magnitude across all visits and filters and in bins of stellar colors.

2106 distortions such as tree rings (H. Y. Park et al. 2017).
 2107 Both features are planned for upcoming releases.

5.3. Astrometry

2108

2109 To characterize astrometric performance, we evaluate
 2110 both internal consistency and agreement with an external
 2111 reference. The primary measure of internal consistency
 2112 is the repeatability of position measurements for
 2113 the same object, defined as the RMS of the astrometric
 2114 distance distribution for stellar pairs having a specified
 2115 separation in arcminutes. We associate isolated point
 2116 sources across visits and compute the rms of their fitted
 2117 positions, rejecting any stars with another star within
 2118 $2''$. Figure 19 shows the mean per-tract rms astrometric
 2119 error in RA for all isolated point sources, both after the
 2120 initial calibration and after the final calibration, which
 2121 includes proper motion corrections. The results indicate
 2122 that the astrometric solution is already very good after
 2123 the initial calibration. Global calibration yields only
 2124 modest improvement, likely due to the short time span
 2125 of DP1 and the minimal distortions in the LSSTCom-
 2126 Cam. In the main survey, the longer time baseline and
 2127 greater distortions near the LSSTCam field edges will
 2128 make global calibration more impactful. An additional
 2129 measure of internal consistency is the repeatability of
 2130 separations between objects at a given distance. To com-
 2131 pute this, we identify pairs of objects that are separated
 2132 by a specified distance and measure their precise separa-
 2133 tion during each visit in which both objects are ob-
 2134 served. The scatter in these separation measurements
 2135 provides an indication of the internal consistency of the
 2136 astrometric model. Figure 20 shows the median separa-
 2137 tion for pairs of objects separated by approximately 5
 2138 arcminutes (referred to as “AM1”), computed per tract
 2139 after the final calibration. These values are already ap-
 2140 proaching the design requirement of 10 mas.
 2142

2143 To assess external consistency, we consider the median
 2144 separation between sources not included in the astro-
 2145 metric fit and associated objects from a reference catalog
 2146 (§3.3.3). For this, we use the Gaia DR3 catalog, with the

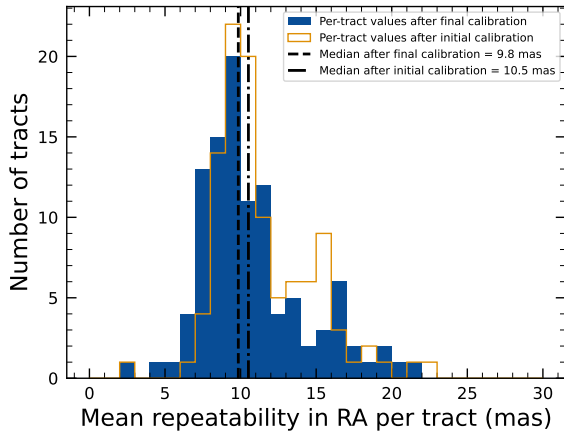


Figure 19. Mean per-tract astrometric repeatability of measurements of isolated point sources in RA in visits across all bands.

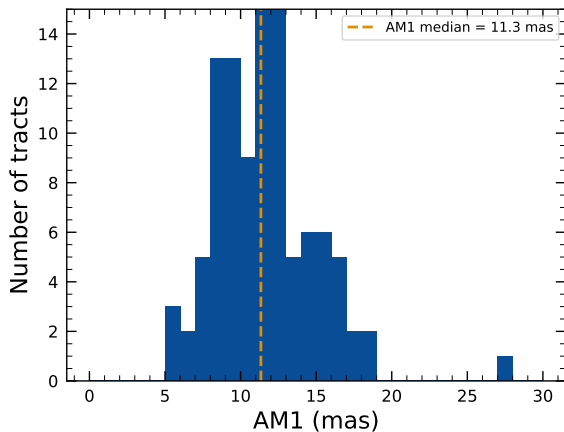


Figure 20. Median per-tract repeatability in separations between isolated point sources 5 arcmin apart (AM1) in visits across all bands.

2147 object positions shifted to the observation epoch using
 2148 the Gaia proper motion parameters. Figure 21 shows the
 2149 median separation for each visit in the r -band in `tract`
 2150 4849 in the ECDFS fields. The calculated values are
 2152 almost all within 5 mas, well below the design require-
 2153 ment of 50 mas for the main survey. By examining the
 2154 astrometric residuals, we can assess whether there are
 2155 distortions not accounted for by the astrometric model.
 2156 In some cases, residuals from a single visit exhibit behav-
 2157 ior consistent with atmospheric turbulence, as shown in
 2158 Figure 22, which is characterized by a curl-free gradient
 2159 field in the two-point correlation function of the residu-
 2160 als (E-mode), P. F. Léget et al. (2021) and W. F. Fortino
 2162 et al. (2021). However, as seen in Figure 23, the residu-
 2163 als in many visits also have correlation functions with

2164 a non-negligible divergence-free B-mode, indicating that
 2165 some of the remaining residuals are due to unmodeled
 2166 instrumental effects, such as rotations between visits.

2168 We can see unmodeled camera distortions by stacking
 2169 the astrometric residuals over many visits as a function
 2170 of the focal plane position. Figure 24 shows the median
 2172 residuals in x and y directions for 1792 visits. Spatial
 2173 structures are evident at the CCD level, as well as at
 2174 the mid-line break, the discontinuity between the two
 2175 rows of amplifiers, in the y -direction residuals. Further
 2176 stacking all the detectors makes certain effects particu-
 2177 larly clear. Figure 25 shows distortions very similar to
 2178 those measured for an LSSTCam ITL sensor in a labo-
 2180 ratory setting in J. H. Esteves et al. (2023).

2181 5.4. Differential Chromatic Refraction

2182 DCR occurs when light passes through Earth’s atmo-
 2183 sphere, refracting more for shorter wavelengths, which
 2184 causes blue light to appear shifted closer to the zenith.
 2185 This wavelength-dependent effect results in the smear-
 2186 ing of point sources along the zenith direction, specifi-
 2187 cally parallel to the parallactic angle. The DCR effect
 2188 is observable in LSSTComCam data, particularly in the
 2189 angular offset versus $g - i$ band magnitude difference
 2190 plots, as shown in Figure 26. These plots include 228
 2191 visits selected to maximize the range of observed air-
 2192 mass, which spans 1.01–1.30 with a mean value of 1.13.
 2193 When looking at data perpendicular to the parallactic
 2194 angle, sources exhibit no discernible DCR effect, which
 2195 is expected, and form a clear vertical distribution on the
 2196 two-dimensional density plots in Figure 26.

2197 In contrast, sources aligned with the parallactic angle
 2198 exhibit a tilted, linear distribution, clearly demonstrat-
 2199 ing that the relationship between angular offset and the
 2200 $g - i$ band magnitude difference, thereby providing a vi-
 2201 sual indication of the DCR effect. The DCR effect will
 2202 be addressed in future releases.

2203 5.5. Stellar Photometry

2204 The photometric repeatability for isolated bright un-
 2205 resolved sources following the FGCM fits was excellent.
 2206 For the 10% of unresolved sources withheld from the fit
 2207 and having signal-to-noise ratios greater than 100, the
 2208 photometric repeatability after applying chromatic cor-
 2209 rection was 7.1, 5.4, 5.4, 5.1, 5.9, and 6.5 mmag in the
 2210 $ugrizy$ bands respectively, across all fields. After ac-
 2211 counting for photometric noise, the intrinsic photomet-
 2212 ric repeatability was approximately 4.8, 2.7, 1.7, 1.0, 2.0,
 2213 and 1.1 mmag in $ugrizy$. The DP1 processing does not
 2214 yet include chromatic corrections in the final photome-
 2215 try. In this case the delivered photometric repeatability
 2216 was 3–8 mmag for $grizy$.

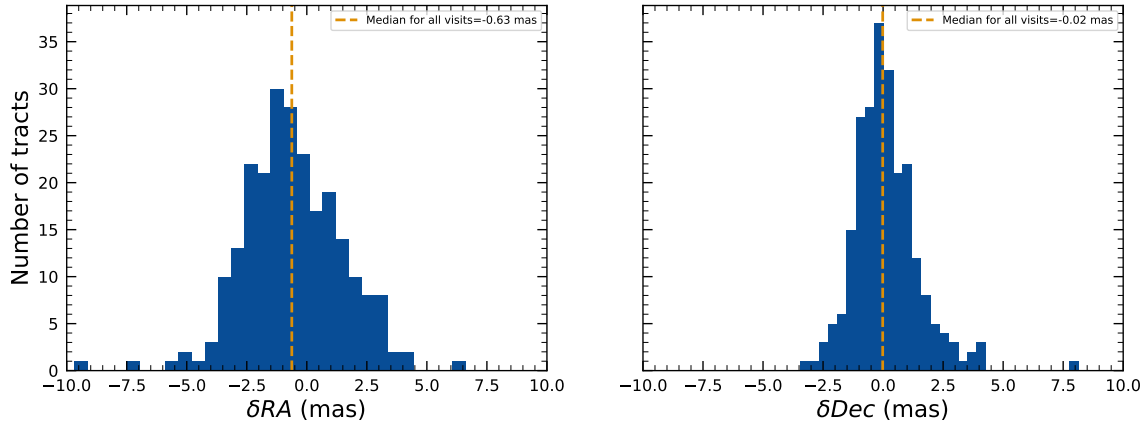


Figure 21. Median absolute offset for all visits in r -band in [tract 4849](#) in the ECDFS field. The offset is the difference between the positions of isolated point sources that were reserved from the astrometric fit and matched objects from the Gaia DR3 catalog.

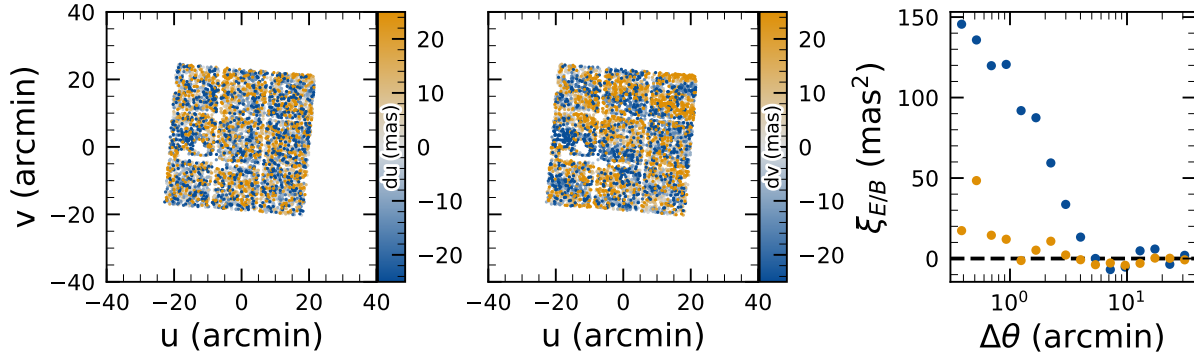


Figure 22. Astrometric residuals in u (left panel) and v (center panel) directions with the E (blue) and B (orange) modes of the two-point correlation function (right panel) seen in visit 2024120200359 in [tract 2393](#) in u band. The residuals show a wave-like pattern characteristic of atmospheric turbulence, and there is significant E-mode and negligible B-mode in the correlation function.

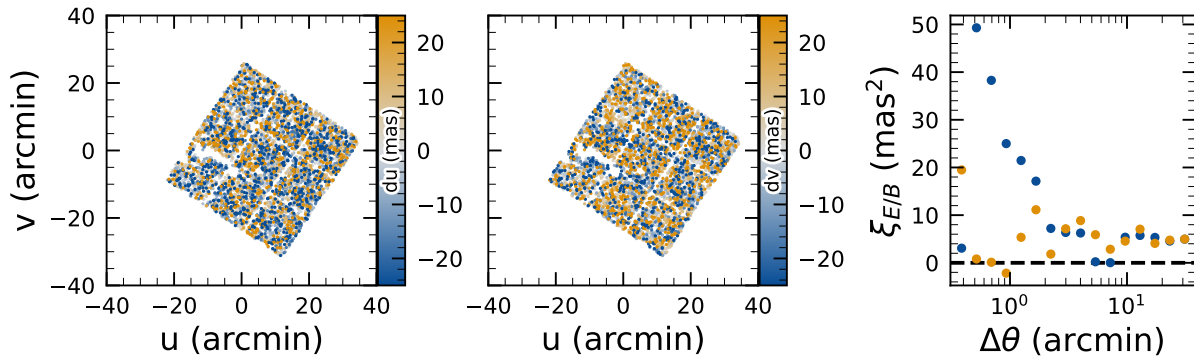


Figure 23. Astrometric residuals in u (left panel) and v (center panel) directions, with the E (blue) and B (orange) modes of the two-point correlation function (right panel) seen in visit 2024120700527 in [tract 2393](#) in u band. There are coherent residuals, but without the wave-like pattern seen in [Figure 22](#), and the correlation function has significant values for both E and B-modes.

2217 In [Figure 27](#), we show the stellar loci for $ugriz$ for un- 2219 unresolved sources were selected using the extendedness
2218 resolved sources in the `DP1 Object` table (§3.2). These

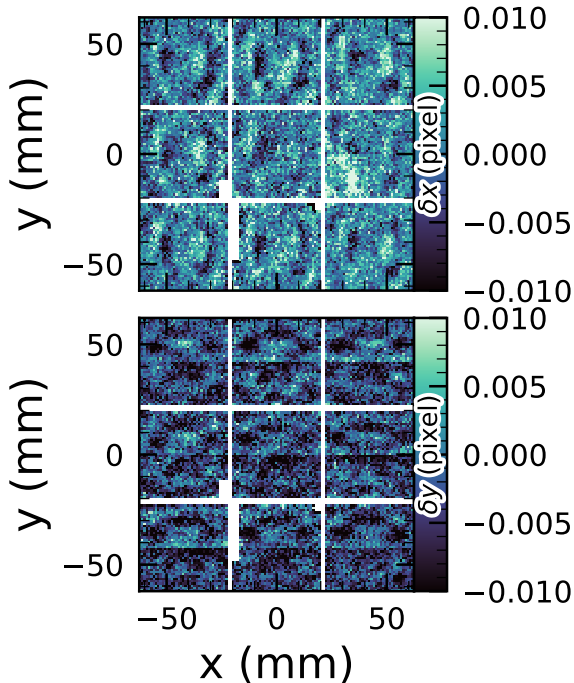


Figure 24. Median astrometric residuals as a function of focal plane position, shown in the left panel for the x direction and in the right panel for the y direction, for all nine LSSTComCam CCDs independently. The range of the color scale is ± 0.01 pixels, corresponding to 2 mas, showing that the effect is small.

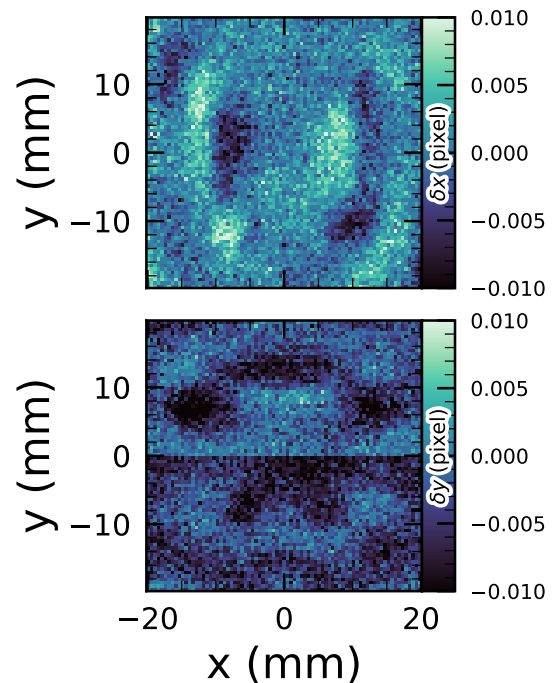


Figure 25. Median residuals as a function of pixel position, shown in the left panel for the x direction and in the right panel for the y direction. These residuals are aggregated across all nine CCDs that comprise the central LSSTComCam raft. The range of the color scale is ± 0.01 pixels, corresponding to 2 mas, showing that the effect is small.

parameter (§3.2) in the Object catalog. This parameter is assigned a value of 0 (unresolved) or 1 (resolved) in each band based on the difference between the PSF and CModel magnitudes. The extendedness is set to 1 when this magnitude difference exceeds 0.016 mag, as the PSF flux for extended sources is biased low relative to the CModel flux. This method has been previously employed by the SDSS pipelines, and its statistical properties, including the optimal combination of information from different bands and repeated measurements, are discussed in C. T. Slater et al. (2020).

Figure 28 illustrates the behavior of the extendedness parameter. Its behavior in the g and r bands is similar, with unresolved sources scattered around the vertical line centered on zero. The width of the distribution increases towards fainter magnitudes. Resolved sources are found to the right and the dashed lines in the top panels show the adopted “star-galaxy” separation boundary. The morphology of the two color-magnitude diagrams in the bottom panels suggest that the unresolved sample suffers from increasing contamination by galaxies for $r > 24$. This behavior is consistent with

simulation-based predictions from C. T. Slater et al. (2020).

5.6. Detection Completeness on Coadds

We characterize completeness by injecting synthetic sources into coadded images, and by comparing source detections to external catalogs. In both cases, we use a greedy, probabilistic matching algorithm that matches reference objects, in order of descending brightness, to the most likely target within a $0''.5$ radius.

We inject sources in 12 of the patches of the ECDFS region with the deepest coverage. The input catalog contains stars and galaxies from part of the Data Challenge 2 (DC2) simulations (LSST Dark Energy Science Collaboration (LSST DESC) et al. 2021), where the galaxies consist of an exponential disk and de Vaucouleurs (G. de Vaucouleurs 1948, 1953) bulge. To avoid deblender failures from excessive increases in object density, stars with a total flux (i.e., summed across all six bands) brighter than 17.5 mag are excluded, as are galaxies whose total flux is brighter than 15 mag or fainter than 26.5 mag. Half of the remaining objects are selected for injection. Afterwards, individual bulge and disk com-

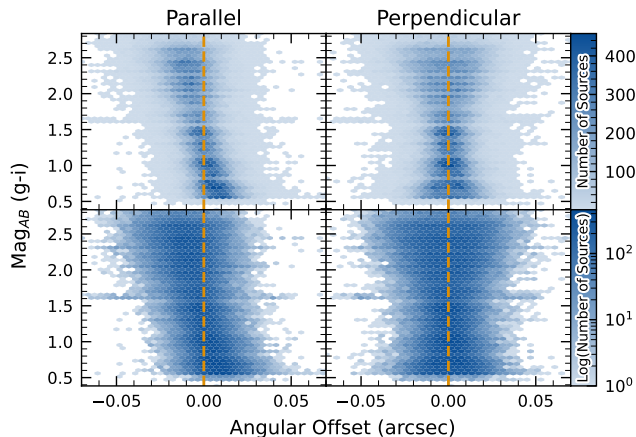


Figure 26. Visualization of [Differential Chromatic Refraction \(DCR\)](#) observed in the [LSSTComCam](#) commissioning campaign. The $g - i$ color is computed for every source in the reference catalog (§3.3.3) that is matched to a direct source in the science image, and the binned density for the full survey is plotted against the angular offset between the reference and detected positions. The angular offset is projected along coordinates parallel and perpendicular to the parallactic angle of the observation, and shows a characteristic correlation along the parallel axis with no correlation along the perpendicular axis. The orange vertical dashed line indicates the expected $g - i$ magnitude distribution at zero angular offset.

2265 ponents fainter than 29 mag are also excluded, both
 2266 for computational expediency and because their struc-
 2267 tural properties are less likely to be representative of
 2268 real galaxies.

2270 [Figure 29](#) shows completeness as a function of mag-
 2271 nitude for these injected objects in the [ECDFS](#) field.
 2272 These completeness estimates are comparable to results
 2273 from matching external catalogs. Matching to the Hub-
 2274 ble Legacy Field catalog ([G. Illingworth et al. 2016](#);
 2275 [K. E. Whitaker et al. 2019](#)) reaches 50% completeness
 2276 at $F775W = 26.13$, or about $i = 25.83$ from differences
 2277 in matched object magnitudes. Similarly, completeness
 2278 drops below 90% at $VIS = 23.80$ from matching to
 2279 [Euclid Q1](#) ([Euclid Collaboration et al. 2025](#)) objects,
 2280 equivalent to roughly $i = 23.5$. The [Euclid](#) imaging is of
 2281 comparable or shallower depth, so magnitude limits at
 2282 lower completeness percentages than 90% are unreliable,
 2283 whereas the [HST](#) images cover too small and irregular of
 2284 an area to accurately characterize 80-90% completeness
 2285 limits.

2286 At the 80% completeness limit, nearly 20% of objects,
 2287 primarily injected galaxies, are incorrectly classified as
 2288 stars based on their reference band extendedness. Sim-
 2289 ilarly, the fraction of correctly classified injected stars

2290 drops to about 50% at $i = 23.8$ (corresponding to 90%
 2291 completeness).

2292 This analysis has several caveats. The selection of
 2293 objects for matching in any catalog is not trivial. Some
 2294 fraction of the detections are spurious, particularly close
 2295 to bright stars and their diffraction spikes. Additionally,
 2296 some objects lie in masked regions of one survey but not
 2297 another, which has not been accounted for. For injected
 2298 source matching, the reference catalog (§3.3.3) does not
 2299 include real on-sky objects. Based on prior analyses of
 2300 the [DC2](#) simulations, purity is generally greater than
 2301 completeness at any given magnitude. Similarly, for
 2302 bright ($i < 23$) objects classified as stars by reference
 2303 band extendedness, $< 5\%$ are either unmatched to a [Euclid](#)
 2304 or [HST](#) object, or misclassified - that is, selecting on
 2305 extendedness alone yields a fairly pure but incomplete
 2306 sample of stars. We expect to remedy some of these
 2307 shortcomings in future releases.

2308 5.7. Model Flux and Shape Measurement

2309 [Figure 30](#) shows i -band magnitude residuals for
 2310 [CModel](#) and [Sérsic](#) measurements using the matched in-
 2311 jected galaxies described in §5.6. Similar behavior is
 2312 seen in other bands. [Sérsic](#) fluxes show reduced scatter
 2313 for galaxies with $i < 22.5$, though [CModel](#) fluxes are
 2314 less biased, with median residuals closer to zero and less
 2315 magnitude-dependent. For fainter objects, [Sérsic](#) fluxes
 2316 are more biased and less accurate. The magnitude of
 2317 this bias is considerably larger than previously seen in
 2318 simulated data. Subsequent testing indicates that this
 2319 bias can be (roughly) halved by fitting an exponential
 2320 model first, and then using those parameters to initialize
 2321 a free [Sérsic](#) fit. This approach will be adopted in future
 2322 releases. Aperture fluxes - including [Kron](#) and [GAaP](#) -
 2323 are not shown as they are not corrected to yield total
 2324 fluxes. The correction for [Kron](#) fluxes can be derived
 2325 from the [Sérsic](#) index ([A. W. Graham & S. P. Driver](#)
 2326 [2005](#)), but this correction is not provided in object ta-
 2327 bles.

2328 [Figure 31](#) shows $g - i$ color residuals versus r -band
 2329 magnitude for the same sample of galaxies as [Figure 30](#).
 2330 For this and most other colors, [GAaP](#) (with a $1''$ aper-
 2331 ture) and [Sérsic](#) colors both yield lower scatter; however,
 2332 the [CModel](#) colors have the smallest bias. Curiously,
 2333 the [GAaP](#) bias appears to be magnitude-dependent,
 2334 whereas the [Sérsic](#) bias remains stable from $19 < r < 26$.
 2335 Any of these color measurements are suitable for use
 2336 for deriving quantities like photometric redshifts, stellar
 2337 population parameters, etc.

2338 In addition to photometry, some algorithms include
 2339 measurements of structural parameters like size, ellip-
 2340 ticity, and [Sérsic](#) index. One particular known issue is

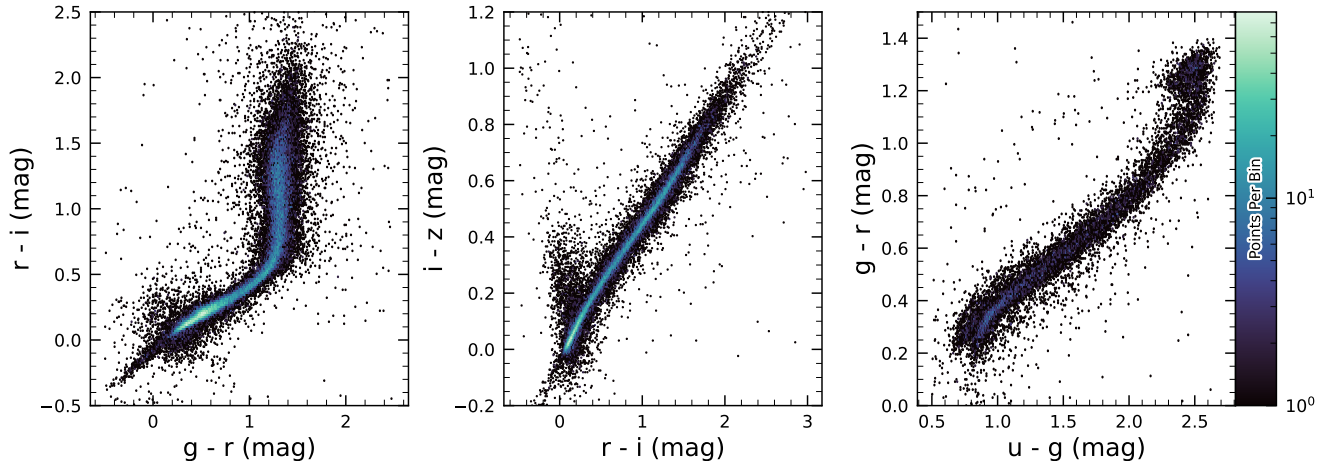


Figure 27. Examples of stellar loci for unresolved sources from the DP1 dataset. From left to right: *gri* stellar locus containing 63,236 stars with signal-to-noise ratio > 200 in the *i* band; *riz* stellar locus containing 46,760 stars with signal-to-noise ratio > 200 in the *i* band; *ugr* stellar locus containing 12,779 stars with signal-to-noise ratio > 50 in the *u* band.

2341 that many (truly) faint objects have significantly over-
 2342 estimated sizes and fluxes. This was also seen in the Dark
 2343 Energy Survey (K. Bechtol et al. 2025), who dubbed
 2344 such objects “super-spreaders”. These super-spreaders
 2345 contribute significantly to overestimated fluxes at the
 2346 faint end (see e.g. Figure 30), and are particularly prob-
 2347 lematic for the Kron algorithm (R. G. Kron 1980), which
 2348 should only be used with caution.

2349 As mentioned in §4.5, the Sérsic fits include a free
 2350 centroid, which is initialized from the fiducial centroid
 2351 of the object. Preliminary analyses of matched injected
 2352 objects suggest that the Sérsic model galaxy *astrom-*
 2353 *etry* residuals are somewhat smaller than for the stan-
 2354 dard centroids used in other measurements, and so users
 2355 of the Sérsic photometry should also use these centroid
 2356 values. One caveat is that for faint objects and/or in
 2357 crowded regions with unreliable deblending, free cen-
 2358 troids can drift significantly and potentially towards
 2359 other objects, so objects with large differences between
 2360 the fiducial and Sérsic *astrometry* should be discarded
 2361 or used with caution.

2362 Sérsic model parameter uncertainties are estimated
 2363 by computing and inverting the Hessian matrix with
 2364 the best-fit parameter values, after replacing the pixel
 2365 data (but not uncertainties) by the best-fit model values.
 2366 Currently, only the on-diagonal dispersion term (square
 2367 root of the variance) is provided as an error estimate for
 2368 each parameter. Future releases may provide more off-
 2369 diagonal terms of the covariance matrix - particularly
 2370 for the structural parameters, which are known to be
 2371 correlated.

2372 A major outstanding issue is that many parameter
 2373 uncertainties - including but not limited to those for

2374 fluxes - are underestimated. This is at least partly (but
 2375 not wholly) due to the fact that coaddition introduces
 2376 covariance between pixels, which is not captured in per-
 2377 pixel variances.

2378 The degree to which uncertainties are underestimated
 2379 can depend on the parameter in question and on the
 2380 brightness of the object. In plots of uncertainty-scaled
 2381 residuals, the ideal behavior is for the median (i.e. the
 2382 bias) to lie close to zero, and for the $\pm 1\sigma$ lines to lie at
 2383 ± 1 , without any dependence on magnitude. Figure 32
 2384 shows that flux and color uncertainties for PSF model
 2385 magnitudes of injected stars are both underestimated,
 2386 but by a factor of approximately 1.7–2 that is not very
 2387 sensitive to SNR. This holds for astrometric/centroid
 2388 parameters as well.

2389 In turn, Figure 33 shows that CModel color uncertain-
 2390 ties of galaxies are underestimated by a similar factor at
 2391 the faint end, but with appreciable scaling with mag-
 2392 nitude (and thereby SNR). Flux error underestimation
 2393 is both larger than for colors and scales more strongly
 2394 with SNR. This indicates that systematic effects domi-
 2395 nate the errors in fluxes, particularly for bright galaxies.
 2396 This is also at least partly but not wholly due to so-
 2397 called model inadequacy - that is, the fact that galaxy
 2398 models, parameteric or otherwise, are insufficiently com-
 2399 plex to capture the structure of real galaxies.

2400 Figure 34 shows that Sérsic model fluxes and colors
 2401 have similar behavior as CModel, but with a greater
 2402 degree of overestimation. This may be partly due to the
 2403 fact that Sérsic parameter uncertainties are estimated
 2404 along with the free centroid and structural (shape and
 2405 Sérsic index) parameters, whereas the forced CModel

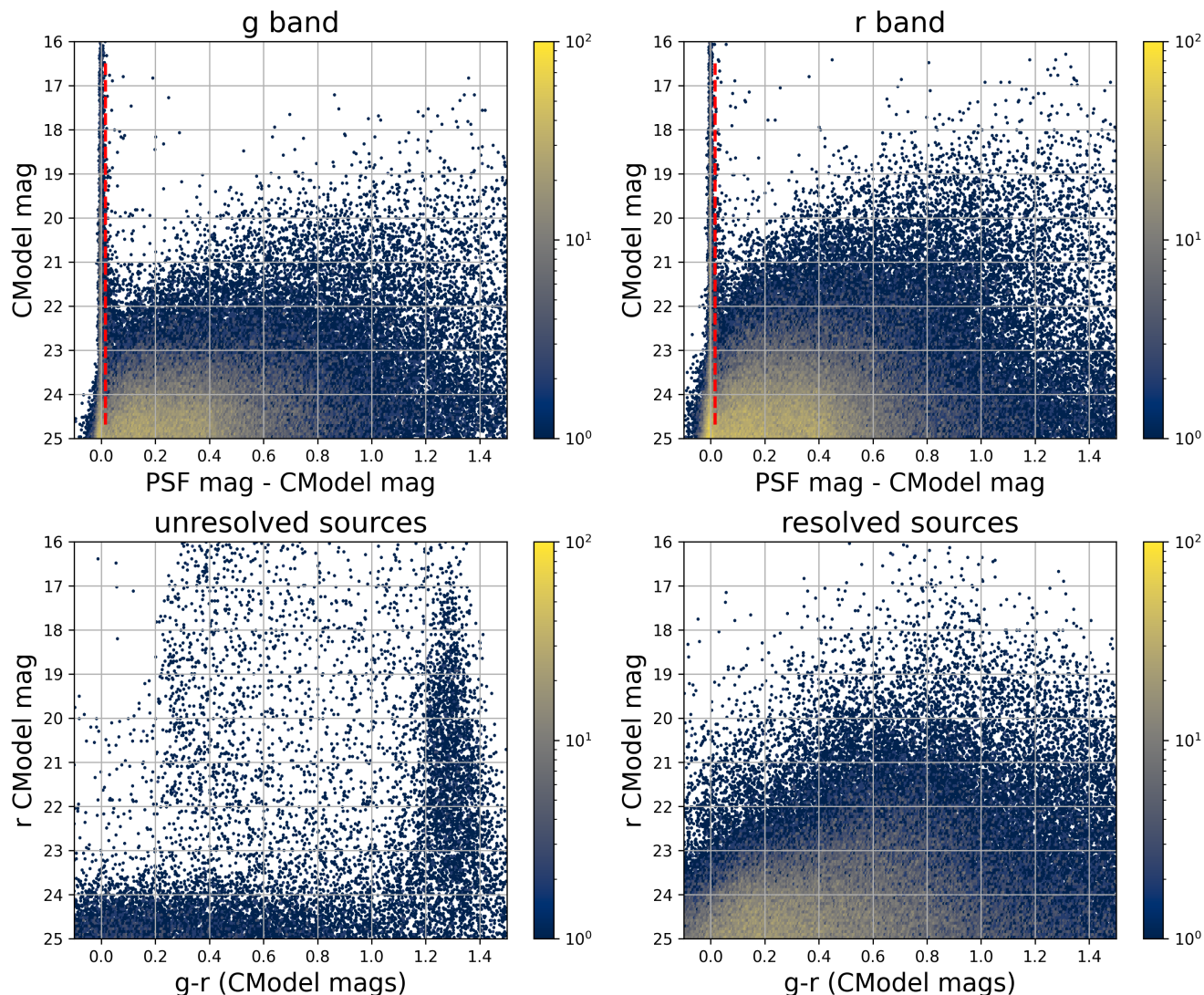


Figure 28. The top two panels shows the difference between the PSF and CModel magnitudes as a function of CModel magnitude in the g and r bands for 178,547 sources with $CModel_r < 25$ from the ECDFS field. The vertical dashed line in each panel marks the minimum value (0.016 mag) for setting the extendedness parameter to 1. The bottom two panels show the r vs. $g - r$ color-magnitude diagrams for 14,701 unresolved (left) and 163,666 resolved (right) sources. Note the unresolved sample suffers from increasing contamination by galaxies for $r > 24$.

2406 fluxes and errors are derived from linear flux fits with a 2416
 2407 fixed shape and centroid.

2408 Efforts are underway to investigate and quantify the 2417
 2409 origin of uncertainty underestimates and future releases 2418
 2410 will, at the least, provide recommendations for mitiga- 2419
 2411 tions. 2420

2412 5.8. Difference Imaging

2413 We assessed the performance of image differencing using 2426
 2414 both human vetting (§5.8.1) and source injection 2427
 2415 (§5.8.2). 2428

5.8.1. Difference Imaging Purity

2417 Members of the DP1 team labeled more than 11,000
 2418 DIASource image triplets, each consisting of cutouts
 2419 from the science, template, and difference images. An
 2420 internal labeling service (`tasso`) was deployed within
 2421 the USDF environment. A random subset of approx-
 2422 imately 16,000 DIASources was selected and uploaded
 2423 to the service, which remained active for roughly three
 2424 months and labeled by members of the DP1 team. Users
 2425 labeled DIASource PNG images triplets, each consist-
 2426 ing of cutouts from the science, template, and differ-
 2427 ence images. Each stamp had dimensions of 51×51 pix-
 2428 els, matching the input size required by the machine-

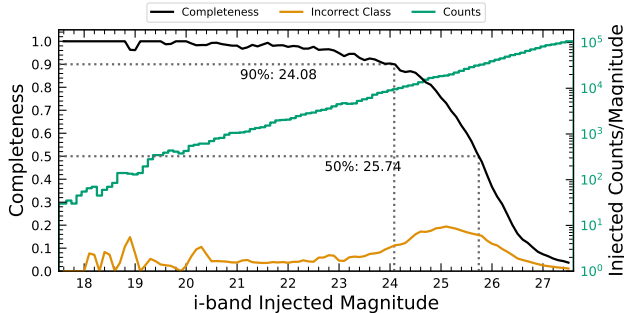


Figure 29. Completeness and incorrect classification fraction as a function of i -band CModel magnitude (Reference Magnitude) for DC2-based injected objects into a portion of the ECDFS field. The “Incorrect Class” line shows the proportion of objects that are matched but classified incorrectly by their reference-band extendedness, i.e. stars with extendedness of 1 or galaxies with extendedness of 0 in the reference band.

learning model. Access to the labeling service was granted to all individuals with commissioning data access. Each DIASource was classified exactly once, with a total of 35 volunteers contributing labels. Figure 35 show an example of one of the image triplets consisting of cutouts from the science, template, and difference images that volunteers were asked to label.

The labeled sources were classified into multiple categories representing real astrophysical events and artifacts. Prior to any filtering, the raw artifact-to-real ratio was approximately 9:1. Bright stars were identified as the dominant source of artifacts, while correlated noise, particularly in the u and g bands, also produced spurious detections near the flux threshold. We expect to be able to mitigate these effects in future LSSTCam data.

Applying a reliability threshold based on the Machine Learning reliability model described in §4.6.1 improved the purity of transient detections but had limited impact on variable stars. This limitation arises from technical constraints at the time of model training, which prevented the injection of variable stars into the synthetic training set. Future reliability models for LSST-Cam data, described in §4.6.1, will be trained using a broader and more representative range of input data.

The performance of the reliability model on the test data (§4.6.1) is shown in Figure 36. The rate of true positives and false negatives obtained by thresholding the reliability score at 0.5 is reported for transients (99 stamps), and variable stars (316 stamps) vetted in `tasso` in Table 6.

Additionally we crossmatched stamps with Solar System Objects with known orbits retrieving 5,988 Solar System Objects stamps.

Table 6. The rate of true positives (TP) and false negatives (FN) obtained by thresholding the reliability score at 0.5 for Solar system objects, transients and variable stars.

Object Type	Number	TP Rate	FN Rate
Solar System	5,988	93.5%	6.5%
Transients	99	73.7%	26.3%
Variables	316	3.5%	96.5%

5.8.2. Difference Imaging Detection Completeness

We assess the performance of our difference imaging pipeline using synthetic source injection on the science images prior to differencing. We construct a catalog of injected sources by joining two different samples of point sources, a set of hosted sources to emulate transients in galaxies and second set of hostless sources. The hosts are selected from the pipeline source catalog that is produced upstream by imposing a cut on their extendedness measurement and selecting $N_{\text{src}} = \min(100, N \times 0.05)$ of the N available sources per detector. For each host we pick a random position angle and radius using its light profile shape to decide where to place the source, and also a random value of brightness for the injected source, with magnitudes higher than the host source.

The hostless sources instead have random positions in the CCD focal plane, and magnitudes chosen from a random uniform distribution with $20 \geq m \geq m_{\text{lim}} + 1$, where m_{lim} is the limiting magnitude of the image. We used the LSST `source_injection` package¹⁰⁷ to include these sources in our test images. We performed a coordinate cross-match task, with a threshold of $0''.5$ to find which of these sources were detected and which were lost, enabling the calculation of a set of performance metrics.

In Figure 37 we show the detection completeness as a function of the SNR, for sources in the ECDFS field, for filters $griz$. We observe a completeness $> 95\%$ for sources with $\text{SNR} > 6$, with mean completeness $\simeq 99\%$ and standard deviation of $\simeq 0.7\%$. In Figure 38 we show the distribution of the residuals of the recovered sky coordinates for the detected synthetic sources. The marginal distributions are both centered at zero, and for sources of $\text{SNR} > 20$ the residuals are compatible with normal distributions $\mathcal{N}(\mu = 0, \sigma^2 = (0''.02)^2)$. In Figure 39 we show photometry results for our detected synthetic sources in the i filter, using PSF photometry

¹⁰⁷ <https://pipelines.lsst.io/modules/lsst.source.injection/index.html>

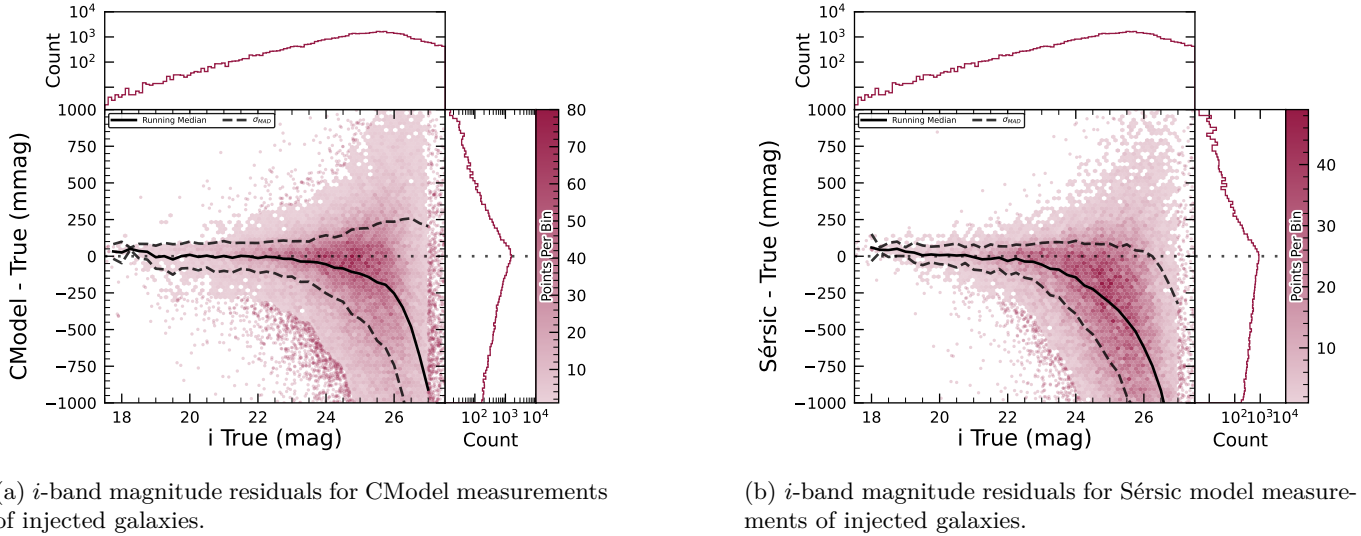


Figure 30. i -band magnitude residuals for matched injected DC2 galaxies with the CModel and Sérsic algorithms in a portion of the ECDFS region, including the median and scatter thereof. The black line is the median.

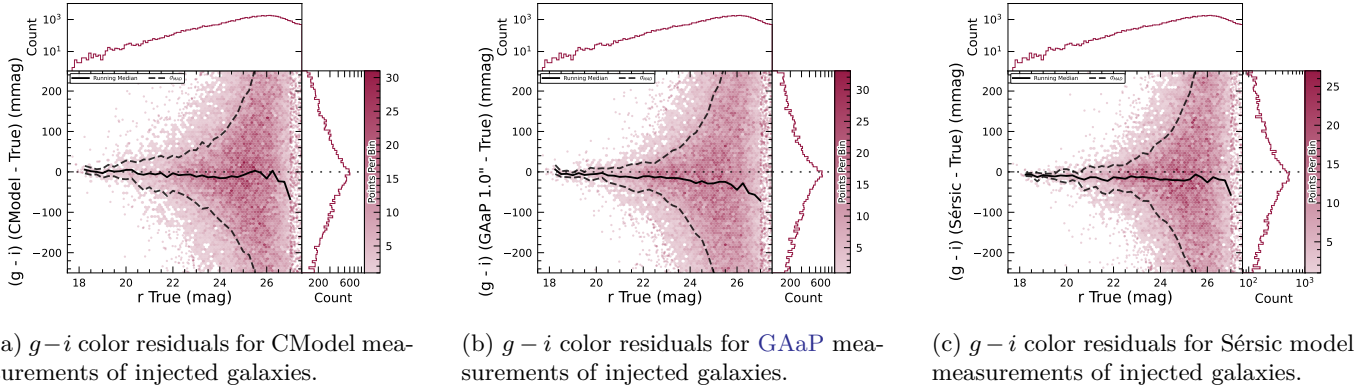


Figure 31. $g-i$ color residuals versus true r -band magnitude for matched injected DC2 galaxies with the CModel, GAaP and Sérsic algorithms in a portion of the ECDFS region.

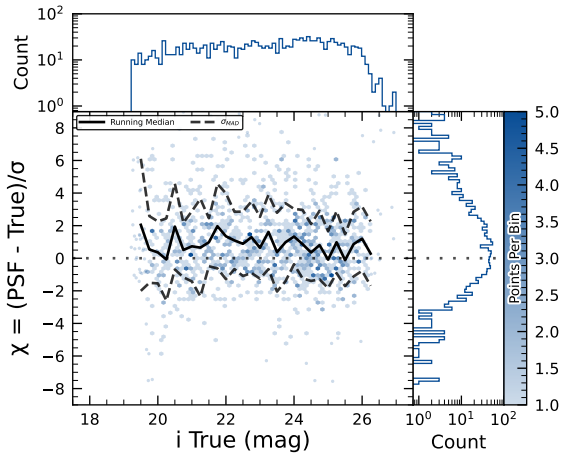
2503 on the difference images. We include both the mag- 2521
 2504 nitude residuals as well as the flux pulls, defined as 2522
 2505 $(f_{PSF} - f_{True})/\sigma_{f_{PSF}}$, where f_{True} is the true flux, f_{PSF} 2523
 2506 is the PSF flux and $\sigma_{f_{PSF}}$ is its uncertainty, as a function 2524
 2507 of the true magnitude of the synthetic sources, includ- 2525
 2508 ing the running median and median absolute deviation 2526
 2509 (MAD) for the whole brightness range. We also include 2527
 2510 the true magnitude distribution as well as the detection 2528
 2511 completeness on the top panel, and for reference the 2529
 2512 90% and 50% completeness magnitude values in vertical 2530
 2513 lines. On the right panels we include the marginal dis- 2531
 2514 tribution for sources brighter than 22.5 mag, splitting 2532
 2515 the data into hosted and hostless, as well as the robust 2533
 2516 mean and standard deviation. From this figure we can 2534
 2517 see that our flux measurements are accurate within a 2535
 2518 wide range of magnitudes, for both hosted and hostless 2536
 2519 synthetic sources. We find that the median offset is be- 2537
 2520 low 0.002 mag for true magnitudes below 21, and with a 2538

2521 maximum σ_{MAD} scatter of about 0.02 mag in this range. 2522
 2523 For true $m_i < 22.5$, the robust running median PSF 2524
 2525 magnitudes residuals are < 0.02 mag, and when split- 2526
 2527 ting into hosted and hostless both robust median are 2527
 2528 well below 0.01, and robust σ , i.e. σ_{MAD} are also well 2528
 2529 below 0.05. For all sources with $m_i < 21.5$ the running 2529
 2530 median is always $|\langle \delta \rangle| < 0.1$, and MAD $\sigma_\delta < 1$. Extend- 2530
 2531 ing to sources with $m_i < 22.5$ then hostless sources have 2531
 2532 a robust mean pull below 0.02, with a robust standard 2532
 2533 deviation < 1.15 , while these parameters increase to 0.2 2533
 2534 and 1.2 for hosted sources, suggesting that we might 2534
 2535 have contamination from host background sources po- 2535
 2536 tentially biasing our fluxes. 2536

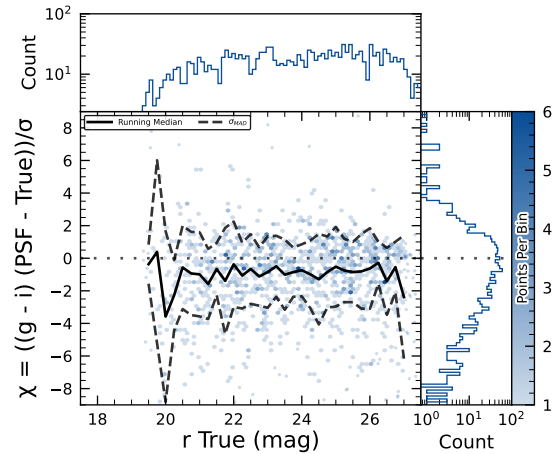
5.9. Solar System

5.9.1. Asteroid Linking Performance

2537 The evaluation of asteroid linking performance in DP1 2537
 2538 focused on demonstrating discovery capability. The so- 2538

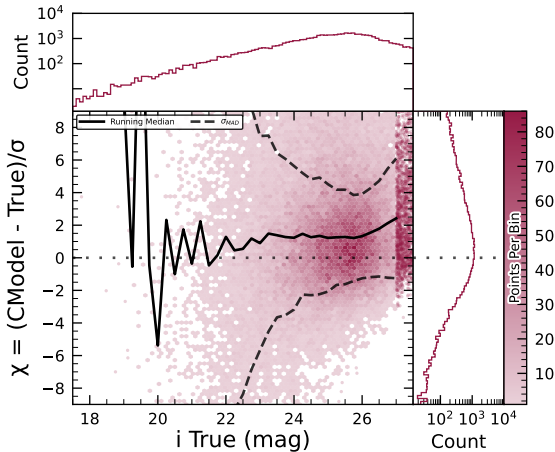


(a) i -band flux uncertainty-scaled residuals for PSF model measurements of injected stars.

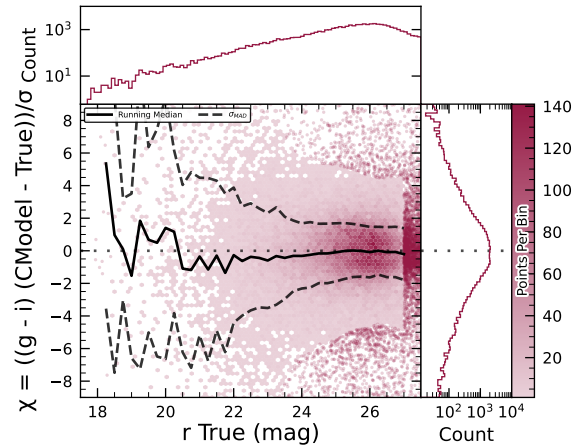


(b) $g - i$ color uncertainty-scaled residuals for PSF model measurements of injected stars.

Figure 32. Color and flux uncertainty-scaled residuals for matched injected DC2 stars' PSF model measurements in a portion of the ECDFS region.



(a) i -band flux uncertainty-scaled residuals for CModel measurements of injected galaxies.



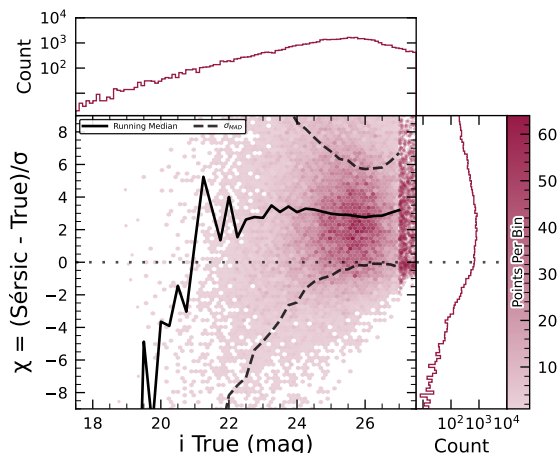
(b) $g - i$ color uncertainty-scaled residuals for CModel measurements of injected galaxies.

Figure 33. Color and flux uncertainty-scaled residuals for matched injected DC2 galaxies' CModel measurements in a portion of the ECDFS region.

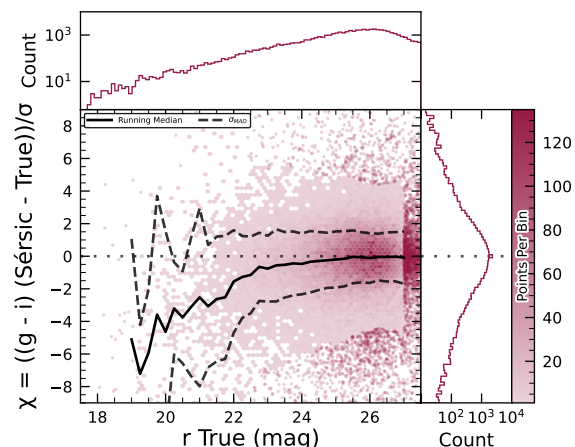
2539 lar system discovery pipeline produced 269,581 track- 2553
 2540 lets, 5,691 linkages, and 281 post-processed candidates. 2554

2541 As described in §4.6.3, post-processing of the heli- 2555
 2542 olinc output with link_purify produced a final set of 2556
 2543 281 candidate linkages, ranked with the most promising 2557
 2544 first. We then used find_orb (B. Gray 2025) to derive 2558
 2545 orbit fits for each candidate, sorting the resulting list by 2559
 2546 χ^2_{dof} , a measure of fit quality. A conservative manual 2560
 2547 investigation of these candidates yielded a curated 2561
 2548 list of 93 probable new asteroid discoveries. Manual 2562
 2549 inspection of the linkages indicated that those ranked 2563
 2550 0–137 corresponded to unique real asteroids; ranks 138– 2564
 2551 200 contained additional real objects intermixed with 2565
 2552 some spurious linkages; and ranks higher than 200 were 2566

essentially all spurious. This analysis indicates that it
 will be possible to identify cuts on quality metrics such
 as χ^2 to define discovery candidate samples with high
 purity; determining the exact quantitative cut values re-
 quires more data with LSSTCam. We next removed all
 observations matched to known asteroids (using Minor
 Planet Center (MPC)'s MPCChecker service), reducing
 the number of candidates to 97. Of these, four had
 strong astrometric and/or photometric outliers, likely
 due to self-subtraction in difference images due to the
 unavoidable limitations of template generation from the
 limited quantity of data available from LSSTComCam.
 We suspect these four linkages do correspond to real ob-
 jects, but have chosen to discard them out of an abun-



(a) i -band flux uncertainty-scaled residuals for Sérsic model measurements of injected galaxies.



(b) $g-i$ color uncertainty-scaled residuals for Sérsic model measurements of injected galaxies.

Figure 34. Color and flux uncertainty-scaled residuals for matched injected DC2 galaxies' Sérsic measurements in a portion of the ECDFS region.

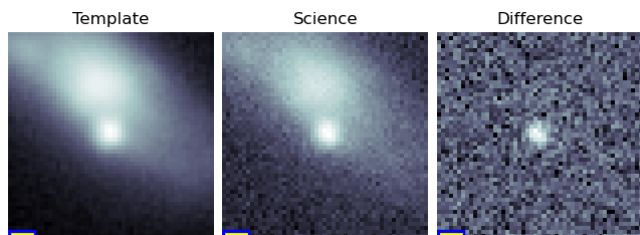


Figure 35. An example an image triplet consisting of cutouts showing, from left to right, the template, science, and difference images that volunteers were asked to label.

2567 dance of caution. The remaining 93 were submitted to
 2568 the Minor Planet Center and accepted as discoveries,
 2569 demonstrating the LSST pipelines are able to success-
 2570 fully discover new solar system objects.

5.9.2. Asteroid Association Performance

2572 During the Solar System association step, 5988 Di-
 2573 aSources were linked to 431 unique Solar System ob-
 2574 jects. These include 3,934 DiaSources with 338 previ-
 2575 ously known objects cataloged by the MPC, and 2,054
 2576 DiaSources with the 93 newly-discovered objects, all of
 2577 which are main belt asteroids. An additional 143 de-
 2578 tectations of these newly discovered objects were also re-
 2579 covered. These detections were not initially identified
 2580 by the discovery pipelines, as they did not meet the
 2581 required criteria for tracklet formation, specifically the
 2582 minimum number of detections and/or the maximum
 2583 allowed time span between observations.

2584 The astrometric residuals of known asteroid associa-
 2585 tions are shown in Figure 40. The astrometric precision
 2586 for solar system sources is excellent, with the majority of
 2587 objects detected within $0''.1$ of their expected positions.

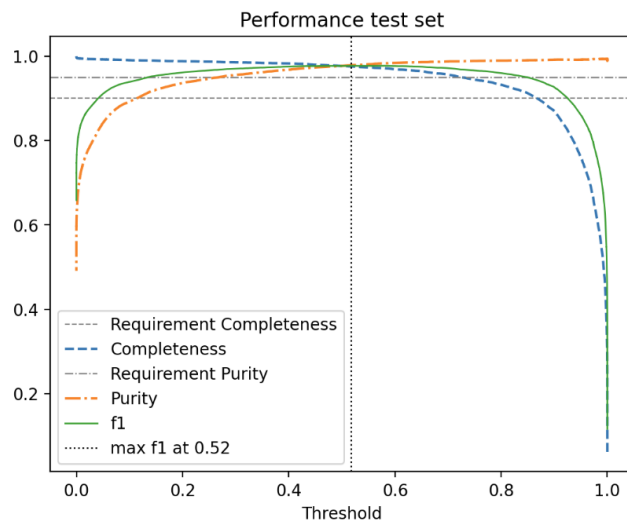


Figure 36. The purity and completeness of the reliability score is shown as a function of reliability threshold based on the testing data. A vertical line marks the threshold where the highest F1-score is obtained. The F1 score is the harmonic mean of completeness and purity. See §4.6.1 for details on the model and model training.

2588 By analyzing the signed median residuals to search for
 2589 biases, we find that previously-known objects have mean
 2590 residuals of $0''.001$ and $-0''.016$ in the RA and Dec di-
 2591 rections respectively, whereas newly-discovered objects
 2592 have mean residuals of $-0''.035$ and $-0''.010$ in the RA
 2593 and Dec directions, respectively. These mean residuals
 2594 are small enough to eliminate the possibility of a tim-
 2595 ing offset greater than the second-scale shutter motion,
 2596 which is consistent with the timing studies presented in
 2597 §2.2.2.

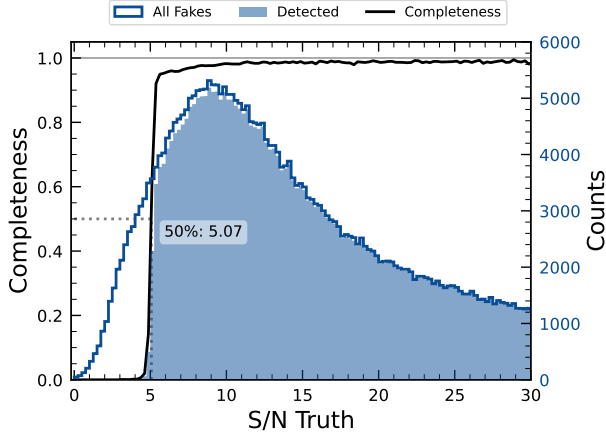


Figure 37. The difference image detection completeness for injected sources in the ECDFS field, for filters *griz*, as a function of the estimated signal to noise ratio SNR. This completeness is the ratio between the found fake sources (shaded histogram) and all the sources (solid line). The horizontal dashed line represents where the 50% completeness level is reached, at approximately $\text{SNR} \simeq 5.07$.

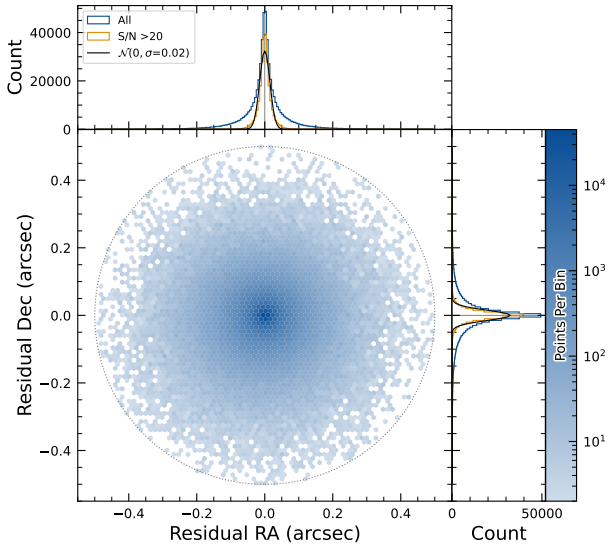


Figure 38. Coordinate residuals for detected synthetic sources in difference images, between recovered and true position of the sources in the ECDFS field. In the top and right panels we include the distribution of these offsets, for all sources as well as for sources with $\text{SNR} > 20$. These high SNR sources show gaussian coordinate residual distributions with $\sigma = 0''.02$ (black solid lines). The circle reflects the matching radius of $0''.5$.

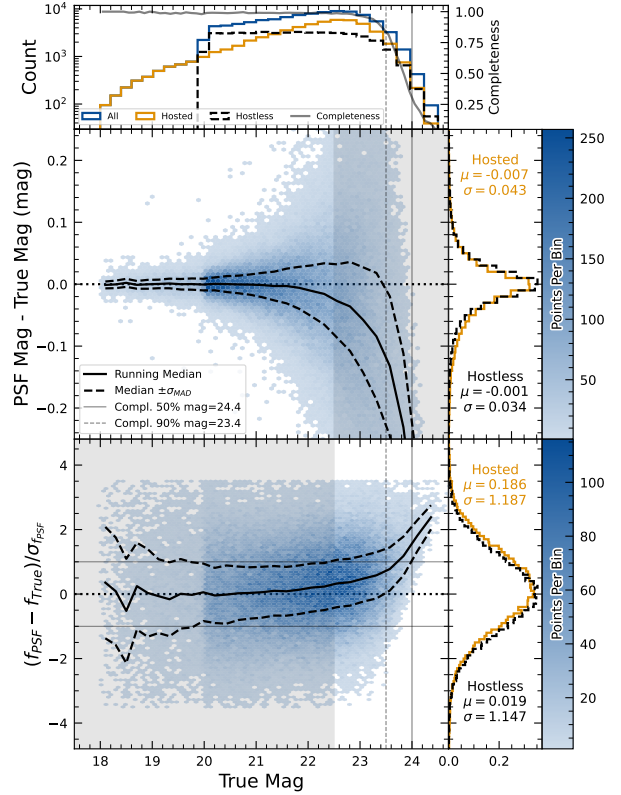


Figure 39. Magnitude residuals and flux pulls for *i*-band PSF photometry on difference images for ECDFS field in *i* for detected injected sources. Top panel: Distribution of true magnitudes for injected sources (blue), and split into hostless (black dash) and hosted (orange) sources, with detection completeness as a function of true magnitude (gray line). Vertical dashed lines indicate the 90% and 50% completeness magnitude limits. Center left panel: 2D hexbin plot of PSF magnitude residuals (measured minus true) versus true magnitude for detected sources, with running median (solid black) and σ_{MAD} (dashed black) overlaid. Center right panel: Marginalized distributions of PSF magnitude residuals for hostless (blue) and hosted (orange) sources with true magnitude $m_i < 22.5$, annotated with robust mean and standard deviation. Bottom left panel: 2D hexbin plot of PSF flux pulls versus true magnitude for detected sources, with running median (solid black) and σ_{MAD} (dashed black) overlaid. Bottom right panel: Marginalized distributions of PSF flux pulls for hostless (blue) and hosted (orange) sources with true magnitude $m_i < 22.5$, annotated with robust mean and standard deviation.

2598 The wider scatter in the RA residuals is due to ob-
 2599 jects whose measured orbital elements are less well con-

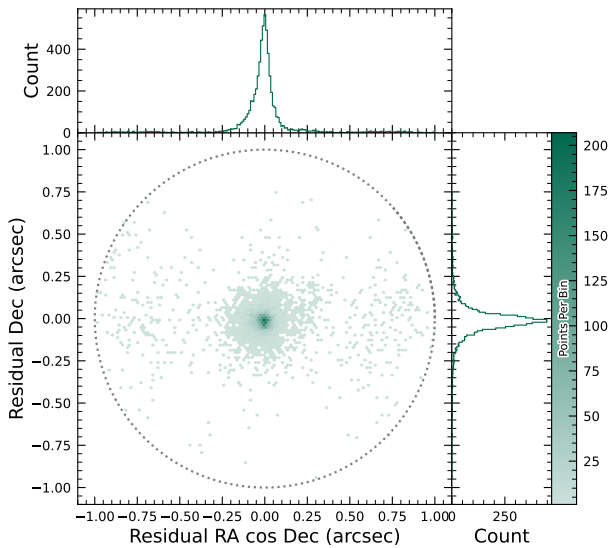


Figure 40. Astrometric residuals between expected and observed positions of Solar System Objects in DP1. The median residuals are $0''.001$ and $-0''.016$ in R.A./Dec direction, with standard deviations of $0''.19$ and $0''.10$, respectively. No detectable systematic offset from zero indicates there are no major errors in either timing or astrometry delivered by the Rubin system. The wider scatter in the RA direction is due to objects whose measured orbital elements are less well constrained, translating to larger along-track positional errors in the predicted positions.

strained, translating to larger along-track positional errors in the predicted positions. Observations of objects with large residuals are the most valuable ones from the point of view of improving the orbit, which is why we kept a generous matching radius. However, in future releases we are likely to couple this with either orbit fitting to verify the “singleton” match, or require two near-in-time observations (a tracklet) that match the expected motion vector as well.

Optimal moving source attribution is an area of active work that we expect to fully converge in time of Data Release 1 (DR1). In the meantime, for DP1 we’ve opted to start with simple, more easily understandable, criteria.

5.10. Crowded Fields

Among the seven Rubin DP1 target fields, two stand out for their severe stellar crowding: the globular cluster 47 Tucanae (47_Tuc) and the Fornax dwarf spheroidal galaxy (Fornax dSph). These fields were selected in part to stress-test the LSST Science Pipelines under high-density conditions. While both exhibit high stellar den-

sities, the nature and spatial extent of the crowding differ significantly.

47 Tuc presents extreme crowding across much of the field, encompassing its dense core and the eastern regions influenced by the Small Magellanic Cloud (SMC). This pervasive crowding leads to persistent challenges for deblending and reliable source detection, exposing field-wide limitations in the current pipeline performance (Y. Choi et al. 2025). In contrast, Fornax dSph shows significant crowding only in its central region, with outer areas remaining well resolved and easier to process.

In both 47 Tuc and Fornax, extreme crowding led to the deblending step being skipped frequently when memory or runtime limits were exceeded, typically due to an excessive number of peaks, or large parent footprints. However, the impact of these limitations differed: in 47 Tuc, deblending was often skipped across the entire field, resulting in large gaps and substantially reduced completeness. In Fornax, these issues were largely confined to the central region, with much better recovery in the outskirts. This contrast highlights how the pipeline’s limitations depend on the spatial extent of high-density regions: 47 Tuc exposed systematic, field-wide challenges, whereas Fornax revealed more localized, density-driven limits.

T. M. Wainer et al. (2025) explored the Rubin DP1 DiaObject catalog (§3.2) in the 47 Tuc field, which contains sources detected in difference images. Because forced photometry is performed at these positions across all single-epoch images, this dataset bypasses the coadd-based detection and deblending stages that often fail in crowded regions. By computing the median of the forced photometry for each DiaObject across available visits, they recovered approximately three times more candidate cluster members than found in the standard Object table (Y. Choi et al. 2025). This result underscores the value of difference-imaging-based catalogs for probing dense stellar regions inaccessible to standard coadd processing in DP1.

Although the DP1 pipeline was not optimized for crowded-field photometry, these early studies of 47 Tuc and Fornax provide critical benchmarks. They highlight both the limitations and opportunities for science with Rubin data in crowded environments, and they inform future pipeline development aimed at robust source recovery in complex stellar fields.

6. RUBIN SCIENCE PLATFORM

The RSP (M. Jurić et al. 2019) is a powerful, cloud-based environment for scientific research and analysis of petascale-scale astronomical survey data. It serves

as the primary interface for scientists to access, visualize, and conduct next-to-the-data analysis of Rubin and LSST data. The RSP is designed around a “bring the compute to the data” principle, eliminating the need for users to download massive datasets. Although DP1 is much smaller in size (3.5 TB) than many current survey datasets, future LSST datasets will be far larger and more complex, making it crucial to co-locate data and analysis for effective scientific discovery.

The RSP provides users with access to data and services through three distinct user-facing Aspects: a *Portal*, which facilitates interactive exploration of the data; a JupyterLab-based *Notebook* environment for data analysis using Python; and an extensive set of *Application Programming Interfaces (APIs)* that enable programmatic access to both data and services. The three Aspects are designed to be fully integrated, enabling seamless workflows across the RSP. The data products described in §3 are accessible via all three Aspects, and the system facilitates operations such as starting a query in one Aspect and retrieving its results in another. Figure 41 shows the Rubin Science Platform landing page in the Google cloud.

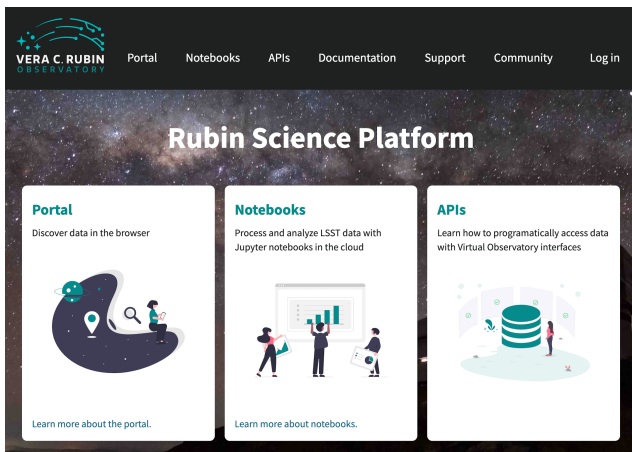


Figure 41. The Rubin Science Platform landing page at <https://data.lsst.cloud/> showing the three user-facing Aspects as well as links to documentation and support information.

The RSP is supported by a number of back-end services, including databases, files, and batch computing. Support for collaborative work through shared workspaces is also included in the RSP.

A preview of the RSP was launched on Google Cloud in 2022, operating under a shared-risk model to support Data Preview 0 (W. O’Mullane et al. 2024a). This allowed the community to test the platform, begin preparations for science, and provide valuable feedback to inform ongoing development. It was the first time an as-

tronomical research environment was hosted in a cloud environment. The DP1 release brings major updates to RSP services, enhancing scientific analysis capabilities. The RSP remains under active development, with incremental improvements being rolled out as they mature. During the Rubin Early Science Phase, the RSP will continue to operate under a shared-risk model. This section outlines the RSP functionality available at the time of the DP1 release and provides an overview of planned future capabilities.

6.1. Rubin Data Access Center

The Rubin US Data Access Center (US DAC) utilizes a novel hybrid on-premises-cloud architecture, which combines on-premises infrastructure at the USDF at SLAC with flexible and scalable resources in the Google cloud. This architecture has been deployed and tested using the larger simulated data set of DP0.2 (W. O’Mullane et al. 2024b).

In this hybrid model, user-facing services are deployed in the cloud to support dynamic scaling in response to user demand and to simplify the provisioning and management of large numbers of science user accounts. The majority of the static data products described in §3 are stored on-premises at the USDF to benefit from cost-effective mass storage and close integration with Rubin data processing infrastructure, also located at the USDF. For imaging data, the Data Butler (§6.2.2) provides the interface between the cloud-based users and data services, and the on-premises data. For catalog data, a cloud-based TAP client (§6.2.1) submits queries to the on-premises Qserv database cluster (§6.5) and retrieves the results. In the initial DP1 deployment, catalog data is hosted at the USDF while image data is stored in the cloud. The full hybrid model will be rolled out and further tested following the release of DP1. The RSP features a single-sign-on authentication and authorization system to provide secure access for Rubin data rights holders (R. Blum & the Rubin Operations Team 2020).

6.2. API Aspect

The API Aspect provides a comprehensive set of user-facing interfaces for programmatic access to the DP1 data products, through both IVOA-compliant services and the Rubin Data Butler. IVOA services enable standard queries and integration with existing tools, while the Butler facilitates advanced data processing within the LSST Science Pipelines.

At the time of the DP1 release, some IVOA services are unavailable, and certain data products are only accessible via the Butler. This section provides

2757 an overview of the available [IVOA](#) services and Butler
2758 access.

2759 6.2.1. *IVOA Services*

2760 Rubin has adopted a [Virtual Observatory \(VO\)](#)-first
2761 design philosophy, prioritizing compliance with [IVOA](#)
2762 standard interfaces to foster interoperability, standard-
2763 ization, and collaboration. In cases where standardized
2764 protocols have yet to be established, additional services
2765 have been introduced to complement these efforts. This
2766 approach ensures that the RSP can be seamlessly inte-
2767 grated with community-standard tools such as [Tool for](#)
2768 [OPerations on Catalogues And Tables \(TOPCAT\)](#) (M.
2769 Taylor 2011) and [Aladin](#) (F. Bonnarel et al. 2000; T.
2770 Boch & P. Fernique 2014; M. Baumann et al. 2022), as
2771 well as libraries such as [PyVO](#) (M. Graham et al. 2014).

2772 The user-facing [APIs](#) are also used internally within
2773 the [RSP](#), creating a unified design that ensures consis-
2774 tent and reproducible workflows across all three Aspects.
2775 This reduces code duplication, simplifies maintenance,
2776 and ensures all users, both internal and external, access
2777 data in the same way. For example, an [Astronomical](#)
2778 [Data Query Language \(IVOA standard\) \(ADQL\)](#) query
2779 on the [Object](#) catalog via [TAP](#) yields identical results
2780 whether run from the Portal, Notebook, or an external
2781 client.

2782 The following [IVOA](#) services are available at the time
2783 of the [DP1](#) release:

- 2784 • **Table Access Protocol (TAP) Service:** A
2785 TAP service (P. Dowler et al. 2019) enables queries
2786 of catalog data via the [IVOA](#)-standard [ADQL](#), a
2787 dialect of [SQL92](#) with spherical geometry exten-
2788 sions. The main TAP service for [DP1](#) runs on the
2789 Rubin-developed [Qserv](#) database (§ 6.5), which
2790 hosts the core science tables described in §3.2, as
2791 well as the [Visit](#) database. It also provides image
2792 metadata in the [IVOA ObsCore](#) format via the
2793 standard `ivoa.ObsCore` table, making it an “Ob-
2794 sTAP” service (ObsTAP; M. Louys et al. 2017).
2795 The TAP service is based on the [Canadian As-](#)
2796 [tronomy Data Centre \(CADC\)](#)’s open-source Java
2797 TAP implementation¹⁰⁸, modified for the exact
2798 query language accepted by [Qserv](#). It currently
2799 supports a large subset of [ADQL](#), with limitations
2800 documented in the data release materials (see §7.1)
2801 and exposed via the TAP **capabilities** endpoint
2802 where possible.

2803 The TAP service provides metadata annotations
2804 consistent with the standard, including table and

2805 column descriptions, indications of foreign-key rela-
2806 tionships between tables, and column metadata
2807 such as units and [IVOA Unified Content Descrip-](#)
2808 [tors \(UCDs\)](#).

- **Image Access Services:** Rubin image access services are compliant with [IVOA SIAv2](#) (Simple Image Access Protocol, version 2; T. Jenness et al. 2024; P. Dowler et al. 2015) for discovering and accessing astronomical images based on metadata. SIAv2 is a [REpresentational State Transfer \(REST\)](#)-based protocol designed for the discovery and retrieval of image data. It allows, for instance, querying all images in a given band over a defined sky region and time period.

Users identify an image or observation of interest and query the service. The result set includes metadata about the image, such as the sky position, time, or band, and a data access URL, which includes an [IVOA Identifier](#) uniquely identifying the dataset (T. Jenness & G. P. Dubois-Felsmann 2025), allowing the dataset to be retrieved or a cutout requested via [Server-side Operations for Data Access \(IVOA standard\) \(SODA\)](#).

- **Image Cutout Service:** The Rubin Cutout Service (R. Allbery 2023, 2024) is based on the [IVOA SODA](#) standard (F. Bonnarel et al. 2017). Users submit requests specifying sky coordinates and the cutout size as the radius from the coordinates, and the service performs the operation on the full image and returns a result set. For [DP1](#), the cutout service is a single cutout service only where N cutout requests will require N independent synchronous calls. We expect some form of bulk cutout service by mid 2026.

- **HiPS Data Service:** An authenticated [HiPS](#) (P. Fernique et al. 2017) data service for seamless pan-and-zoom access to large-scale co-adds. It supports fast interactive progressive image exploration at a range of resolutions.

- **WebDAV:** A [Web Distributed Authoring and Versioning \(WebDav\)](#) service is provided to enable users to remotely manage, edit, and organize files and directories on the [RSP](#) as if they were local files on their own computer. This is especially useful for local development.

2850 6.2.2. *Data Butler*

2851 The Rubin Data Butler (T. Jenness et al. 2022; N. B.
2852 Lust et al. 2023), is a high-level interface designed to

¹⁰⁸ <https://github.com/opencadc/tap>

2853 facilitate seamless access to data for both users and
 2854 software systems. This includes managing storage for-
 2855 mats, physical locations, data staging, and database
 2856 mappings. A [Butler](#) repository contains two compo-
 2857 nents:

- 2858 • the *Data Store*: A physical storage system for
 2859 datasets, e.g., a [Portable Operating System Inter-](#)
 2860 [face \(POSIX\)](#) file system or S3 object store; and
- 2861 • the *Registry*: An [Structured Query Language](#)
 2862 [\(SQL\)](#)-compatible database that stores metadata
 2863 about the datasets in the data store.

2864 For DP1, the Butler repository is hosted in the Google
 2865 Cloud, using an [\(Amazon\) Simple Storage Service](#)
 2866 [\(S3\)](#)-compatible store for datasets and AlloyDB, a
 2867 PostgreSQL-compatible database, for the registry.

2868 In the context of the [Butler](#), a *dataset* refers to a
 2869 unique data product, such as an image, catalog or map,
 2870 generated by the observatory or processing pipelines
 2871 Datasets belong to one of the various types of data
 2872 products, described in §3. The [Butler](#) ensures that
 2873 each dataset is uniquely identifiable by a combination
 2874 of three pieces of information: a data coordinate,
 2875 a dataset type, and a run collection. For example,
 2876 a dataset that represents a single raw image in the
 2877 *i* band taken on the night starting 2024-11-11 with
 2878 exposure ID 2024111100074 would be represented as
 2879 `dataId='exposure':2024111100074, 'band':'i',`
 2880 `'instrument':'LSSTComCam'` and is associated with
 2881 the `raw` DatasetType. For a deep coadd on a [patch](#)
 2882 of sky in the Seagull field, there would be no exposure di-
 2883 mensions and instead the tract, [patch](#) and band would
 2884 be specified as `dataId='tract':7850, 'patch':`
 2885 `6, 'band':'g', 'instrument':'LSSTComCam',`
 2886 `skymap='lsst_cells_v1'` and is associated with the
 2887 `deep_coadd` DatasetType. The tract identification
 2888 numbers and corresponding target names for these
 2889 tracts are listed in [Table 7](#).

2890 The data coordinate is used to locate a dataset in
 2891 multi-dimensional space, where dimensions are defined
 2892 in terms of scientifically meaningful concepts, such as
 2893 instrument, visit, detector or band. For example, a cali-
 2894 brated single-visit image (§3.1) has dimensions includ-
 2895 ing band, instrument, and detector. In contrast, the
 2896 visit table (§3.2), a catalog of all calibrated single-epoch
 2897 visits in DP1, has only the instrument dimension. The
 2898 main dimensions used in DP1 are listed, together with a
 2899 brief description, in [Table 8](#). To determine which dimen-
 2900 sions are relevant for a specific dataset, the [Butler](#) de-
 2901 fines dataset types, which associate each dataset with its
 2902 specific set of relevant dimensions, as well as the associ-
 2903 ated Python type representing the dataset. The dataset

Table 7. Tract coverage of each DP1 field. The size of a tract is larger than the LSSTComCam field of view; however, since each observed field extends across more than one tract, each field covers multiple tracts.

Field Code	Tract ID
47_Tuc	453, 454
ECDFS	4848, 4849, 5062, 5063, 5064
EDFS_comcam	2234, 2235, 2393, 2394
Fornax_dSph	4016, 4017, 4217, 4218
Rubin_SV_095_-25	5305, 5306, 5525, 5526
Rubin_SV_38_7	10221, 10222, 10463, 10464, 10704, 10705
Seagull	7610, 7611, 7849, 7850

2904 type defines the kind of data a dataset represents, such
 2905 as a raw image (`raw`), a processed catalog (`object_`
 2906 `forced_source`), or a sky map (`skyMap`). [Table 9](#) lists
 2907 all the dataset types available via the Butler in DP1, to-
 2908 gether with the dimensions needed to uniquely identify
 2909 a specific dataset and the number of unique datasets of
 2910 each type.

2911 It is important to highlight a key difference between
 2912 accessing catalog data via the [TAP](#) service versus the
 2913 Butler. While the [TAP](#) service contains entire catalogs,
 2914 many of the same catalogs in the Butler are split into
 2915 multiple separate catalogs. This is partly due to how
 2916 these catalogs are generated, but also because of the
 2917 way data is stored within and retrieved from the Butler
 2918 repository – it is inefficient to retrieve the entire `Source`
 2919 catalog, for example, from the file system. Instead, be-
 2920 cause the `Source` catalog contains data for sources de-
 2921 tected in the `visit_images`, there is one `Source` catalog
 2922 in the Butler for each `visit_image`. Similarly, there is
 2923 one `Object` catalog for each `deep_coadd`. All the cata-
 2924 logs described in §3.2, aside from the `CcdVisit`, `SSOb-`
 2925 `ject`, `SSSource`, and `Calibration` catalogs, are split
 2926 within the Butler.

2928 A dataset is associated with one or more *Collections*;
 2929 logical groupings of datasets within the [Butler](#) system
 2930 that were created or processed together by the same
 2931 batch operation. Collections allow multiple datasets
 2932 with the same data coordinate to coexist without con-
 2933 flict. Collections support flexible, parallel processing by
 2934 enabling repeated analyses of the same input data using
 2935 different configurations. The DP1 Butler is read-only; a
 2936 writeable Butler is expected by mid-2026.

6.2.3. Remote Programmatic Access

2938 The Rubin [RSP API](#) can be accessed from a local sys-
 2939 tem by data rights holders outside of the [RSP](#), by creat-

Table 8. Descriptions of and valid values for the key data dimensions in DP1. YYYYMMDD signifies date and # signifies a single 0–9 digit.

Dimension	Format/Valid values	Description
day_obs	YYYYMMDD	A day and night of observations that rolls over during daylight hours.
visit	YYYYMMDD#####	A sequence of observations processed together; synonymous with “exposure” in DP1.
exposure	YYYYMMDD#####	A single exposure of all nine ComCam detectors.
instrument	LSSTComCam	The instrument name.
detector	0–8	A ComCam detector.
skymap	lsst_cells_v1	A set of tracts and patches that subdivide the sky into rectangular regions with simple projections and intentional overlaps.
tract	See Table 7	A large rectangular region of the sky.
patch	0–99	A rectangular region within a tract.
physical_filter	u_02, g_01, i_06, r_03, z_03, y_04	A physical filter.
band	u, g, r, i, z, y	An conceptual astronomical passband.

Table 9. The name and number of each type of data product in the Butler and the dimensions required to identify a specific dataset.

Data Product	Name in Butler	Required Dimensions	Number in DP1
Image Data Products			
raw	raw	instrument, detector, exposure	16125
visit_image	visit_image	instrument, detector, visit	15972
deep_coadd	deep_coadd	band, skymap, tract, patch	2644
template_coadd	template_coadd	band, skymap, tract, patch	2730
difference_image	difference_image	instrument, detector, visit	15972
Catalog Data Products			
Source	source	instrument, visit	1786
Object	object	skymap, tract	29
ForcedSource	object_forced_source	skymap, tract, patch	636
DiaSource	dia_source	skymap, tract	25
DiaObject	dia_object	skymap, tract	25
ForcedSourceOnDiaObject	dia_object_forced_source	skymap, tract, patch	597
SSSource	ss_source	–	1
SSObject	ss_object	–	1
Visit	visit_table	instrument	1
CcdVisit	visit_detector_table	instrument	1

2940 ing a user security token. This token can then be used
 2941 as a bearer token for API calls to the RSP TAP service.
 2942 This capability is especially useful for remote data anal-
 2943 ysis using tools such as TOPCAT, as well as enabling
 2944 third-party systems, e.g., Community Alert Brokers, to
 2945 access Rubin data. Additionally, it supports remote de-
 2946 velopment, allowing for more flexible workflows and in-
 2947 tegration with external systems.

2948 6.3. Portal Aspect

2949 The Portal Aspect provides an interactive web-based
 2950 environment for exploratory data discovery, filtering,
 2951 querying ,and visualization of both image and catalog
 2952 data, without requiring programming expertise. It en-
 2953 ables users to access and analyze large datasets via tools
 2954 for catalog queries, image browsing, time-series inspec-
 2955 tion, and cross-matching.

The Portal is built on [Firefly](#) (X. Wu et al. 2019), a web application framework developed by the Infrared Processing and Analysis Center (IPAC). [Firefly](#) provides interactive capabilities such as customizable table views, image overlays, multi-panel visualizations, and synchronized displays linking catalog and image data.

Designed to support both exploratory data access and detailed scientific investigation, the Portal delivers an intuitive user experience, allowing users to visually analyze data while retaining access to underlying metadata and query controls.

6.4. Notebook Aspect

The Notebook Aspect provides an interactive, web-based environment built on Jupyter Notebooks, enabling users to write and execute Python code directly on Rubin and [LSST](#) data without downloading it locally. It offers programmatic access to Rubin and [LSST](#) data products, allowing users to query and retrieve datasets, manipulate and display images, compute derived properties, plot results, and reprocess data using the [LSST Science Pipelines](#) (§4.1). The environment comes pre-installed with the pipelines and a broad set of widely used astronomical [software](#) tools, supporting immediate and flexible data analysis.

6.5. Databases

The user-facing Aspects of the [RSP](#) are supported by several backend databases that store catalog data products, image metadata, and other derived datasets. The [schema](#) for [DP1](#) and other Rubin databases are available online at <https://sdm-schemas.lsst.io>.

6.5.1. Qserv

The final 10-year [LSST](#) catalog is expected to reach 15 PB and contain measurements for billions of stars and galaxies across trillions of detections. To support efficient storage, querying, and analysis of this dataset, Rubin Observatory developed [Qserv](#) (D. L. Wang et al. 2011; F. Mueller et al. 2023) – a scalable, parallel, distributed SQL database system. [Qserv](#) partitions data over approximately equal-area regions of the celestial sphere, replicates data to ensure resilience and high availability, and uses shared scanning to reduce overall I/O load. It also supports a package of scientific user-defined functions (SciSQL: <https://smonkewitz.github.io/scisql/>) simplifying complex queries involving spherical geometry, statistics, and photometry. [Qserv](#) is built on robust production-quality components, including [MariaDB](#) (<https://www.mariadb.org/>) and [XRootD](#) (<https://xrootd.org/>). [Qserv](#) runs at the [USDF](#) and user access to catalog data is via the [TAP](#) service (§6.2.1).

This enables catalog-based analysis through both the [RSP](#) Portal and [Notebook](#) Aspects.

Although the small [DP1](#) dataset does not require [Qserv](#)’s full capabilities, we nevertheless chose to use it for [DP1](#) to accurately reflect the future data access environment and to gain experience with scientifically-motivated queries ahead of full-scale deployment. [Qserv](#) is open-source and available on [GitHub](#): <https://github.com/lsst/qserv>.

7. SUPPORT FOR COMMUNITY SCIENCE

Rubin Observatory has a science community that encompasses thousands of individuals worldwide, with a broad range of experience and expertise in astronomy in general, and in the analysis of optical imaging data specifically.

Rubin’s model to support this diverse community to access and analyze [DP1](#) emphasizes self-help via documentation and tutorials, and employs an open platform for asynchronous issue reporting that enables crowd-sourced solutions. These two aspects of community support are augmented by virtual engagement activities. In addition, Rubin supports its Users Committee to advocate on behalf of the science community, and supports the eight [LSST](#) Science Collaborations (§7.6).

All of the resources for scientists that are discussed in this section are discoverable by browsing the *For Scientists* pages of the Rubin Observatory website¹⁰⁹.

7.1. Documentation

The data release documentation for [DP1](#)¹¹⁰ provides an overview of the [LSSTComCam](#) observations, detailed descriptions of the data products, and a high-level summary of the processing pipelines. Although much of its content overlaps significantly with this paper, the documentation is presented as a searchable, web-based resource built using [Sphinx](#)¹¹¹, with a focus on enabling scientific use of the data products.

7.2. Tutorials

A suite of tutorials (NSF-DOE Vera C. Rubin Observatory 2021) that demonstrate how to access and analyze [DP1](#) using the [RSP](#) accompanies the [DP1](#) release¹¹². Jupyter Notebook tutorials are available via the “Tutorials” drop-down menu within the Notebook aspect of the [RSP](#). Tutorials for the Portal and API aspects of the [RSP](#) can be found in the data release documentation.

¹⁰⁹ <https://rubinobservatory.org/for-scientists>

¹¹⁰ <https://dp1.lsst.io>

¹¹¹ <https://www.sphinx-doc.org/>

¹¹² <https://dp1.lsst.io/tutorials>

These tutorials are designed to be inclusive, accessible, clear, focused, and consistent. Their format and contents follow a set of guidelines (M. L. Graham et al. 2026) that are informed by modern standards in technical writing.

7.3. Community Forum

The venue for all user support is the Rubin Community Forum¹¹³. Questions about any and all aspects of the Rubin data products, pipelines, and services, including DP1, should be posted as new topics in the Support category. This includes beginner-level and “how-to” questions, advanced scientific analysis questions, technical bug reports, account and data access issues, and everything in between. The Support category of the Forum is monitored by Rubin staff, who follow an established internal workflow for following-up and resolving all reported issues.

The Rubin Community Forum is built on the open-source Discourse platform. It was chosen because, for a worldwide community of ten thousand Rubin users, a traditional (i.e., closed) help desk represents a risk to Rubin science (e.g., many users with the same question having to wait for responses). The open nature of the Forum enables self-help by letting users search for similar issues, and enables crowd-sourced problem solving (and avoids knowledge bottlenecks) by letting users help users.

The Rubin Community Forum, and the internal staff workflows for user support, were set up, tested, and refined with DP0 so that it was ready for use with DP1.

7.4. Engagement Activities

A variety of live virtual and in-person workshops and seminars offer learning opportunities to scientists and students working with the Rubin data products, services, and tools.

- Rubin Science Assemblies (weekly, virtual, 1 hour): alternates between hands-on tutorials based on the most recent data release and open drop-in “office hours” with Rubin staff.
- Rubin Data Academy (annual, virtual, 3-4 days): an intense set of hands-on tutorials based on the most recent data release, along with co-working and networking sessions.
- Rubin Community Workshop (annual, virtual, 5 days), a science-focused conference of contributed

posters, talks, and sessions led by members of the Rubin science community and Rubin staff.

Following the release of DP1, all of these engagement activities focused on use of DP1 by the science community. In particular, the 2025 Rubin Data Academy was run the week of the DP1 release, in order to immediately facilitate community access. The 2025 Rubin Community Workshop had several sessions to introduce people to the DP1 dataset and demonstrate how to access and analyze it with the RSP.

For schedules, connection information, zoom recordings, and associated materials, visit the *For Scientists* pages of the Rubin Observatory website¹¹⁴. Requests for custom tutorials and presentations for research groups are also accommodated.

7.5. Users Committee

This committee is charged with soliciting feedback from the science community, advocating on their behalf, and recommending science-driven improvements to the LSST data products and the Rubin Science Platform tools and services. Community members are encouraged to attend their virtual meetings and raise issues to their attention, so they can be included in the committee’s twice-yearly reports to the Rubin Observatory Director.

Like the Forum, the Users Committee was established and began its work with DP0, and that feedback was implemented for DP1. The community’s response to DP1 will be especially valuable input to DP2 and DR1, and the Users Committee encourages all users to interact with them. For a list of members and contact information, visit the *For Scientists* pages of the Rubin Observatory website.

7.6. Science Collaborations

The eight LSST Science Collaborations are independent, worldwide communities of scientists, self-organized into collaborations based on their research interests and expertise. Members work together to apply for funding, build software infrastructure and analysis algorithms, and incorporate external data sets into their LSST-based research.

The Science Collaborations also provide valuable advice to Rubin Observatory on the operational strategies and data products to accomplish specific science goals, and Rubin Observatory supports the collaborations via staff liaisons and regular virtual meetings with Rubin operations leadership.

¹¹³ <https://community.lsst.org/>

¹¹⁴ <https://rubinobservatory.org/for-scientists/events-deadlines>

3142 The Science Collaborations have been functioning for
 3143 many years, and their engagement and feedback on DP0
 3144 was implemented into the community science model for
 3145 DP1, as it will for future data releases.

3146 8. SUMMARY AND FUTURE RELEASES

3147 Rubin Data Preview 1 offers an initial look at the first
 3148 on-sky data products and access services from the Vera
 3149 C. Rubin Observatory. DP1 forms part of Rubin’s Early
 3150 Science Program, and provides the scientific community
 3151 with an early opportunity to familiarize themselves with
 3152 the data formats and access infrastructure for the forth-
 3153 coming Legacy Survey of Space and Time. This early
 3154 release has a proprietary period of two years, during
 3155 which time it is available to Rubin data rights holders
 3156 only via the cloud-based RSP.

3157 In this paper we have described the completion status
 3158 of the observatory at the time of data acquisition, the
 3159 commissioning campaign that forms the basis of DP1,
 3160 and the processing pipelines used to produce early ver-
 3161 sions of data products. We provide details on the data
 3162 products, their characteristics and known issues, and
 3163 describe the Rubin Science Platform for access to and
 3164 analysis of DP1.

3165 The data products described in this paper derive from
 3166 observations obtained by LSSTComCam. LSSTCom-
 3167 Cam contains only around 5% the number of CCDs as
 3168 the full LSST Science Camera (LSSTCam), yet the DP1
 3169 dataset that it has produced will already enable a very
 3170 broad range of science. At 3.5 TB in size, DP1 covers
 3171 a total area of ~ 15 deg² and contains 1792 single-epoch
 3172 images, 2644 deep coadded images and 2.3 million dis-
 3173 tinct astrophysical objects, including 93 new asteroid
 3174 discoveries.

3175 While some data products anticipated from the LSST
 3176 are not yet available, e.g., cell-based coadds, DP1 in-
 3177 cludes several products that will not be provided in fu-
 3178 ture releases. Notably, difference images are included in
 3179 DP1 as pre-generated products; in future releases, these
 3180 will instead be generated on demand via dedicated ser-
 3181 vices. The inclusion of pre-generated difference images
 3182 in DP1 is feasible due to the relatively small size of the
 3183 dataset, an approach that will not scale to the signifi-
 3184 cantly larger data volumes expected in subsequent re-
 3185 leases.

3186 The RSP is continually under development, and new
 3187 functionality will continue to be deployed incrementally

3188 as it becomes available, and independent of the future
 3189 data release schedule. User query history capabilities,
 3190 context-aware documentation and a bulk cutout services
 3191 are just a few of the services currently under develop-
 3192 ment.

3193 Coincident with the release of DP1, Rubin Obser-
 3194 vatory begins its Science Validation Surveys with the
 3195 LSST Science Camera (i.e., LSSTCam). This final com-
 3196 missioning phase will produce a dataset that will form
 3197 the foundation for the second Rubin Data Preview, DP2.
 3198 Full operations, marking the start of the LSST, are ex-
 3199 pected to commence in 2026.

ACKNOWLEDGMENTS

3200 . This material is based upon work supported in part by
 3201 the National Science Foundation through Cooperative
 3202 Agreements AST-1258333 and AST-2241526 and Co-
 3203 operative Support Agreements AST-1202910 and AST-
 3204 2211468 managed by the Association of Universities for
 3205 Research in Astronomy (AURA), and the Department of
 3206 Energy under Contract No. DE-AC02-76SF00515 with
 3207 the SLAC National Accelerator Laboratory managed
 3208 by Stanford University. Additional Rubin Observatory
 3209 funding comes from private donations, grants to univer-
 3210 sities, and in-kind support from LSST-DA Institutional
 3211 Members.

3212 This work has been supported by the French Na-
 3213 tional Institute of Nuclear and Particle Physics (IN2P3)
 3214 through dedicated funding provided by the National
 3215 Center for Scientific Research (CNRS).

3216 This work has been supported by STFC fund-
 3217 ing for UK participation in LSST, through grant
 3218 ST/Y00292X/1.
 3219

3220 *Facilities:* Rubin:Simonyi (LSSTComCam), Ru-
 3221 bin:USDAC

3222 *Software:* Rubin Data Butler (T. Jenness et al.
 3223 2022), LSST Science Pipelines (Rubin Observatory Sci-
 3224 ence Pipelines Developers 2025), LSST Feature Based
 3225 Scheduler v3.0 (P. Yoachim et al. 2024; E. Naghib et al.
 3226 2019) Astropy (Astropy Collaboration et al. 2013, 2018,
 3227 2022) PIFF (M. Jarvis et al. 2021), GBDES (G. M.
 3228 Bernstein 2022), Qserv (D. L. Wang et al. 2011; F.
 3229 Mueller et al. 2023), Slurm, HTCondor, CVMFS, FTS3,
 3230 ESNset

APPENDIX

REFERENCES

- 3232 Abazajian, K., Adelman-McCarthy, J. K., Agüeros, M. A.,
3233 et al. 2004, *AJ*, 128, 502, doi: [10.1086/421365](https://doi.org/10.1086/421365)
- 3234 Ahumada, R., Allende Prieto, C., Almeida, A., et al. 2020,
3235 *ApJS*, 249, 3, doi: [10.3847/1538-4365/ab929e](https://doi.org/10.3847/1538-4365/ab929e)
- 3236 Aihara, H., AlSayyad, Y., Ando, M., et al. 2022, *PASJ*, 74,
3237 247, doi: [10.1093/pasj/psab122](https://doi.org/10.1093/pasj/psab122)
- 3238 Allbery, R. 2023, IVOA SODA implementation experience,
3239 SQuaRE Technical Note SQR-063, NSF-DOE Vera C.
3240 Rubin Observatory. <https://sqr-063.lsst.io/>
- 3241 Allbery, R. 2024, Draft IVOA SODA web service
3242 specification, SQuaRE Technical Note SQR-093,
3243 NSF-DOE Vera C. Rubin Observatory.
3244 <https://sqr-093.lsst.io/>
- 3245 AlSayyad, Y. 2018, Coaddition Artifact Rejection and
3246 CompareWarp, Data Management Technical Note
3247 DMTN-080, NSF-DOE Vera C. Rubin Observatory,
3248 doi: [10.71929/rubin/2583441](https://doi.org/10.71929/rubin/2583441)
- 3249 Ansel, J., Yang, E., He, H., et al. 2024, in 29th ACM
3250 International Conference on Architectural Support for
3251 Programming Languages and Operating Systems, Volume
3252 2 (ASPLOS '24) (ACM), doi: [10.1145/3620665.3640366](https://doi.org/10.1145/3620665.3640366)
- 3253 Antilogus, P., Astier, P., Doherty, P., Guyonnet, A., &
3254 Regnault, N. 2014, *Journal of Instrumentation*, 9,
3255 C03048, doi: [10.1088/1748-0221/9/03/C03048](https://doi.org/10.1088/1748-0221/9/03/C03048)
- 3256 Astropy Collaboration, Robitaille, T. P., Tollerud, E. J.,
3257 et al. 2013, *A&A*, 558, A33,
3258 doi: [10.1051/0004-6361/201322068](https://doi.org/10.1051/0004-6361/201322068)
- 3259 Astropy Collaboration, Price-Whelan, A. M., Sipőcz, B. M.,
3260 et al. 2018, *AJ*, 156, 123, doi: [10.3847/1538-3881/aabc4f](https://doi.org/10.3847/1538-3881/aabc4f)
- 3261 Astropy Collaboration, Price-Whelan, A. M., Lim, P. L.,
3262 et al. 2022, *ApJ*, 935, 167, doi: [10.3847/1538-4357/ac7c74](https://doi.org/10.3847/1538-4357/ac7c74)
- 3263 Baumann, M., Boch, T., Pineau, F.-X., et al. 2022, in
3264 *Astronomical Society of the Pacific Conference Series*,
3265 Vol. 532, *Astronomical Data Analysis Software and*
3266 *Systems XXX*, ed. J. E. Ruiz, F. Pierfederici, &
3267 P. Teuben, 7
- 3268 Bechtol, K., Sevilla-Noarbe, I., Drlica-Wagner, A., et al.
3269 2025, arXiv e-prints, arXiv:2501.05739,
3270 doi: [10.48550/arXiv.2501.05739](https://doi.org/10.48550/arXiv.2501.05739)
- 3271 Berk, A., Anderson, G. P., Bernstein, L. S., et al. 1999, in
3272 *Society of Photo-Optical Instrumentation Engineers*
3273 *(SPIE) Conference Series*, Vol. 3756, *Optical*
3274 *Spectroscopic Techniques and Instrumentation for*
3275 *Atmospheric and Space Research III*, ed. A. M. Larar,
3276 348–353, doi: [10.1117/12.366388](https://doi.org/10.1117/12.366388)
- 3277 Bernstein, G. M. 2022, gbdes: DECam instrumental
3278 signature fitting and processing programs,, *Astrophysics*
3279 *Source Code Library*, record ascl:2210.011
3280 <http://ascl.net/2210.011>
- 3281 Bernstein, G. M., & Jarvis, M. 2002, *AJ*, 123, 583,
3282 doi: [10.1086/338085](https://doi.org/10.1086/338085)
- 3283 Bernstein, G. M., Armstrong, R., Plazas, A. A., et al. 2017,
3284 *PASP*, 129, 074503, doi: [10.1088/1538-3873/aa6c55](https://doi.org/10.1088/1538-3873/aa6c55)
- 3285 Bertin, E. 2011, in *Astronomical Society of the Pacific*
3286 *Conference Series*, Vol. 442, *Astronomical Data Analysis*
3287 *Software and Systems XX*, ed. I. N. Evans,
3288 A. Accomazzi, D. J. Mink, & A. H. Rots, 435
- 3289 Bianco, F. B., Ivezić, Ž., Jones, R. L., et al. 2022, *ApJS*,
3290 258, 1, doi: [10.3847/1538-4365/ac3e72](https://doi.org/10.3847/1538-4365/ac3e72)
- 3291 Blum, R., & the Rubin Operations Team. 2020, Vera C.
3292 Rubin Observatory Data Policy, Data Management
3293 Operations Controlled Document RDO-013, NSF-DOE
3294 Vera C. Rubin Observatory. <https://ls.st/RDO-013>
- 3295 Boch, T., & Fernique, P. 2014, in *Astronomical Society of*
3296 *the Pacific Conference Series*, Vol. 485, *Astronomical*
3297 *Data Analysis Software and Systems XXIII*, ed.
3298 N. Manset & P. Forshay, 277
- 3299 Bonnarel, F., Dowler, P., Demleitner, M., Tody, D., &
3300 Dempsey, J. 2017, IVOA Server-side Operations for Data
3301 Access Version 1.0., IVOA Recommendation 17 May 2017
3302 doi: [10.5479/ADS/bib/2017ivoa.spec.0517B](https://doi.org/10.5479/ADS/bib/2017ivoa.spec.0517B)
- 3303 Bonnarel, F., Fernique, P., Bienaymé, O., et al. 2000,
3304 *A&AS*, 143, 33, doi: [10.1051/aas:2000331](https://doi.org/10.1051/aas:2000331)
- 3305 Bosch, J., Armstrong, R., Bickerton, S., et al. 2018, *PASJ*,
3306 70, S5, doi: [10.1093/pasj/psx080](https://doi.org/10.1093/pasj/psx080)
- 3307 Broughton, A., Utsumi, Y., Plazas Malagón, A. A., et al.
3308 2024, *PASP*, 136, 045003, doi: [10.1088/1538-3873/ad3aa2](https://doi.org/10.1088/1538-3873/ad3aa2)
- 3309 Burke, D. L., Rykoff, E. S., Allam, S., et al. 2018, *AJ*, 155,
3310 41, doi: [10.3847/1538-3881/aa9f22](https://doi.org/10.3847/1538-3881/aa9f22)
- 3311 Chambers, K. C., Magnier, E. A., Metcalfe, N., et al. 2016,
3312 arXiv e-prints, arXiv:1612.05560,
3313 doi: [10.48550/arXiv.1612.05560](https://doi.org/10.48550/arXiv.1612.05560)
- 3314 Choi, Y., Olsen, K. A. G., Carlin, J. L., et al. 2025, arXiv
3315 e-prints, arXiv:2507.01343,
3316 doi: [10.48550/arXiv.2507.01343](https://doi.org/10.48550/arXiv.2507.01343)
- 3317 de Vaucouleurs, G. 1948, *Annales d’Astrophysique*, 11, 247
- 3318 de Vaucouleurs, G. 1953, *MNRAS*, 113, 134,
3319 doi: [10.1093/mnras/113.2.134](https://doi.org/10.1093/mnras/113.2.134)
- 3320 Dowler, P., Bonnarel, F., & Tody, D. 2015, IVOA Simple
3321 Image Access Version 2.0., IVOA Recommendation 23
3322 December 2015
3323 doi: [10.5479/ADS/bib/2015ivoa.spec.1223D](https://doi.org/10.5479/ADS/bib/2015ivoa.spec.1223D)
- 3324 Dowler, P., Rixon, G., Tody, D., & Demleitner, M. 2019,
3325 Table Access Protocol Version 1.1., IVOA
3326 Recommendation 27 September 2019
3327 doi: [10.5479/ADS/bib/2019ivoa.spec.0927D](https://doi.org/10.5479/ADS/bib/2019ivoa.spec.0927D)

- 3328 Eggl, S., Juric, M., Moeyens, J., & Jones, L. 2020, in
3329 AAS/Division for Planetary Sciences Meeting Abstracts,
3330 Vol. 52, AAS/Division for Planetary Sciences Meeting
3331 Abstracts, 211.01
- 3332 Esteves, J. H., Utsumi, Y., Snyder, A., et al. 2023, PASP,
3333 135, 115003, doi: [10.1088/1538-3873/ad0a73](https://doi.org/10.1088/1538-3873/ad0a73)
- 3334 Euclid Collaboration, Romelli, E., Kümmel, M., et al. 2025,
3335 arXiv e-prints, arXiv:2503.15305,
3336 doi: [10.48550/arXiv.2503.15305](https://doi.org/10.48550/arXiv.2503.15305)
- 3337 Fagrelus, P., & Rykoff, E. S. 2025, Rubin Observatory
3338 Baseline Calibration Plan, Commissioning Technical
3339 Note SITCOMTN-086, NSF-DOE Vera C. Rubin
3340 Observatory, doi: [10.71929/rubin/2583850](https://doi.org/10.71929/rubin/2583850)
- 3341 Ferguson, P. S., Rykoff, E. S., Carlin, J. L., Saunders, C., &
3342 Parejko, J. K. 2025, The Monster: A reference catalog
3343 with synthetic ugrizy-band fluxes for the Vera C. Rubin
3344 observatory, Data Management Technical Note
3345 DMTN-277, NSF-DOE Vera C. Rubin Observatory,
3346 doi: [10.71929/rubin/2583688](https://doi.org/10.71929/rubin/2583688)
- 3347 Fernique, P., Allen, M. G., Boch, T., et al. 2015, A&A, 578,
3348 A114, doi: [10.1051/0004-6361/201526075](https://doi.org/10.1051/0004-6361/201526075)
- 3349 Fernique, P., Allen, M., Boch, T., et al. 2017, HiPS -
3350 Hierarchical Progressive Survey Version 1.0., IVOA
3351 Recommendation 19 May 2017
3352 doi: [10.5479/ADS/bib/2017ivoa.spec.0519F](https://doi.org/10.5479/ADS/bib/2017ivoa.spec.0519F)
- 3353 Finkbeiner, D. P., Davis, M., & Schlegel, D. J. 1999, The
3354 Astrophysical Journal, 524, 867, doi: [10.1086/307852](https://doi.org/10.1086/307852)
- 3355 Fortino, W. F., Bernstein, G. M., Bernardinelli, P. H., et al.
3356 2021, AJ, 162, 106, doi: [10.3847/1538-3881/ac0722](https://doi.org/10.3847/1538-3881/ac0722)
- 3357 Gaia Collaboration, Montegriffo, P., Bellazzini, M., et al.
3358 2023a, A&A, 674, A33,
3359 doi: [10.1051/0004-6361/202243709](https://doi.org/10.1051/0004-6361/202243709)
- 3360 Gaia Collaboration, Vallenari, A., Brown, A. G. A., et al.
3361 2023b, A&A, 674, A1, doi: [10.1051/0004-6361/202243940](https://doi.org/10.1051/0004-6361/202243940)
- 3362 Górski, K. M., Hivon, E., Banday, A. J., et al. 2005, ApJ,
3363 622, 759, doi: [10.1086/427976](https://doi.org/10.1086/427976)
- 3364 Graham, A. W., & Driver, S. P. 2005, PASA, 22, 118,
3365 doi: [10.1071/AS05001](https://doi.org/10.1071/AS05001)
- 3366 Graham, M., Plante, R., Tody, D., & Fitzpatrick, M. 2014,
3367 PyVO: Python access to the Virtual Observatory,,
3368 Astrophysics Source Code Library, record ascl:1402.004
- 3369 Graham, M. L., Carlin, J. L., Adair, C. L., et al. 2026,
3370 Guidelines for User Tutorials, Technical Note RTN-045,
3371 NSF-DOE Vera C. Rubin Observatory,
3372 doi: [10.71929/rubin/2584020](https://doi.org/10.71929/rubin/2584020)
- 3373 Gray, B. 2025, find_orb: Orbit determination from
3374 observations, https://github.com/Bill-Gray/find_orb
- 3375 Guy, L. P., Bechtol, K., Bellm, E., et al. 2026, Rubin
3376 Observatory Plans for an Early Science Program,
3377 Technical Note RTN-011, NSF-DOE Vera C. Rubin
3378 Observatory, doi: [10.71929/rubin/2584021](https://doi.org/10.71929/rubin/2584021)
- 3379 Heinze, A., Eggl, S., Juric, M., et al. 2022, in AAS/Division
3380 for Planetary Sciences Meeting Abstracts, Vol. 54,
3381 AAS/Division for Planetary Sciences Meeting Abstracts,
3382 504.04
- 3383 Heinze, A., Juric, M., & Kurlander, J. 2023, heliolineX: Open
3384 Source Solar System Discovery Software,
3385 <https://github.com/heliolineX/heliolineX>
- 3386 Hirata, C., & Seljak, U. 2003, MNRAS, 343, 459,
3387 doi: [10.1046/j.1365-8711.2003.06683.x](https://doi.org/10.1046/j.1365-8711.2003.06683.x)
- 3388 Holman, M. J., Payne, M. J., Blankley, P., Janssen, R., &
3389 Kuindersma, S. 2018, AJ, 156, 135,
3390 doi: [10.3847/1538-3881/aad69a](https://doi.org/10.3847/1538-3881/aad69a)
- 3391 Howard, J., Reil, K., Claver, C., et al. 2018, in Society of
3392 Photo-Optical Instrumentation Engineers (SPIE)
3393 Conference Series, Vol. 10700, Ground-based and
3394 Airborne Telescopes VII, ed. H. K. Marshall &
3395 J. Spyromilio, 107003D, doi: [10.1117/12.2312684](https://doi.org/10.1117/12.2312684)
- 3396 Illingworth, G., Magee, D., Bouwens, R., et al. 2016, arXiv
3397 e-prints, arXiv:1606.00841,
3398 doi: [10.48550/arXiv.1606.00841](https://doi.org/10.48550/arXiv.1606.00841)
- 3399 Ingraham, P., Fagrelus, P., Stubbs, C. W., et al. 2022, in
3400 Society of Photo-Optical Instrumentation Engineers
3401 (SPIE) Conference Series, Vol. 12182, Ground-based and
3402 Airborne Telescopes IX, ed. H. K. Marshall,
3403 J. Spyromilio, & T. Usuda, 121820R,
3404 doi: [10.1117/12.2630185](https://doi.org/10.1117/12.2630185)
- 3405 Ivezić, Ž., Kahn, S. M., Tyson, J. A., et al. 2019a, ApJ,
3406 873, 111, doi: [10.3847/1538-4357/ab042c](https://doi.org/10.3847/1538-4357/ab042c)
- 3407 Ivezić, Ž., Kahn, S. M., Tyson, J. A., et al. 2019b, ApJ,
3408 873, 111, doi: [10.3847/1538-4357/ab042c](https://doi.org/10.3847/1538-4357/ab042c)
- 3409 Jarvis, M., et al. 2021, Mon. Not. Roy. Astron. Soc., 501,
3410 1282, doi: [10.1093/mnras/staa3679](https://doi.org/10.1093/mnras/staa3679)
- 3411 Jenness, T., & Dubois-Felsmann, G. P. 2025, IVOA
3412 Identifier Usage at the Rubin Observatory, Data
3413 Management Technical Note DMTN-302, NSF-DOE Vera
3414 C. Rubin Observatory, doi: [10.71929/rubin/2583848](https://doi.org/10.71929/rubin/2583848)
- 3415 Jenness, T., Voutsinas, S., Dubois-Felsmann, G. P., &
3416 Salnikov, A. 2024, arXiv e-prints, arXiv:2501.00544,
3417 doi: [10.48550/arXiv.2501.00544](https://doi.org/10.48550/arXiv.2501.00544)
- 3418 Jenness, T., Bosch, J. F., Salnikov, A., et al. 2022, in
3419 Society of Photo-Optical Instrumentation Engineers
3420 (SPIE) Conference Series, Vol. 12189, Software and
3421 Cyberinfrastructure for Astronomy VII, 1218911,
3422 doi: [10.1117/12.2629569](https://doi.org/10.1117/12.2629569)

- 3423 Jones, R. L., Yoachim, P., Ivezić, Ž., Neilsen Jr., E. H., &
 3424 Ribeiro, T. 2021, Survey Strategy and Cadence Choices
 3425 for the Vera C. Rubin Observatory Legacy Survey of
 3426 Space and Time (LSST), Project Science Technical Note
 3427 PSTN-051, NSF-DOE Vera C. Rubin Observatory,
 3428 doi: [10.71929/rubin/2584084](https://doi.org/10.71929/rubin/2584084)
- 3429 Juric, M. 2025, mpsky: Multi-purpose sky catalog
 3430 cross-matching, <https://github.com/mjuric/mpsky>
- 3431 Jurić, M., Ciardi, D., Dubois-Felsmann, G., & Guy, L.
 3432 2019, LSST Science Platform Vision Document, Systems
 3433 Engineering Controlled Document LSE-319, NSF-DOE
 3434 Vera C. Rubin Observatory, doi: [10.71929/rubin/2587242](https://doi.org/10.71929/rubin/2587242)
- 3435 Jurić, M., Axelrod, T. S., Becker, A. C., et al. 2023, Data
 3436 Products Definition Document, Systems Engineering
 3437 Controlled Document LSE-163, NSF-DOE Vera C. Rubin
 3438 Observatory, doi: [10.71929/rubin/2587118](https://doi.org/10.71929/rubin/2587118)
- 3439 Kannawadi, A. 2025, Consistent galaxy colors with
 3440 Gaussian-Aperture and PSF photometry, Data
 3441 Management Technical Note DMTN-190, NSF-DOE Vera
 3442 C. Rubin Observatory, doi: [10.71929/rubin/2583849](https://doi.org/10.71929/rubin/2583849)
- 3443 Kron, R. G. 1980, ApJS, 43, 305, doi: [10.1086/190669](https://doi.org/10.1086/190669)
- 3444 Kuijken, K. 2008, A&A, 482, 1053,
 3445 doi: [10.1051/0004-6361:20066601](https://doi.org/10.1051/0004-6361:20066601)
- 3446 Lange, T., Nordby, M., Pollek, H., et al. 2024, in Society of
 3447 Photo-Optical Instrumentation Engineers (SPIE)
 3448 Conference Series, Vol. 13096, Ground-based and
 3449 Airborne Instrumentation for Astronomy X, ed. J. J.
 3450 Bryant, K. Motohara, & J. R. D. Vernet, 130961O,
 3451 doi: [10.1117/12.3019302](https://doi.org/10.1117/12.3019302)
- 3452 Léget, P. F., Astier, P., Regnault, N., et al. 2021, A&A,
 3453 650, A81, doi: [10.1051/0004-6361/202140463](https://doi.org/10.1051/0004-6361/202140463)
- 3454 Lim, K.-T. 2023, Proposal and Prototype for Prompt
 3455 Processing, Data Management Technical Note
 3456 DMTN-219, NSF-DOE Vera C. Rubin Observatory,
 3457 doi: [10.71929/rubin/2585429](https://doi.org/10.71929/rubin/2585429)
- 3458 Louys, M., Tody, D., Dowler, P., et al. 2017, Observation
 3459 Data Model Core Components, its Implementation in the
 3460 Table Access Protocol Version 1.1., IVOA
 3461 Recommendation 09 May 2017
 3462 doi: [10.5479/ADS/bib/2017ivoa.spec.0509L](https://doi.org/10.5479/ADS/bib/2017ivoa.spec.0509L)
- 3463 LSST Dark Energy Science Collaboration (LSST DESC),
 3464 Abolfathi, B., Alonso, D., et al. 2021, ApJS, 253, 31,
 3465 doi: [10.3847/1538-4365/abd62c](https://doi.org/10.3847/1538-4365/abd62c)
- 3466 Lupton, R., Blanton, M. R., Fekete, G., et al. 2004, PASP,
 3467 116, 133, doi: [10.1086/382245](https://doi.org/10.1086/382245)
- 3468 Lust, N. B., Jenness, T., Bosch, J. F., et al. 2023, arXiv
 3469 e-prints, arXiv:2303.03313,
 3470 doi: [10.48550/arXiv.2303.03313](https://doi.org/10.48550/arXiv.2303.03313)
- 3471 Mandelbaum, R., Hirata, C. M., Seljak, U., et al. 2005,
 3472 MNRAS, 361, 1287,
 3473 doi: [10.1111/j.1365-2966.2005.09282.x](https://doi.org/10.1111/j.1365-2966.2005.09282.x)
- 3474 Megias Homar, G., Kahn, S. M., Meyers, J. M., Crenshaw,
 3475 J. F., & Thomas, S. J. 2024, The Astrophysical Journal,
 3476 974, 108, doi: [10.3847/1538-4357/ad6cdc](https://doi.org/10.3847/1538-4357/ad6cdc)
- 3477 Megias Homar, G., Tighe, R., Thomas, S., et al. 2024, in
 3478 Ground-based and Airborne Telescopes X, ed. H. K.
 3479 Marshall, J. Spyromilio, & T. Usuda, Vol. 13094,
 3480 International Society for Optics and Photonics (SPIE),
 3481 130943C, doi: [10.1117/12.3019031](https://doi.org/10.1117/12.3019031)
- 3482 Melchior, P., Moolekamp, F., Jerdee, M., et al. 2018,
 3483 Astronomy and Computing, 24, 129,
 3484 doi: [10.1016/j.ascom.2018.07.001](https://doi.org/10.1016/j.ascom.2018.07.001)
- 3485 Mueller, F., et al. 2023, in ASP Conf. Ser., Vol. TBD,
 3486 ADASS XXXII, ed. S. Gaudet, S. Gwyn, P. Dowler,
 3487 D. Bohlender, & A. Hincks (San Francisco: ASP), in
 3488 press. <https://dmtn-243.lsst.io>
- 3489 Naghib, E., Yoachim, P., Vanderbei, R. J., Connolly, A. J.,
 3490 & Jones, R. L. 2019, The Astronomical Journal, 157, 151,
 3491 doi: [10.3847/1538-3881/aafece](https://doi.org/10.3847/1538-3881/aafece)
- 3492 NSF-DOE Vera C. Rubin Observatory. 2021, Rubin
 3493 Observatory LSST Tutorials [Computer Software],
 3494 NSF-DOE Vera C. Rubin Observatory,
 3495 doi: [10.11578/rubin/dc.20250909.20](https://doi.org/10.11578/rubin/dc.20250909.20)
- 3496 NSF-DOE Vera C. Rubin Observatory. 2025a, Legacy
 3497 Survey of Space and Time Data Preview 1 [Data set],
 3498 NSF-DOE Vera C. Rubin Observatory,
 3499 doi: [10.71929/RUBIN/2570308](https://doi.org/10.71929/RUBIN/2570308)
- 3500 NSF-DOE Vera C. Rubin Observatory. 2025b, Legacy
 3501 Survey of Space and Time Data Preview 1: raw dataset
 3502 type [Data set], NSF-DOE Vera C. Rubin Observatory,
 3503 doi: [10.71929/RUBIN/2570310](https://doi.org/10.71929/RUBIN/2570310)
- 3504 NSF-DOE Vera C. Rubin Observatory. 2025c, Legacy
 3505 Survey of Space and Time Data Preview 1: visit_image
 3506 dataset type [Data set], NSF-DOE Vera C. Rubin
 3507 Observatory, doi: [10.71929/RUBIN/2570311](https://doi.org/10.71929/RUBIN/2570311)
- 3508 NSF-DOE Vera C. Rubin Observatory. 2025d, Legacy
 3509 Survey of Space and Time Data Preview 1:
 3510 template_coadd dataset type [Data set], NSF-DOE Vera
 3511 C. Rubin Observatory, doi: [10.71929/RUBIN/2570314](https://doi.org/10.71929/RUBIN/2570314)
- 3512 NSF-DOE Vera C. Rubin Observatory. 2025e, Legacy
 3513 Survey of Space and Time Data Preview 1:
 3514 difference_image dataset type [Data set], NSF-DOE Vera
 3515 C. Rubin Observatory, doi: [10.71929/RUBIN/2570312](https://doi.org/10.71929/RUBIN/2570312)
- 3516 NSF-DOE Vera C. Rubin Observatory. 2025f, Legacy
 3517 Survey of Space and Time Data Preview 1: Source
 3518 searchable catalog [Data set], NSF-DOE Vera C. Rubin
 3519 Observatory, doi: [10.71929/RUBIN/2570323](https://doi.org/10.71929/RUBIN/2570323)

- 3520 NSF-DOE Vera C. Rubin Observatory. 2025g, Legacy
3521 Survey of Space and Time Data Preview 1: Object
3522 searchable catalog [Data set], NSF-DOE Vera C. Rubin
3523 Observatory, doi: [10.71929/RUBIN/2570325](https://doi.org/10.71929/RUBIN/2570325)
- 3524 NSF-DOE Vera C. Rubin Observatory. 2025h, Legacy
3525 Survey of Space and Time Data Preview 1: ForcedSource
3526 searchable catalog [Data set], NSF-DOE Vera C. Rubin
3527 Observatory, doi: [10.71929/RUBIN/2570327](https://doi.org/10.71929/RUBIN/2570327)
- 3528 NSF-DOE Vera C. Rubin Observatory. 2025i, Legacy
3529 Survey of Space and Time Data Preview 1: DiaSource
3530 searchable catalog [Data set], NSF-DOE Vera C. Rubin
3531 Observatory, doi: [10.71929/RUBIN/2570317](https://doi.org/10.71929/RUBIN/2570317)
- 3532 NSF-DOE Vera C. Rubin Observatory. 2025j, Legacy
3533 Survey of Space and Time Data Preview 1: DiaObject
3534 searchable catalog [Data set], NSF-DOE Vera C. Rubin
3535 Observatory, doi: [10.71929/RUBIN/2570319](https://doi.org/10.71929/RUBIN/2570319)
- 3536 NSF-DOE Vera C. Rubin Observatory. 2025k, Legacy
3537 Survey of Space and Time Data Preview 1:
3538 ForcedSourceOnDiaObject searchable catalog [Data set],
3539 NSF-DOE Vera C. Rubin Observatory,
3540 doi: [10.71929/RUBIN/2570321](https://doi.org/10.71929/RUBIN/2570321)
- 3541 NSF-DOE Vera C. Rubin Observatory. 2025l, Legacy
3542 Survey of Space and Time Data Preview 1: SSOBJECT
3543 searchable catalog [Data set], NSF-DOE Vera C. Rubin
3544 Observatory, doi: [10.71929/RUBIN/2570335](https://doi.org/10.71929/RUBIN/2570335)
- 3545 NSF-DOE Vera C. Rubin Observatory. 2025m, Legacy
3546 Survey of Space and Time Data Preview 1: SSSource
3547 searchable catalog [Data set], NSF-DOE Vera C. Rubin
3548 Observatory, doi: [10.71929/RUBIN/2570333](https://doi.org/10.71929/RUBIN/2570333)
- 3549 NSF-DOE Vera C. Rubin Observatory. 2025n, Legacy
3550 Survey of Space and Time Data Preview 1: CcdVisit
3551 searchable catalog [Data set], NSF-DOE Vera C. Rubin
3552 Observatory, doi: [10.71929/RUBIN/2570331](https://doi.org/10.71929/RUBIN/2570331)
- 3553 NSF-DOE Vera C. Rubin Observatory. 2025o, Legacy
3554 Survey of Space and Time Data Preview 1: survey
3555 property dataset type [Data set], NSF-DOE Vera C.
3556 Rubin Observatory, doi: [10.71929/RUBIN/2570315](https://doi.org/10.71929/RUBIN/2570315)
- 3557 Oke, J. B., & Gunn, J. E. 1983, ApJ, 266, 713,
3558 doi: [10.1086/160817](https://doi.org/10.1086/160817)
- 3559 O'Mullane, W., Economou, F., Huang, F., et al. 2024a, in
3560 Astronomical Society of the Pacific Conference Series,
3561 Vol. 535, Astronomical Data Analysis Software and Systems
3562 XXXI, ed. B. V. Hugo, R. Van Rooyen, & O. M.
3563 Smirnov, 227, doi: [10.48550/arXiv.2111.15030](https://doi.org/10.48550/arXiv.2111.15030)
- 3564 O'Mullane, W., AlSaiyad, Y., Chiang, J., et al. 2024b, in
3565 Society of Photo-Optical Instrumentation Engineers
3566 (SPIE) Conference Series, Vol. 13101, Software and
3567 Cyberinfrastructure for Astronomy VIII, ed. J. Ibsen &
3568 G. Chiozzi, 131012B, doi: [10.1117/12.3018005](https://doi.org/10.1117/12.3018005)
- 3569 Onken, C. A., Wolf, C., Bessell, M. S., et al. 2019, PASA,
3570 36, e033, doi: [10.1017/pasa.2019.27](https://doi.org/10.1017/pasa.2019.27)
- 3571 Park, H. Y., Nomerotski, A., & Tsybychev, D. 2017,
3572 Journal of Instrumentation, 12, C05015,
3573 doi: [10.1088/1748-0221/12/05/C05015](https://doi.org/10.1088/1748-0221/12/05/C05015)
- 3574 Petrosian, V. 1976, ApJL, 210, L53,
3575 doi: [10.1086/18230110.1086/182253](https://doi.org/10.1086/18230110.1086/182253)
- 3576 Plazas, A. A., Shapiro, C., Smith, R., Huff, E., & Rhodes,
3577 J. 2018, Publications of the Astronomical Society of the
3578 Pacific, 130, 065004, doi: [10.1088/1538-3873/aab820](https://doi.org/10.1088/1538-3873/aab820)
- 3579 Plazas Malagón, A. A., Digel, S. W., Roodman, A., et al.
3580 2026, LSSTCam and ComCam Focal Plane Layouts,
3581 Camera Technical Note CTN-001, NSF-DOE Vera C.
3582 Rubin Observatory, doi: [10.71929/rubin/2584019](https://doi.org/10.71929/rubin/2584019)
- 3583 Plazas Malagón, A. A., Waters, C., Broughton, A., et al.
3584 2025, Journal of Astronomical Telescopes, Instruments,
3585 and Systems, 11, 011209,
3586 doi: [10.1117/1.JATIS.11.1.011209](https://doi.org/10.1117/1.JATIS.11.1.011209)
- 3587 Porter, M. N., Tucker, D. L., Smith, J. A., & Adair, C. L.
3588 2026, Photometric Transformation Relations for the
3589 LSST Data Preview 1, Technical Note RTN-099,
3590 NSF-DOE Vera C. Rubin Observatory,
3591 doi: [10.71929/rubin/3006074](https://doi.org/10.71929/rubin/3006074)
- 3592 Refregier, A. 2003, ARA&A, 41, 645,
3593 doi: [10.1146/annurev.astro.41.111302.102207](https://doi.org/10.1146/annurev.astro.41.111302.102207)
- 3594 Reiss, D. J., & Lupton, R. H. 2016, Implementation of
3595 Image Difference Decorrelation, Data Management
3596 Technical Note DMTN-021, NSF-DOE Vera C. Rubin
3597 Observatory, doi: [10.71929/rubin/2586490](https://doi.org/10.71929/rubin/2586490)
- 3598 Roodman, A., Rasmussen, A., Bradshaw, A., et al. 2024, in
3599 Society of Photo-Optical Instrumentation Engineers
3600 (SPIE) Conference Series, Vol. 13096, Ground-based and
3601 Airborne Instrumentation for Astronomy X, ed. J. J.
3602 Bryant, K. Motohara, & J. R. D. Vernet, 130961S,
3603 doi: [10.1117/12.3019698](https://doi.org/10.1117/12.3019698)
- 3604 Rubin, V. C., & Ford, Jr., W. K. 1970, ApJ, 159, 379,
3605 doi: [10.1086/150317](https://doi.org/10.1086/150317)
- 3606 Rubin, V. C., Ford, Jr., W. K., & Thonnard, N. 1980, ApJ,
3607 238, 471, doi: [10.1086/158003](https://doi.org/10.1086/158003)
- 3608 Rubin Observatory Science Pipelines Developers. 2025, The
3609 LSST Science Pipelines Software: Optical Survey
3610 Pipeline Reduction and Analysis Environment, Project
3611 Science Technical Note PSTN-019, NSF-DOE Vera C.
3612 Rubin Observatory, doi: [10.71929/rubin/2570545](https://doi.org/10.71929/rubin/2570545)
- 3613 Rubin's Survey Cadence Optimization Committee, Bauer,
3614 F. E., Brough, S., et al. 2022, Survey Cadence
3615 Optimization Committee's Phase 1 Recommendation,
3616 Project Science Technical Note PSTN-053, NSF-DOE
3617 Vera C. Rubin Observatory, doi: [10.71929/rubin/2584276](https://doi.org/10.71929/rubin/2584276)

- 3618 Rubin's Survey Cadence Optimization Committee, Bauer,
3619 F. E., Bianco, F. B., et al. 2023, Survey Cadence
3620 Optimization Committee's Phase 2 Recommendations,
3621 Project Science Technical Note PSTN-055, NSF-DOE
3622 Vera C. Rubin Observatory, doi: [10.71929/rubin/2585249](https://doi.org/10.71929/rubin/2585249)
- 3623 Rubin's Survey Cadence Optimization Committee, Bianco,
3624 F. B., Jones, R. L., et al. 2025, Survey Cadence
3625 Optimization Committee's Phase 3 Recommendations,
3626 Project Science Technical Note PSTN-056, NSF-DOE
3627 Vera C. Rubin Observatory, doi: [10.71929/rubin/2585402](https://doi.org/10.71929/rubin/2585402)
- 3628 Rykoff, E. S., Tucker, D. L., Burke, D. L., et al. 2023, arXiv
3629 e-prints, arXiv:2305.01695,
3630 doi: [10.48550/arXiv.2305.01695](https://doi.org/10.48550/arXiv.2305.01695)
- 3631 Saunders, C. 2024, Astrometric Calibration in the LSST
3632 Pipeline, Data Management Technical Note DMTN-266,
3633 NSF-DOE Vera C. Rubin Observatory,
3634 doi: [10.71929/rubin/2583846](https://doi.org/10.71929/rubin/2583846)
- 3635 Schutt, T., Jarvis, M., Roodman, A., et al. 2025, The Open
3636 Journal of Astrophysics, 8, 26, doi: [10.33232/001c.132299](https://doi.org/10.33232/001c.132299)
- 3637 Sérsic, J. L. 1963, Boletín de la Asociación Argentina de
3638 Astronomía La Plata Argentina, 6, 41
- 3639 Sersic, J. L. 1968, Atlas de Galaxias Australes (Cordoba,
3640 Argentina: Observatorio Astronomico)
- 3641 Shanks, T., Metcalfe, N., Chehade, B., et al. 2015,
3642 MNRAS, 451, 4238, doi: [10.1093/mnras/stv1130](https://doi.org/10.1093/mnras/stv1130)
- 3643 SLAC National Accelerator Laboratory, & NSF-DOE Vera
3644 C. Rubin Observatory. 2024, LSST Commissioning
3645 Camera, SLAC National Accelerator Laboratory (SLAC),
3646 Menlo Park, CA (United States),
3647 doi: [10.71929/RUBIN/2561361](https://doi.org/10.71929/RUBIN/2561361)
- 3648 Slater, C. T., Ivezić, Ž., & Lupton, R. H. 2020, AJ, 159, 65,
3649 doi: [10.3847/1538-3881/ab6166](https://doi.org/10.3847/1538-3881/ab6166)
- 3650 Smith, G. E. 2010, Rev. Mod. Phys., 82, 2307,
3651 doi: [10.1103/RevModPhys.82.2307](https://doi.org/10.1103/RevModPhys.82.2307)
- 3652 Stalder, B., Reil, K., Claver, C., et al. 2020, in Society of
3653 Photo-Optical Instrumentation Engineers (SPIE)
3654 Conference Series, Vol. 11447, Ground-based and
3655 Airborne Instrumentation for Astronomy VIII, ed. C. J.
3656 Evans, J. J. Bryant, & K. Motohara, 114470L,
3657 doi: [10.1117/12.2561132](https://doi.org/10.1117/12.2561132)
- 3658 Stalder, B., Reil, K., Aguilar, C., et al. 2022, in Society of
3659 Photo-Optical Instrumentation Engineers (SPIE)
3660 Conference Series, Vol. 12184, Ground-based and
3661 Airborne Instrumentation for Astronomy IX, ed. C. J.
3662 Evans, J. J. Bryant, & K. Motohara, 121840J,
3663 doi: [10.1117/12.2630184](https://doi.org/10.1117/12.2630184)
- 3664 Stalder, B., Munoz, F., Aguilar, C., et al. 2024, in Society
3665 of Photo-Optical Instrumentation Engineers (SPIE)
3666 Conference Series, Vol. 13094, Ground-based and
3667 Airborne Telescopes X, ed. H. K. Marshall, J. Spyromilio,
3668 & T. Usuda, 1309409, doi: [10.1117/12.3019266](https://doi.org/10.1117/12.3019266)
- 3669 Swinbank, J. D., Axelrod, T. S., Becker, A. C., et al. 2020,
3670 Data Management Science Pipelines Design, Data
3671 Management Controlled Document LDM-151, NSF-DOE
3672 Vera C. Rubin Observatory, doi: [10.71929/rubin/2587108](https://doi.org/10.71929/rubin/2587108)
- 3673 Taranu, D. S. 2025, The MultiProFit astronomical source
3674 modelling code, Data Management Technical Note
3675 DMTN-312, NSF-DOE Vera C. Rubin Observatory,
3676 doi: [10.71929/rubin/2584108](https://doi.org/10.71929/rubin/2584108)
- 3677 Taylor, M. 2011, TOPCAT: Tool for OPERations on
3678 Catalogues And Tables,, Astrophysics Source Code
3679 Library, record ascl:1101.010
- 3680 Thomas, S., Connolly, A., Crenshaw, J. F., et al. 2023, in
3681 Adaptive Optics for Extremely Large Telescopes
3682 (AO4ELT7), 67, doi: [10.13009/AO4ELT7-2023-069](https://doi.org/10.13009/AO4ELT7-2023-069)
- 3683 Tonry, J. L., Denneau, L., Heinze, A. N., et al. 2018, PASP,
3684 130, 064505, doi: [10.1088/1538-3873/aabadf](https://doi.org/10.1088/1538-3873/aabadf)
- 3685 Wainer, T. M., Davenport, J. R. A., Bellm, E. C., et al.
3686 2025, Research Notes of the American Astronomical
3687 Society, 9, 171, doi: [10.3847/2515-5172/adecef](https://doi.org/10.3847/2515-5172/adecef)
- 3688 Wang, D. L., Monkewitz, S. M., Lim, K.-T., & Becla, J.
3689 2011, in State of the Practice Reports, SC '11 (New
3690 York, NY, USA: ACM), 12:1–12:11,
3691 doi: [10.1145/2063348.2063364](https://doi.org/10.1145/2063348.2063364)
- 3692 Waters, C. Z., Magnier, E. A., Price, P. A., et al. 2020,
3693 ApJS, 251, 4, doi: [10.3847/1538-4365/abb82b](https://doi.org/10.3847/1538-4365/abb82b)
- 3694 Whitaker, K. E., Ashas, M., Illingworth, G., et al. 2019,
3695 ApJS, 244, 16, doi: [10.3847/1538-4365/ab3853](https://doi.org/10.3847/1538-4365/ab3853)
- 3696 Wu, X., Roby, W., Goldian, T., et al. 2019, in Astronomical
3697 Society of the Pacific Conference Series, Vol. 521,
3698 Astronomical Data Analysis Software and Systems
3699 XXVI, ed. M. Molinaro, K. Shortridge, & F. Pasian, 32
- 3700 Xin, B., Claver, C., Liang, M., et al. 2015, ApOpt, 54,
3701 9045, doi: [10.1364/AO.54.009045](https://doi.org/10.1364/AO.54.009045)
- 3702 Yoachim, P. 2022, Survey Strategy: Rolling Cadence,
3703 Project Science Technical Note PSTN-052, NSF-DOE
3704 Vera C. Rubin Observatory, doi: [10.71929/rubin/2584109](https://doi.org/10.71929/rubin/2584109)
- 3705 Yoachim, P., Jones, L., Eric H. Neilsen, J., & Becker, M. R.
3706 2024, lsst/rubin_scheduler: v3.0.0, v3.0.0 Zenodo,
3707 doi: [10.5281/zenodo.13985198](https://doi.org/10.5281/zenodo.13985198)
- 3708 Zhang, T., Almoubayyed, H., Mandelbaum, R., et al. 2023,
3709 MNRAS, 520, 2328, doi: [10.1093/mnras/stac3350](https://doi.org/10.1093/mnras/stac3350)